TESIS DE LA UNIVERSIDAD DE ZARAGOZA

2013

77

Ana Arizaga Páez

Synthesis of core-shell magnetic nanoparticles for biomedical applications

Departamento
Física de la Materia Condensada

Director/es
Millán Escolano, Ángel
Palacio Parada, Fernando

ISSN 2254-7606

Prensas de la Universidad
Universidad Zaragoza

Universidad Zaragoza
1542

Tesis Doctoral

SYNTHESIS OF CORE-SHELL MAGNETIC NANOPARTICLES FOR BIOMEDICAL APPLICATIONS

Autor

Ana Arizaga Páez

Director/es

Millán Escolano, Ángel
Palacio Parada, Fernando

UNIVERSIDAD DE ZARAGOZA

Física de la Materia Condensada

2013

Synthesis of Core-Shell Magnetic Nanoparticles for Biomedical Applications

Synthesis of Core-Shell Magnetic Nanoparticles for Biomedical Applications

Ana Arizaga Páez

A Jose Luís y Ainhoa

Index

Preface

Nanoscience and nanotechnology are two related promising areas that take advantage of the novel properties that nanostructured materials exhibit. At the nanoscale the classical laws of physics are not able to explain some properties of materials, and the chemical behaviour differs from bulk materials of the same composition. This opens new opportunities to design and develop new functional materials in areas as chemistry, physics, biology, material science, electronics and medicine.

Nanosystems are materials composed by different constituents with at least one of its dimensions at the nanoscale range. One of the most common structures of nanosystems are the core-shell materials, which comprehend single-core and multi-core. Magnetic nanoparticles are of great interest for biomedical applications, and good candidates for being nanosystems cores. Maghemite is especially appealing because it exhibits superparamagnetic behaviour at nanoscale, is non-toxic and is less sensitive to oxidation than other magnetic particles as cobalt, nickel or iron. But it is also important to study the design of the nanosystems in order to optimize the desired characteristics for a chosen application. Normally these particles need to be coated to avoid agglomeration and degradation. The election of the material of the shell is usually based on the size of the particles and the environment they are to be used in. Furthermore, the functionalization of these core-shell systems can also be an extra benefit, so it is better to chose easily functionalized materials for the shell if the application requires it.

In this thesis the production and characterization of aqueous and organic iron oxide nanoparticles and stabilized by different coatings for their application in nanobiomedicine are reported.

In chapter 1, a brief introduction about biomedical applications of nanoparticles is reported. There are also described some especial magnetic properties that are observed in nanoparticulate materials that can be useful for the design of new core-shell materials for biomedical applications. Eventually, the purpose and goals of this thesis are exposed.

The methods and the synthesis and characterization of aqueous and organic ferrofluids are described in chapter 2. These ferrofluids are mentioned later in other chapters because they are the former particles, and from them, several studies were performed and explained in chapters 3, 4 and 5.

Chapter 3 is about how to obtain aqueous dispersions of high quality iron oxide nanoparticles synthesised in organic solvents. For this purpose, a ligand exchange technique is used, which consists on the substitution of the hydrophobic ligand used in the organic synthesis by a hydrophilic ligand.

Chapter 4 describes the contribution to the design and development of a biosensor based on impedance measurements that are made in order to improve the signal. A multi-core-shell structure is functionalised with a siloxane ended in a carboxylic group. This group is able to bond an antibody that can interact with the capacitor of the biosensor, changing the signal.

Chapter 5 describes a multifunctional multi-core-shell system that is able to combine the magnetic properties of the superparamagnetic nanoparticles of the core and the pH response of the polymer that forms the shell. This system can be used in biomedical applications with some modifications.

Chapter 1

Introduction and goals

1.1 Advantages of MNPs in biomedical uses

The use of magnetic nanoparticles (MNPs) in biomedicine began at the end of the 70s when they were employed as enzyme carriers (Magnogel, Dynabeads and Estapor) in bioanalysis [1, 2]. Since then, they have been used in many other biotechnological applications such as biocatalysis, bioprocessing, separation and purification. In biocatalysis, it is well known that homogeneous catalysts are more efficient than heterogeneous ones, but they are very difficult to remove from the medium after reaction. MNPs are very helpful for this task because when they are used as support for the catalysts they can be easily separated from the reaction medium with a magnet [3]. In bioprocessing, the magnetophoretic behaviour of MNPs can improve the mobility of a biosystem to perform bioseparation and target isolation under a continuous flow processing conditions [4]. For separation and purification, magnetic solid-phase extraction is a widely used technique. The typical procedure is to functionalize the target with MNPs that can interact with a magnetic adsorbent. Then, the target contained in the absorbent is recovered from the solution in a magnetic separator [5]. The physical principle behind these applications is simple: the magnetic particle is attached to a biological molecule (enzyme, cell, antibody, DNA, etc.) and the magnetic moment of the particle is used to move or fix the biomolecule with an external magnet.

In the 80s, MNPs were commercially used for the first time in clinical applications, as contrast agents in Magnetic Resonance Imaging (MRI) [6]. This application is based on the effect of MNPs on the relaxation time of neighbouring water protons, especially on spin-spin relaxation time t_2 [7, 8].

An additional and interesting application of MNPs already in the market is biosensing [9]. It is important to highlight the importance of magnetic nanoparticles for detection of biomolecules and cells based on magnetic resonance [10]. Baby and col. fabricated an amperometric biosensor by deposition of glucose oxidase over a Nafion-solubilized Fe_3O_4@SiO_2 electrode, which retains its biocatalytic activity and offers fast and sensitive glucose quantification [11].

Another exciting clinical application of MNPs is found in hyperthermia cancer therapy [12]. When superparamagnetic nanoparticles are exposed to an alternating magnetic field, they produce heat that can be used to heat cells over 42–45ºC causing cellular death. Tumour cells are more sensitive to heat than healthy cells so it is expected to achieve a higher population of death tumour cells [13].

Other biomedical use of MNPs that has been further developed in the last decade is targeted drug delivery. Systemic disease treatments require a large drug doses to achieve high local concentrations that produces undesired side effects elsewhere. This can be avoided with drug targeted administration. In magnetic targeting, the drug is attached to a MNP than can be directed to the desired zone with a magnetic field. This system can be reinforced by biological specific vectors implemented in the surface of MNPs that are capable of specific recognition and binding to the target site [14]. Recently, a most promising area of application of MNPs in medicine has emerged, namely theranostics, which is based in performing therapy and diagnosis simultaneously [15].

Besides their unquestionable biomedical interest, MNPs have a large variety of industrial applications such as polymer processing through homogeneous heating or selective heating, soldering or glue-welding procedures, magnetic recording, magnetic refrigeration, magnetic printing, lubrication and sealing in vacuum systems, magnetic sensors, and others [16].

Nanoparticulate materials open a new opportunity to study at the molecular and cellular levels. Therefore, promoting fast advances in life sciences and healthcare

because they are capable to pass barriers that bigger systems cannot. Small size is a great advantage of NPs, although not the only one arising from their unique properties with respect to bulk materials, which can be even more important for biomedical applications. One of these properties of MNPs is superparamagnetism. When a magnetic field is applied, the MNPs give a magnetic response, but when the field is removed, no remanent magnetization is observed. This is very important in order to avoid magnetic agglomeration when the influence of the magnetic field is taken away. The magnetic response of nanoparticles strongly depends on their morphology, crystallinity and size, therefore controlling these characteristics is of great interest to have a fine control on the MNPs properties.

Most biomedical applications require specific MNPs characteristics. Ideally and for optimum use, nanoparticles of homogeneous size and uniform shape are desired. It would be interesting to have a procedure that permits the production of controlled nanoparticle diameter in the order of nanometers. Good crystallinity and phase control are also desirable tunable properties. MNPs also must have good thermal stability, biocompatibility, and an adequate magnetic moment. It is important as well that they form stable dispersions in biological fluids, such as blood. MNPs can be coated with biomolecules in order to increment the residence time in the blood circulation systems or to make them interact with a cell or a biological entity.

As we mentioned before, in order to design a potential biosystem it is very important to take into account the requirements of the applications it is conceived for. Each application needs different features from the magnetic nucleus and from the coatings to obtain the optimum response of the system, as it will be commented in the following sections.

1.1.1 MRI

In recent years, medical imaging research has experienced immense improvements with the introduction of techniques such as Magnetic Resonance Imagine (MRI). In this technique, contrast agents are often needed in order to improve the diagnosis. Magnetic nanoparticles systems are good candidates for this purpose, especially, superparamagnetic iron oxide nanoparticles [17]. Superparamagnetic iron oxide nanoparticles modify the relaxation time of water protons changing the contrast image intensity of the tissue where they are present [18]. In order to avoid particle aggregation and improve stabilization, the iron oxide nanoparticles are covered by a coating. This coating may also be used to facilitate the distribution of the particles in the tissue and to add new functionalities to the system as described below.

Some requirements are needed to create an ideal contrast agent system, for example, the system has to be homogeneous in size because it is important to get a uniform distribution in the tissue, and the hydrodynamic radius has to be small in order to get long blood circulation time. It is also important to control the magnetic properties. In order to be superparamagnetic, the particle size has to be smaller than 25–30 nm. Moreover, the particle morphology has to be homogeneous, and the size distribution must be narrow, to achieve consistent results. The surface properties are also relevant for this application. It has been shown that surface modification with hydrophilic molecules such as PEG increases circulation times. An additional advantage of PEG coating is that it enables particles to cross cell membranes because PEG is soluble in both polar and non-polar solvents and it has high permeability in cell membranes [19]. Another possible coating is silica as shown by Taboada et al., who presented a system composed by monodisperse iron oxide and microporous silica core/shell nanoparticles of around 100 nm in diameter. This system has a high magnetization and may be particularly useful as an enhanced T2 imaging agent [20].

1.1.2 Magnetic hyperthermia

The amount of heat released by MNPs under an alternating magnetic field is a promising tool for biomedical applications based on hyperthermia [21] and on thermally assisted drug delivery [22]. The use of superparamagnetic nanoparticles for hyperthermia purposes was first introduced by Jordan et al. in 1993 [23]. Further studies have demonstrated that magnetic hyperthermia could be an alternative to current therapeutic approaches for cancer treatment, by inducing tumour regression in combination with other toxic agents, or by causing necrosis of cancerous cells [24-26]. Hyperthermia is also producing a strong enhancement of radiation damage. For instance, a local heating of 43.5°C for 1 hour yields an approximate enhancement ratio of 5 [27]. According to Rosenzweig, a ferrofluid subjected to an alternating magnetic field produces a power dissipation that comes from the orientational relaxation of particles having thermal fluctuations in a viscous medium [28]. From the point of view of the study of hyperthermic behaviour of magnetic iron oxide nanoparticles some work has still to be carried out in order to confirm Rosenzweig theoretical predictions. The heating capacity of MNPs is quantified by the specific absorption rate (SAR), which accounts for the heating power per mass unit of dissipating material. This magnitude depends on the MNPs characteristics, such a phase composition, particle shape, magnetic anisotropy, mean size and size distribution, as well as on the alternating magnetic field parameters, such as amplitude and frequency [29]. With respect to the particle size, Rosenzweig reported a very sharp maximum of SAR at 14 nm in case of magnetite nanoparticles. For the case of maghemite and magnetite nanoparticles, widely used due to their biocompatibility, small particles in the order of 10–15 nm in diameter are desired because they lie well below the critical size of single domain particles. In this size range, the heat dissipation is due to the thermal relaxation of magnetic moments [29], the heating power decreases strongly with the size dispersion [28]. The heating capacity is greatly influenced by nanoparticle environment, and the degree of particle aggregation. Therefore, a protecting nanoparticle coating is highly important for hyperthermia applications.

1.1.3 Biosensors

Sensing was the first application of magnetic nanoparticles in biomedicine and this area continue to rapidly evolve with very important developments and future perspectives in this area. An example is the work of Han et al., who have reported extensively on the use of functionalized magnetic micro- and nanoparticles for biosensing. These authors have proposed a sensing system based on the absorption of magnetic particles by hybridized DNA that alters the sensor resistance and generates electrical signals that can be directly measured. In this system, the cells are first treated with a biotinylated primary antibody or ligand. Then, they are magnetically labelled with streptavidin coated magnetic beads. Under an electromagnetic field, the magnetic labelled cells are retained in a column containing a magnetically soft material, whereas the unlabeled cells will just flow through [30]. Another effective material for biosensing is that composed by core/shell iron oxide MNPs coated with gold as is reported by Wang et al. [31]. This system has been used as a solid support for goat anti-human antibody IgM, which could be immobilized on the surface of a surface plasmon resonance biosensor.

1.1.4 Drug delivery

Nowadays nanobiosystems are of great interest in drug delivery. Novel nanoparticles are designed to alter their structure and properties during the drug delivery process to make them most effective for distribution [32]. This alteration can be achieved through the incorporation of materials that are able to respond to physical or biological stimuli, including changes in pH, redox potential or enzymes. The idea of employing MNPs for drug delivery was proposed by Widder and Senyei in 1978 [33, 34]. The basic argument is that therapeutic agents are encapsulated or attached to MNPs. These particles may have magnetic cores protected with a stabilizing material like polymers or other kind of coatings which can be functionalized. They may also consist of porous polymers containing MNPs precipitated within the pores [35-37]. Advantages of the use of these devices are conjugation with biological ligands and also the possibility to increase the circulation time of MNPs in the blood stream [38].

1.1.5 Targeting

Ideally, the treatment of local diseases should be local therapy, but when the disease problem is inaccessible to common local treatments, a systemic treatment is often used. This requires the administration of large amounts of drugs with the consequent side effects. The use of drug targeting allows reduction of drugs quantities that diminishes the side effects and increases the treatment efficacy. Although magnetic targeting has been successful in a number of studies, there are only a small number of clinical trials. Lubbe et al. carried out a clinical study in mice and rats where two forms of treatment were studied [39]. Epirubicin, a well-know drug that is widely employed for chemotherapy, was attached to MNPs by electrostatic interaction, and the mechanical occlusion of the tumour with high concentrations of ferrofluid was studied as well as the targeted delivery of epirubicin with low nanoparticle concentration. As in many other related *in vivo* studies, the particles not attached to the tumour were accumulated in the liver and spleen and not harmful effects on organ functions were observed.

Novel strategies are being developed for applying magnetic fields and MNPs which could lead to new treatments. Rapid developments in particle synthesis have enabled the use of new materials for more efficient capture and targeting. In order to design an efficient biosystem, it has to be taken into account that the nanoscale dimensions of particles should allow them not only to pass through the blood vessels but also to penetrate cell membranes when necessary [40]. Chemotherapeutic agents require internalization and slow drug release, gene therapy demands positive interaction with the nucleus, radiotherapeutic systems requires cellular internalization. The maximum size that can be used for a biosystem is 1.4 μm in diameter to avoid capillary occlusion.

A great number of chemical methodologies have been used for the conjugation of targeting molecules with the biosystem surface. The primary goal is to bind the targeting molecule without compromising its functionality once attached. For example, if an antibody is bonded to the particle surface and its active site is covered,

it may loose its capacity to bind a target [41]. Some of the most interesting candidates for being targeting molecules are tumoral markers for brain and gene therapy, such as siRNA or Tat that facilitate intracellular delivery [42]. Another interesting possibility of targeting consists of magnetic targeting. In magnetic targeted drug delivery, the systems formed of coated MNPs loaded with anti-cancer drugs are injected into the body via the blood circulatory system. An external magnetic field is used to localize the biosystem at the tumour site and the drug can then be released from the system via enzymatic activity or changes in physiological conditions such as pH or temperature and be taken up by tumour cells [43]. Alexiou et al. showed that magnetic targeted drug delivery caused complete tumour remission in rabbits without any negative side effects and allowed a drug dose reduction of 20% of the usual dose [14].

1.2 Magnetic properties of nanoparticles

All materials can be classified by their magnetic response to an external magnetic field. This response is related to the magnetic interactions of the constituent atoms and the crystalline structure of the material [44]. The main types of magnetism include diamagnetism, paramagnetism and ferromagnetism. Antiferromagnetism and ferrimagnetism are considered to be subclasses of ferromagnetism. In Figure 1.1, it can be observed the different possible orientation of magnetic moments. Below a certain magnetic ordering temperature, ferromagnetic materials exhibit parallel alignment of permanent magnetic moments resulting in a large net magnetization that can remain in the absence of a magnetic field. Two characteristics, albeit not exclusive, of ferromagnetic materials are their spontaneous magnetization and the existence of hysteresis. In ferrimagnets, the moments of adjacent atoms or ions are in an antiparallel alignment, but they do not cancel to each other.

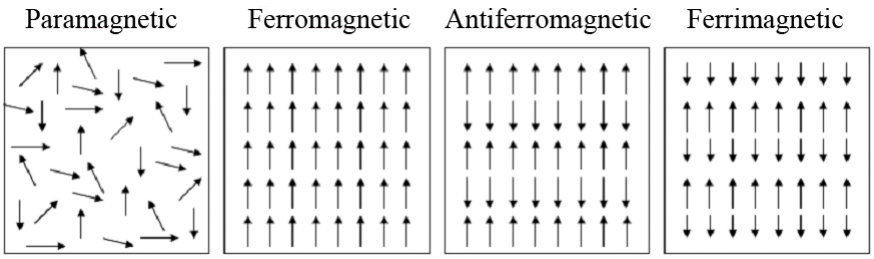

Figure 1.1 Possible magnetic moments orientation.

An example of a ferrimagnetic mineral is magnetite (Fe_3O_4). Ferrimagnetism exhibits all the properties of ferromagnetic behaviour like spontaneous magnetization, Curie temperatures (T*c*), hysteresis, and remanence. However, ferro and ferrimagnets have very different magnetic ordering.

Below a critical temperature, T*c*, the moments in a ferromagnet order and align parallel to each other. However, in order to minimise the magnetic free energy, the whole magnetic structure splits in small-volume regions known as domains, in which there is mutual alignment of the magnetic moments in the same direction, as illustrated in Figure 1.2. Each domain is magnetized to its saturation magnetization, adjacent domains being separated by domain walls.

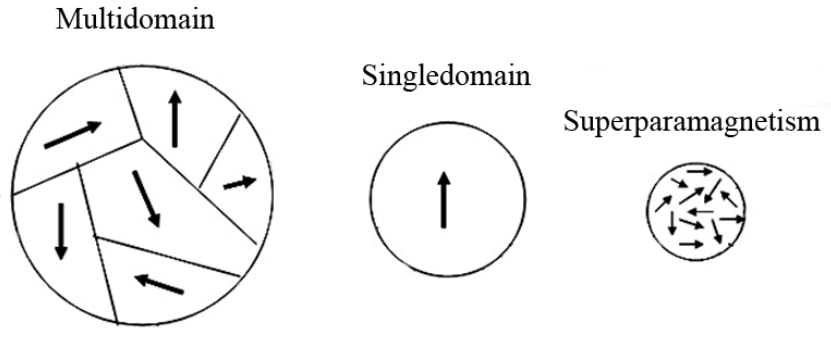

Figure 1.2 Nanometric magnetic structures above T_C.

Ferromagnets can retain a memory of an applied field even after the field is removed. This behaviour is called hysteresis and the plot of the variation of magnetization with magnetic field is called hysteresis loop. The hysteresis loop is useful to characterize magnetic materials and various parameters can be determined from it.

It is well known that magnetism and most of the physical properties of materials depend on their size, particularly when the size reaches the nanometer range (1–100 nm) [45] (see Figure 1.2). There are two main sources for that: (1) size effects, when the particle size becomes smaller than that of magnetic domain, the mechanisms of magnetization reversal change, something that affects magnetization properties particularly the saturation and remanent magnetizations, the coercive field and the magnetic anisotropy; and (2) surface effects, when the surface/volume ratio increases, structural and magnetic surface disorders become increasingly influential. These circumstances cause the apparition of unique magnetic phenomena not found in bulk materials, such as superparamagnetism, giant magnetoresistance [46], quantum tunnelling of magnetization [47], and large coercivities [48]. In sufficiently small magnetic particles, ferro or ferrimagnetic, a phenomenon that is known as superparamagnetism, can be observed. When an external magnetic field is applied to superparamagnetic nanoparticles, the magnetic moments tend to align along the magnetic field, leading to a net magnetization. When the magnetic field is removed, the magnetic moments will not randomize their direction immediately, but rather it will take some length of time to do so and no remanent magnetization is kept as it can be seen in Figure 1.3. This behaviour can be useful in biomedical applications, as we will see later.

1.2.1 Superparamagnetism

The first consequence of size reduction is the formation of single domain particles. At a temperature below T*c*, ferromagnets are composed of small-volume regions known as domains, in which there is mutual alignment of the magnetic moments in the same direction, as illustrated in Figure 1.2. Domains are formed in

order to reduce the magnetostatic energy of the system. Each domain is magnetized to its saturation magnetization, adjacent domains being separated by domain walls where the spins gradually rotate between the respective spin orientations of neighbouring domains.

In single domain particles, the anisotropy energy barrier that prevents the reversal of magnetization direction depends on the size. When the size is reduced below a point (below 25–30 nm in magnetite or maghemite), the anisotropy energy becomes lower than the thermal energy, so the particle cannot maintain a fixed orientation of the magnetic moment and becomes superparamagnetic. The resulting fluctuations in the direction of magnetization cause the magnetic field to average zero. The material behaves in a similar way to a paramagnet, except that instead of each individual atom being independently influenced by an external magnetic field, the magnetic moment of the entire particle tends to align with the magnetic field. At temperatures below T_B, when the applied field is removed, the particle magnetic moment takes time to recover its initial state by thermal influence. In sufficiently small particles, with an effective uniaxial anisotropy constant, the relaxation of the magnetization will vary exponentially with the temperature following a Néel-Brown process [1, 49, 50].

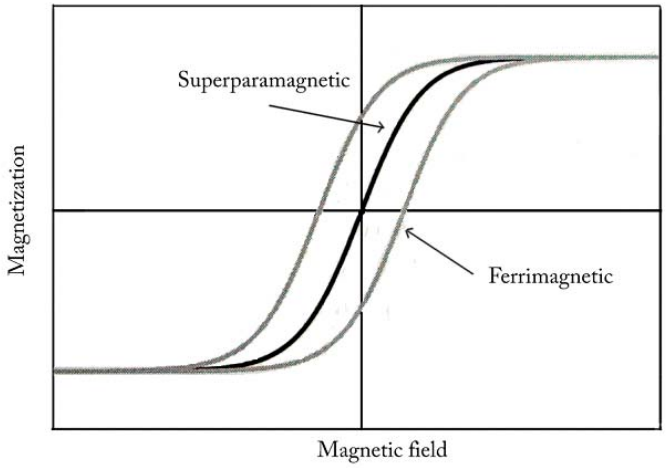

Figure 1.3 Ferrimagnetic and superparamagnetic behaviour.

1.2.2 Magnetic relaxation

There are two main mechanisms of particle relaxation (Figure 1.4): spin rotation (Néel relaxation) and particle rotation (Brown relaxation). The time required for the reversal of the magnetic moment of the particle (spin rotation) is related to the magnetic anisotropy of the material.

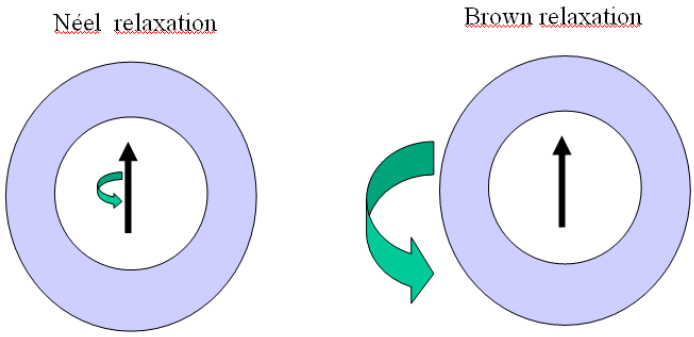

Figure 1.4 Nanoparticle magnetic relaxation.

The existence of different particle sizes and shapes leads to a distribution of relaxation times, with an average value τ that in general is also temperature dependent. The time τ is then the average time needed for a given kind of particle to reverse its magnetization after removing the external applied field. The practical consequence is that when the measuring time τ_m, is greater than τ it can be observed a superparamagnetic behaviour. However, for $\tau_m < \tau$ the complete reorientation of the magnetic moments of the cluster cannot take place during the measuring time. Thus, below a blocking temperature T_B, given by the condition $\tau(T_B) = \tau_m$, the system appears "blocked" and its behaviour is strongly dependent on τ_m.

There are a large amount of techniques to experimentally observe superparamagnetism: magnetization, ac susceptibility, neutron scattering and Mössbauer spectroscopy. Since each of these experimental techniques has a characteristic measuring time, which ranges from 10–100 s for dc magnetization

measurements to 10^{-114} -10^{-12} s for neutron scattering experiments, each one can provide information from different relaxation rates.

1.2.3 Specific absorption rate

The history of hyperthermia with MNPs in alternating magnetic fields started in the late 1950s, but most of the studies were unfortunately conducted with inadequate animal systems, inexact thermometry and poor magnetic field parameters, so that any clinical implication was far behind to be useful [51].

More than three decades later, it was found, that colloidal dispersions of superparamagnetic nanoparticles exhibit an extraordinary specific absorption rate. Heating of certain organs or tissues to temperatures between 41°C and 46°C, preferentially for cancer therapy, is called hyperthermia. Higher temperatures, up to 56°C, cause cellular necrosis or carbonization, and it is called thermoablation. Both mechanisms act completely different concerning biological response and application technique [52]. The classical hyperthermia induces irreversible damage to cells and tissues, but hyperthermia is also used to enhance radiation injury of tumour cells and chemotherapeutic efficacy. Modern clinical hyperthermia studies focus mainly on the optimization of thermal homogeneity at moderate temperatures (43°C) in the target volume, a problem requiring extensive technical efforts and advanced therapy and thermometry systems.

The most important parameter that determines the quantity of heat that magnetic particles can produce is the specific absorption rate. This value is defined as the rate at which the electromagnetic energy is absorbed by mass unit. It is proportional to the rate of the temperature increase ($\Delta T/\Delta t$), and is expressed in calories per kilogram:

$$SAR = C_t\left(\frac{\Delta T}{\Delta t}\right) \qquad \text{(Eq. 1.1)}$$

where C_t is the total specific heat capacity of the entire sample. Based on the Brown and Néel relaxation, it has been shown, that single domain particles (nanometer

in size) absorb much more power at tolerable alternating magnetic fields than multidomain particles (microns in size) [23].

1.2.4 Surface effects

For very small particles, as the particle size decreases, the surface/volume ratio increases and surface effects become increasingly important [47, 53, 54], see Figure 1.2. The lattice symmetry breaks at the surface resulting in large perturbations in crystal and electronic structures. Differences in the magnetocrystalline anisotropy with respect to the core and spin disorder are observed, particularly in ferrimagnets. Surface ions have incomplete coordination shells, which alters their spin orientation producing a disorder near the surface and a reduction of the magnetization as compared to bulk [47, 54–57]. In the case of antiferromagnetic particles, the formation of net magnetisation has also been observed and it is associated to uncompensated moments and spin canting due to the breaking of symmetry and differences in the magnetocrystalline anisotropy at the surface [58, 59].

Surface effects can be further enhanced by the particle coating. Interactions between an inorganic coating or a polymeric matrix and the nanoparticles have the effect to introduce some further disorder at the particle surface, particularly in the presence of strong covalent bonds between the particle and the coating.

1.3 Core-Shell structures of MNPs used in medicine

In general, MNPs used in biomedical applications have the following structure: (1) one or several magnetic nucleus; (2) a biocompatible shell that permits a good stability of the particles in biological media, and have binding sites for the anchoring of physical and/or biological functionalities; (3) a biological vector (antibody, DNA, peptide, oligosacharide, etc.) capable of binding to the target biological entity (macromolecules, cells, tissues, etc.); and (4) a therapeutic agent (drugs, enzymes, etc.). The scheme of a typical biosystem is described in Figure 1.5. An obvious condition in biomedical applications is that the materials have to be biocompatible.

This requirement restricts severely the type of compounds used for the magnetic nucleus and the shell.

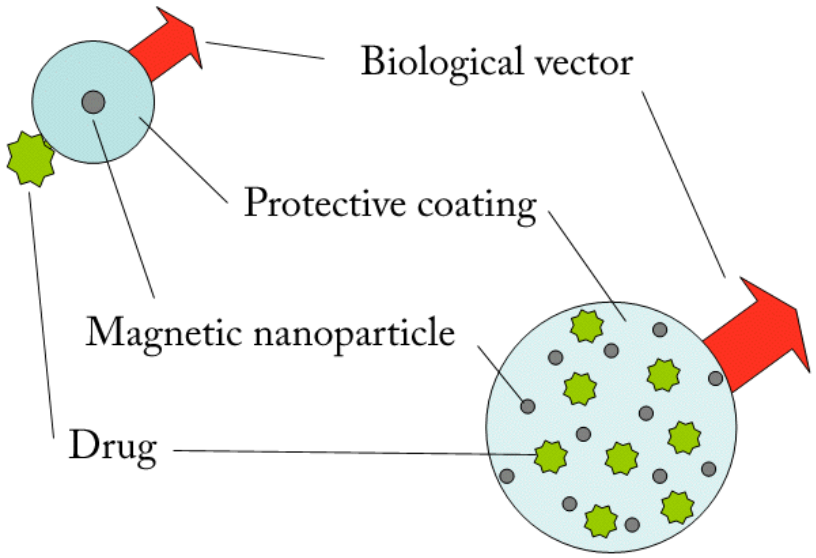

Figure 1.5 Components of biological systems.

From this general scheme, the structure and size of MNPs can vary depending on the desired application. Thus MNPs for "in vitro" applications in biosensors or in magnetic separation must have a size large enough to reach a sufficient magnitude for the magnetic moment or to be confined in liquid permeable chambers. In these applications, the size of the magnetic nucleus is usually in the range from 10 nm to 50 nm in diameter and the total size is between 0.1 μm and 10 μm. However, in *in vivo* applications the size must be small enough to permeate biological barriers, and therefore typical sizes of MNPs for MRI are 2 to 50 nm for the core and 7 to 400 nm for the entire particle.

For instance, in magnetic hyperthermia therapy, only MNPs in a narrow size range contribute to the SAR for a given frequency of the alternating field. Other relevant structural factors are: internal structural disorder [1], aggregation [60], and interparticle separation [61]. In order to find an optimum magnetothermal behaviour, it is necessary to have a system in which these factors can be varied independently, while keeping a narrow size distribution.

1.3.1 Materials for the core

The most common magnetic materials are composed by Fe, Co, Ni, their oxides and their alloys. Actually, the minerals magnetite (Fe_3O_4) and maghemite (γ-Fe_2O_3) are typical examples of ferrimagnetic materials. It is well known that maghemite and magnetite are biocompatible materials [62]. Maghemite has the advantage over magnetite that it is more stable because it is the oxidized form of magnetite. So among the magnetic compounds, γ-Fe_2O_3 is the one that provides the best expectations for use in living organisms together with a fine magnetic performance. In fact, there are many iron oxide-based particles in the market for biological applications. For example, superparamagnetic contrast agents used for MRI consist of maghemite-magnetite cores encapsulated in a polisacharide of dextran family or other coatings like Endorem (nanoparticles of 4-15 nm in diameter coated with dextran, with a total hydrodynamic diameter of 150 nm), Sinerem (nanoparticles of 4-15 nm coated with dextrane, hydrodynamic diameter: 30 nm), and MION-46 (nanoparticles in the order of the 20 nm of hydrodynamic diameter coated with dextrane) [63].

Apart from iron oxide nanoparticles, other magnetic nanoparticulate materials have been employed in biomedical applications. Recently, gadolinium hexanedione nanoparticles of about 140 nm in diameter, fabricated in microemulsions [64] have shown greater image enhancement ability than commercial gadolinium molecular products, and they are non-toxic for human stem cells. $Mn_xZn1_{-x}Fe_2O_4$ nanoparticles have been investigated as hyperthermia agents with the aim to improve heating temperature, SAR and biocompatibility [65]. Also in this field, monodisperse metastable Fe-Ni MNPs, synthesized by chemical reduction, showed tuneable Curies

temperatures. This is particularly important because it opens the possibility of self-regulated heating of cancer cells, as the Curie temperature sets an upper limit to heating preventing the damage to neighbouring healthy tissue [66]. Magnetic nanorods composed of Ni and Au, synthesized by electrodeposition into a porous alumina membrane, have been proposed for biomolecular separation [67]. Moreover, biofunctionalized FePt MNPs (3-4 nm) have been successfully used for rapid detection of gram-positive bacteria at very low concentration [68]. Therefore, we can conclude that there is good variety of magnetic nanomaterials susceptible for being employed in biomedical applications. In the work described here and in spite of the moderate magnetic performance of iron oxide MNPs, we decided to use them because of their biocompatibility advantage over other materials.

1.3.1.1 Iron oxides: An introduction

Iron oxides are the result of iron metal in contact with the atmosphere, which contains oxygen. So, iron oxides exist in the earth as long as both iron and oxygen have been on the planet. Iron oxides present a large variety of crystal phases. There are 16 known iron oxides, hydroxides and oxide-hydroxides [69]. Among them, only magnetite (Fe_3O_4) maghemite (γ-Fe_2O_3) and lepidocrocite (γ-FeOOH) are ferrimagnetic, the rest being antiferromagnetic or weakly ferromagnetic.

Magnetite is black, ferrimagnetic, and contains both Fe(II) and Fe(III). The structure is an inverse spinel, and it was one of the first minerals being studied by XRD. It has a face-centered cubic unit cell with an edge length of a = 0.8394 nm, and 8 formula units. The formula can be written as $Fe(III)[Fe(II)Fe(III)]O_4$, and the structure can be seen as an inverse spinel where octahedral (Oh) sites are occupied by both Fe(II) and Fe(III) ions, whereas tetrahedral (Td) sites are occupied by Fe(III), see Figure 1.6. This mineral is frequently non-stoichiometric with a deficient Fe(III) sublattice.

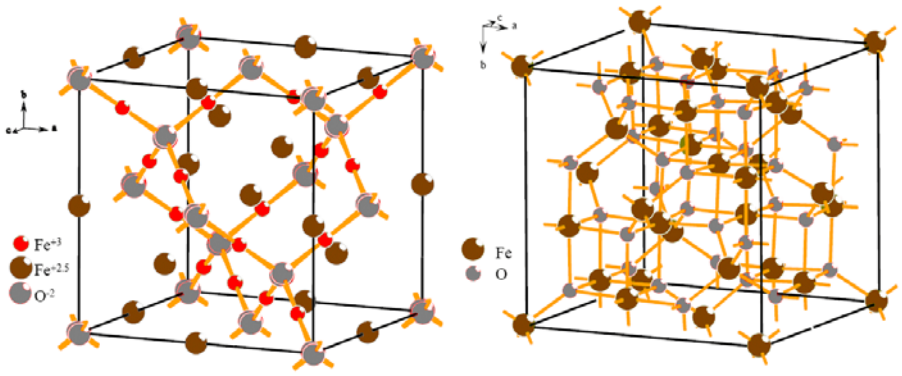

Figure 1.6 Crystalline structure of magnetite (left) and maghemite (right).

Maghemite is brown-red, ferrimagnetic, and all of the iron ions in the structure are trivalent. The structure is also a inverse spinel, thus, to compensate the higher charge in the structure, cation vacancies are created. Each cell of maghemite contains 32 O^{2-} ions, 21 Fe(III) ions and 2 vacancies. The 8 Fe cations occupy Td sites and the other are distributed in the Oh sites, as shown in Figure 1.6. The vacancies are confined in the Oh sites. The unit cell edge is 0.834 nm, slightly shorter than that of magnetite. The oxidation of magnetite takes place by migration of Fe(II) cations from the inside to the outside of the particle, creating the vacancies (□). Then, Fe(II) cations are oxidized to Fe(III) at the surface generating maghemite [70]. The resulting formula structure can be written as follows:

$$[Fe_8{}^{3+}]_{Td}[Fe_8{}^{3+}Fe_8{}^{2+}]_{Oh}O_{32} \rightarrow [Fe_8{}^{3+}]_{Td}[Fe_8{}^{3+}Fe^{3+}{}_{5.33}\square_{2.66}]_{Oh}O_{32}$$

In the case of magnetite, Fe(III) ions are equally split between Oh and Td, they are coupled antiferromagnetically, and hence do not contribute to the magnetic moment. The magnetic moment of magnetite is therefore due to the contribution of Fe(II) ions occupying Oh sites, which have a moment of 4 μ_B. The sublattice of Fe(III) in the Td sites has magnetic moment of 40 μ_B (8 cations x 5 μ_B) and the sublattice made of Fe(II) and Fe(III) in Oh sites has 72 μ_B (40 μ_B from Fe(III) and 32 μ_B Fe(II)). The total magnetic moment of the two combined sublattices is 32 μ_B. The saturation

magnetization of bulk magnetite is 84 emu/g at room temperature, and the Curie temperature is 850 K.

$$[Fe^{3+}\uparrow]_{T\,d}\,[Fe^{2+}\downarrow, Fe^{3+}\downarrow]_{Oh}\,O_4$$

In maghemite the magnetic structure consists on two sublattices corresponding to the Fe(III) located on Td and Oh sites. The spins in each sublattice align ferromagnetically, but the spins between the sublattices align antiparallel. Ferrimagnetism arises from decompensation between the number of Fe(III) cations in each sublattice. The sublattice that consist on Fe(III) in Td sites is 40 μ_B and for Oh sublattice is 66.7 μ_B (40/3 cations in Oh sites). The total magnetic moment is 26.7 μ_B. The saturation magnetization of bulk maghemite is 74 emu/g at room temperature, and the Curie temperature is in the range of 820–986 K. Maghemite has a phase transition to hematite at 800 K.

$$[Fe^{3+}\uparrow]_{T\,d}\,[Fe^{3+}{}_{5/3}\downarrow, \square_{1/3}]_{Oh}\,O_4$$

1.3.1.2 Synthesis of iron oxide MNPs

The preparation of iron oxide nanoparticles can be realized through bottom-up or top-down methods. The top-down approach is based on solid phase procedures. In the first known method for the production of iron oxide nanoparticles, large iron oxide materials are broken down to smaller particles by means of mechanical milling. But this method has a long preparation time and generates very high size dispersion [71]. In a bottom-up process, small building blocks such as atoms or clusters are assembled into nanoparticles. This approach includes chemical synthesis in solution and gas-phase routes [72, 73]. Various synthetic strategies for the preparation of MNPs have been investigated, including chemical co-precipitation [74], microwave heating [75], micro- and nanoemulsion [76], sol-gel [77], hydrothermal routes [78], high temperature decomposition [79], sonochemical reactions [80], and laser pyrolysis [81].

Emulsion methods use two immiscible liquids, an organic solvent and an aqueous solution, in which small droplets are formed. The dispersion is achieved by

mechanical mixing that forms a non-stable droplet dispersion, however the addition of surfactants improves both stability and homogeneity. Organic and aqueous solvents often contain several dissolved components that allow nanoparticles formation, consequently this system behaves as a micro- or nano-reactor, depending on the droplet size. The temperature and surfactant concentration permit size and shape control of the obtained nanoparticles because they control the droplets size. This procedure is inexpensive and rapid but cumbersome for large-scale production [76].

The co-precipitation procedure consists on the treatment of a mixture of different metal precursors with a base in an aqueous medium. Complete precipitation can be obtained at a pH between 8 and 14. The main advantage of co-precipitation is that a large amount of nanoparticles can be synthesized. However the control of particle size distribution is limited because kinetic factors are the only controlling factor of the growth process [74].

Microwave co-precipitation allows a fast heating of the reaction mixtures, especially those containing water, so the formation of MNPs occurs almost immediately. This leads to very small particle sizes and narrow size distributions. This method offers the additional benefit of very short reaction times [75]. The main drawback is agglomeration, so an additional size-sorting process is needed.

As in microwave heating processes, sonication of a liquid also produces rapid heating, but the precipitation mechanism goes through acoustic cavitation, which is the formation, growth, and collapse of a bubble in an irradiated liquid. This generates a transitory localized hot spot, with an effective high temperature (more than 700ºC) and a short lifetime (less than 1s). The chemical reactions take place inside the bubbles. One advantage is that no surfactant is used. The disadvantages are that amorphous materials are always obtained whenever a volatile liquid is used, and cooling rates are large. Nevertheless, the sonochemical decomposition of metal carbonyls in alkene solvents has been widely used to prepare iron metallic nanoparticles [80].

Hydrothermal reactions are performed in reactors that permit high pressure and temperature conditions. Most of the solvents in these methods are polar, such as water, methanol or isopropanol, but also other organic solvents have been used. Two main chemical routes are employed to obtain iron oxide nanoparticles in hydrothermal methods: hydrolysis/oxidation, and neutralization of mixed metal hydroxides [78]. In the well-known polyol process, a metallic precursor is dissolved in polyethylenglicol or pyrrolidone solvent and the solution is stirred and heated to reach the boiling point to get metal nanoparticles that are later oxidized. By controlling the precipitation kinetics, well-dispersed iron oxide MNPs with well-defined shape and size can be obtained [82].

In liquid aerosols routes, particles are obtained by spraying a solution into a series of reactors where the aerosol droplets evaporate. If the key step is drying, the technique is called aerosol evaporation, and when a thermolysis process is involved, it is called spray pyrolysis. Most of the pyrolysis techniques used to produce iron oxide nanoparticles start with an Fe(III) salt in a solution containing an organic reducing agent. This method is simple, rapid and continuous, but the obtained particles are often difficult to coat [81].

Sol-gel methods consist on the hydrolysis and condensation of alkoxide-based precursors at low temperature. This method starts from a chemical solution (sol) that acts as the precursor for an integrated network (or gel) of discrete particles. Typical precursors are metal alkoxides, such as tetraethyl orthosilicate (TEOS) or alkoxysilanes, and metal chlorides, which undergo a series of hydrolysis and condensation reactions in aqueous media. One of the advantages of sol-gel methods is the low reaction temperature that enables small particles to be grown. The main drawback is that the resulting particles are not homogeneous in size and shape [77].

The method allowing higher level of monodispersity and size control in iron oxide nanoparticles production (see Figure 1.7) is probably thermal decomposition of iron organic precursors, such as $Fe(Cup)_3$, $Fe(CO)_5$, or $Fe(acac)_3$, in organic solvents, and in the presence of surfactants. The particle diameter can be tuned from 4 to 20 nm,

and the hydrophobic particles can be transformed into hydrophilic ones by adding a bipolar surfactant [79] and [83]. However, this process must be improved, especially in terms of reactants safety and high temperatures required, in order to be suitable for industrial preparation.

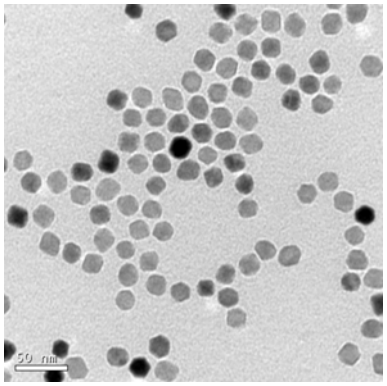

Figure 1.7 Iron oxide nanoparticles obtained by thermal decomposition of metallorganic precursors.

Nanoparticles growth in confined spaces is another methodology to achieve size control in nanoparticles. Superparamagnetic nanoparticles can be obtained by controlling the gelation time of a mesoporous material and an iron oxide precursor [84]. Mixtures of TEOS and alcoholic solutions of iron nitrate generate iron oxide nanoparticles homogeneously dispersed in the silica matrix [85]. Polymers can act as confined spaces as well, and the synthesis of tuneable size nanoparticles can performed using these conditions [86-88].

Reverse micelles are shown to be a suitable procedure to achieve nanoparticles with a tailored size, which can be controlled by modifications in the reaction temperature, the concentration of the precursor, or the water:surfactant ratio [89-91].

1.3.1.3 Strategies for the control of size in nanoparticles

In order to obtain MNPs, direct precipitation methods are of great interest because a certain control of particle size can be achieved by adjusting the conditions of reaction. In batch precipitation systems, the supersaturation decreases as nucleation and growth occurs, and so does the growth rate, thus limiting the maximum size. Low solubility, fine mixing of reactants and temperature are also factors that may help to control the size and size dispersion in these systems. A typical example of direct precipitation method is the popular Massart method. There, iron oxide nanoparticles are precipitated by addition of a base to a solution of Fe(II) and Fe(III) salts in a 1:2 ratio, at a pH between 8 and 9.6. The size varies with the strength of the precipitating base [92], so that a stronger base leads to larger particles (NH_3: 6 nm, CH_3NH_2: 10 nm, NaOH: 19 nm). This strategy is not sufficient to ensure a narrow size distribution that is usually in between 20% and 30%. A higher control can be obtained with the ratio of reactants in the reaction medium. This is very efficient in organic solution precipitation, but it is far less effective in aqueous media due to the strong solvation capacity of water. The size distribution can be further narrowed by size-sorting procedures, such as centrifugation [93], size-selective precipitation [95], magnetic separation [95], field-flow fractionation and size-exclusion chromatography [96].

The size dispersion associated to direct precipitation methods can be largely avoided by the use of additives that adsorb on the particle surface and inhibit particle growth and aggregation. This is especially the case of surfactants that have a part that binds to the particle surface and another part with a high affinity for the solvent. So they serve as growth restrainers and colloidal stabilizers at the same time. They are widely used to control the average particle size and size distribution in chemical synthesis routes. The surfactant nature and its concentration are important parameters that have an influence in particle size. Turning back to metal organic decomposition methods, the interaction between Fe atoms and the functional group of the surfactant produces small particles when this interaction is strong. The group of Cheon made a comparative study with two surfactants, trioctylphosphine (TOPO) and dodecylamine (DDA) [97]. The alkylamine ligand used in this study seems to bind weakly to the

metal centers on the surface of nanocrystals, while the TOPO ligand forms a much stronger bond to the crystal surface due to its high oxophilicity. A weakly binding ligand can reversibly coordinate to the metal sites on the surface, and further growth is possible when sufficient amounts of alkylamine ligand are available. The Fe-surfactant interaction determines the decomposition temperature and the number of nucleus. The molar ratio surfactant/precursor is also important, the size increases as the quantity of surfactant increases, as it was shown in a study of Yu et al. [98]. They have reported that when the ratio moves from 1:3 to 1:8 the particle size becomes 4 times greater. However, there is an upper size limit that cannot be overcome by varying the solvent temperature, the concentration of surfactants and the concentration of precursor. In order to increase the size limit Hyeon et al. proposed a variation of the method that consisted on using an iron oleate complex as the growth source. In this way, they synthesized monodisperse iron nanoparticles of 20 nm with controlled size by the additional incremental growth of the previously prepared nanoparticles, in a seed mediated process [99]. The same group has obtained nanoparticles of a diameter of 50 nm using $FeCl_3$ as iron precursor and sodium oleate [100].

1.3.2 Materials for the shell

The stabilization of the iron oxide MNPs in aqueous solutions and organic media is crucial to obtain magnetic colloidal ferrofluids that are stable against aggregation even under the presence of a magnetic field. The stability of a magnetic colloidal suspension can be controlled reaching the equilibrium between attractive and repulsive forces. Four kinds of forces can contribute to the interparticle potential in the system. Van der Waals forces induce strong short-range isotropic attractions. The electrostatic repulsive forces can be partially screened by adding a salt to the suspension. Moreover, steric repulsion forces have to be taken into account. For magnetic suspensions, magnetic dipolar forces between two particles must be added. Because of the growing interest of in the use of iron oxide nanoparticles for biomedical applications many efforts have been employed to render them stable in biological fluids. As we mentioned before, the method of precipitation from organic solutions is the most adequate to obtain samples with good size control, narrow size distribution

and high crystallinity. Making these particles hydrophilic could open the possibility of their use in biomedical applications. There are many different approaches to stabilize nanoparticles using a compound that coats the nanoparticles surface. The most usual are: (1) organic coatings such as dextran, polyethylene glycol or chitosan; (2) inorganic coatings such as gold, silica or carbon.

The coating of iron oxide nanoparticles avoids aggregation but also may affect the magnetic properties of the system due to the modification of the particle surface. In fact, a decrease of M*s* has been observed for iron oxide nanoparticles coated with certain organic or inorganic coatings [101]. Therefore, it is important to take this into account for biomedical applications.

1.3.2.1 Organic coatings

The stability of a magnetic colloidal suspension results from the equilibrium between attractive and repulsive forces. The interparticle repulsion can be electrostatic if the polarity of the solvent is high enough, steric if a suitable surfactant or polymer is used as a steric barrier, or it can be produce by the properties of solvation of the particle coating in the solvent [102]. For an organic solvent, the use of surfactants is the most common way to stabilize the dispersions. The surfactant employed must contain one or more functional groups that interact with the surface of the particle and another group, for example, a long enough hydrocarbon chain to render the coated particle stable in the solvent. The chain of the surfactant provides a permanent distance between the particles and compatibility with the solvent. The functional group, which can be cationic, anionic or non-ionic, is attached to the magnetic particle surface by chemical bonding, physical interaction or a combination of both. As we mentioned before, the high-temperature decomposition methods yield more uniform nanoparticles with better magnetic properties than aqueous routes, but for biomedical applications it is important to make them water stable.

Organic coatings are usually employed to render MNPs stable in water at neutral pH and physiological salinity [103]. The coating can be performed by different

methodologies: in situ coating, post synthesis adsorption and post synthesis grafting via covalent bonds [104]. Many examples of MNPs organic coatings have been reported in the literature; here we will mention some of the most common. Natural polymers are widely used due to their advantages: they are nontoxic, non-immunogenic and biodegradable. Dextran is a branched polysaccharide composed of glucose. At the end of the 80´s, Widder et al. coated iron oxide with dextran by mixing the polymer with MNPs obtained by coprecipitation [105]. Jung and Jacob have obtained a colloidal dispersion of dextran coated nanoparticles, called Ferumoxan that is stable over a pH range from 3 to10 [106]. Chitosan is a cationic hydrophilic natural polymer that is very popular in drug delivery applications because it is very abundant in nature and is easy to functionalize. Kim et al. have produced MNPs coated with chitosan by physically adsorption above oleic acid coated nanoparticles [107]. Poly(ethylene glycol) (PEG) is a biocompatible linear synthetic polyether. It improves the dispersibility and blood circulation time of the MNPs and it can favour the transport across the blood-brain barrier. An example of PEG coating method is that described by Kohler et al. who grafted PEG to MNPs via a silane group in toluene [108]. Polyethyleneimine (PEI) is another water soluble cationic polymer that has been used for decades for gene delivery. An in situ method for PEI coating of MNPs is given by Corti et al. [109]. However PEI coatings still present several problems including PEI´s toxicity. Pluronics are a family of poly(ethylene oxide)-b-poly(propylene oxide)-b-poly(ethyleneoxide) triblock copolymers that are often used as non-ionic surfactants in biotechnological and pharmaceutical industries due to their high surfactant capacities, low toxicity and minimal immune response. These block-copolymers have been used for the thermal synthesis of iron based MNPs [110].

Recently, several groups have achieved the encapsulation by nanoprecipitation method of oleic acid-coated magnetite nanoparticles inside spheres of polymers, or hydrogels, such as poly (D,L-caprolactone (PCL) [111], poly(lactide) acid (PLLA) [112], poly(D,L-lactide-co-glycolide) (PLGA) [113], and methoxy poly (ethylene glycol) poly (lactide) copolymer (MPEGPLA) [111]. These polymers can provide the system with additional advantages. For instance, the group of T.Y. Liu demonstrated

that beads of poly(ethylene-oxide)- poly(propylene-oxide)- poly(ethylene-oxide) block copolymers (PEO-PPO-PEO) encapsulating iron oxide nanoparticles and a drug could be magnetically triggered for drug release[114].

A group of polymers that deserve special attention concerning drugs and NPs encapsulation is that of polymer hydrogels. These hydrogels can be prepared in several ways. When synthetic polymers are used, they are typically dissolved in a convenient solvent followed by precipitation in a liquid environment leading to particle formation. The drug or nanoparticles intended to be encapsulated in the spheres are usually incorporated during the polymer solvation and precipitation processes. Solvent diffusion, solvent evaporation, nanoprecipitation and salting-out methods are widely applied techniques and they have been discussed in several reviews [115–118]. In solvent evaporation, the dissolved polymer is emulsified with an aqueous phase with the help of a high-energy source such as ultrasound or homogenization followed by solvent evaporation (vacuum and/or temperature). In the salting-out method, polymer precipitation is obtained via phase separation (organic solvent-aqueous phase) by the addition of a salting-out agent. Similarly, in solvent diffusion, nanospheres are formed when the saturation limit of a partially water-miscible solvent is exceeded by addition of water. In both techniques, the phase separation is accompanied by vigorous stirring. Techniques such as supercritical fluid technologies [119–120] are different approaches to nanoscale spheres preparation. Additionally, polymer nanospheres can be created directly from monomers by means of different polymerization techniques as presented in some reviews [115,117].

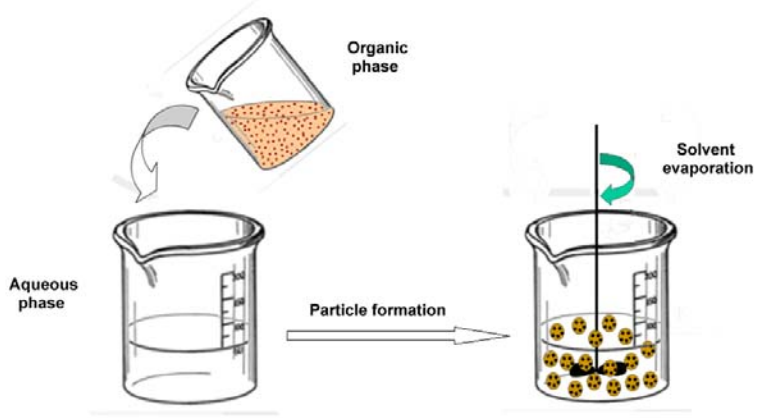

Figure 5.4 Nanoprecipitation method.

In nanoprecipitation, introduced by Fessi et al. [121], the spheres formation is based on precipitation and subsequent solidification of the polymer at the interface of a solvent and non-solvent. The polymer is dissolved in a water miscible organic solvent and then added to an aqueous solution, where the organic solvent is dispersed by stirring the mixture, as shown in Figure 5.4. Particle formation is spontaneous, because the polymer precipitates in the aqueous environment. It is currently accepted that the Marangoni effect explains the process as follows [118]: solvent flow, diffusion and surface tensions are the interface of the organic solvent and the aqueous phase cause turbulences, which form small droplets containing the polymer. Subsequently, as the solvent diffuses out from the droplets, the polymer precipitates. The emulsification step is critical because the stirring speed determine the size of the particles. Finally, the organic solvent is typically evaporated with help of vacuum or temperature. Usually, surfactants or stabilizers are included in the process to modify the size and the surface properties, or to ensure the stability of the spheres dispersion. However, the presence of surfactants is not indispensable for the formation of the particles. The drug substance or the nanoparticles to be encapsulated are, depending on its solubility, dispersed as an aqueous solution or dissolved in the organic solvent before the fusion of the phases. The nanoprecipitation technique suffers from poor encapsulation efficacy of hydrophilic drugs or nanoparticles, because they can diffuse

to the aqueous outer phase during polymer precipitation [122]. By modifying the solubility of the drug by changes in the pH, the drug can be easily encapsulated [123]. Another way to improve the encapsulation is accelerating the precipitation rate of the polymer, modifying solvent composition or increasing the M*w* of the polymer.

Alternatively, multi-functional and/or multi-responsive polymeric systems have been developed due to their potential applications. Multi-responsive core-shell nanospheres that exhibit volume changes in response to temperature and pH were synthesized by incorporating a temperature responsive polymer and a pH sensitive polymer in the core and shell structure, respectively [124]. The nanostructured polymer particles, however, have an average diameter of about 100–200 nm, which limits the hydrogels for drug and gene delivery applications. Most self-assembling polymeric micelles and polyelectrolyte complex nanoparticles have a size smaller than 100 nm, but they are unstable, tend to aggregate, or easily disintegrate in body fluid conditions because their structures are primarily maintained by weak interactions. Thus, it is desirable to synthesize robust and stable hydrogels with sizes under 200 nm that are stable in physiological conditions. They have definite advantages as carriers for drugs and imaging agents. There are several studies about diverse types of pH-responsive hydrogels. These include metacrylic latexes [125], N-isopropylacrylamide copolymer microgels containing another monomers [126], and monomers such as 4-vinylpyridine (4VP) [127], 2-vinylpyridine (2VP) [128], 2-(diethylamino)ethyl methacrylate (DEA) [129], 2- (diisopropylamino)-ethyl methacrylate (DPA) [130]. It is known that poly (vinylpyridine) is a pH dependent polymer by itself and in combination with other polymers [131, 133], but as far as it is known, no work has been carried out, up to date, on the preparation of polyvinylpyridine polymer spheres by the nanoprecipitation method.

1.3.2.2 Inorganic coatings

Inorganic coatings present some unique differences with respect to organic ones. They do not experiment swelling or porosity changes with changes in pH, ionic strength or temperature, and they are not vulnerable to microbiological attacks. Coatings such as gold, carbon and silica have been widely investigated because they can be quite adequate for biological applications due to their biocompatibility. These coatings can provide not only good dispersibility of the particles in aqueous medium, but also chemical stability and easy functionalization. A paradigmatic case, widely reported in the bibliography, is that of gold, which can be easily functionalized due to its binding abilities with thiol groups [134]. Alternatively, the advantage of carbon coatings is in its porosity that allows the adsorption of a large variety of compounds [135]. Regarding silica, a silicon dioxide with chemical formula SiO_2, it has been known since a long time for its hardness. Silica is the most abundant mineral in the Earth's crust. It is most commonly found in nature as sand or quartz, as well as in the cell walls of diatom algae. In the vast majority of silicates, the Si atom shows tetrahedral coordination, with 4 oxygen atoms surrounding a central Si atom, as it can be seen in Figure 1.8. In each of the most thermodynamically stable crystalline forms of silica, on average, all 4 of the vertices (or oxygen atoms) of the SiO_4 tetrahedra are shared with others, yielding the simplified chemical formula of SiO_2.

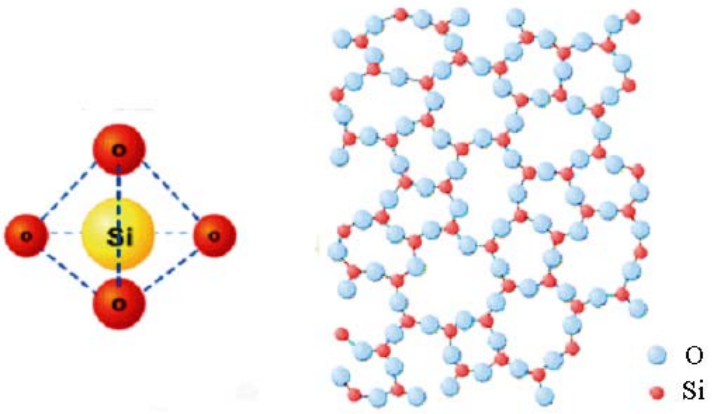

Figure 1.8 Tetrahedral structure unit of silica and amorphous structure of silica.

Silica can be obtained by a large variety of methods. The most common involves exposing silicon to oxygen. When silicon is exposed to air under ambient conditions, a very thin oxide layer is formed on the surface. In order to grow well-controlled layers of silicon dioxide, higher temperatures and alternative environments are used. However, the most interesting method to synthesize silica is that of sol-gel. This method is a wet chemical route; the sol evolves gradually towards the formation of a gel network containing both a liquid phase and a solid phase. In basic solutions, the particles may grow to sufficient size to become colloids. Then the sol evolves towards the formation of a phase gel. In the case of the colloid, the number of particles in an extremely dilute suspension may be so low that the removal of a significant amount of solvent may be needed for the gel properties to be recognized. This can be accomplished in a number of ways. The simplest method is to allow time for sedimentation to occur, or by centrifugation to separate the solid from the solvent. The removal of all the solvent requires drying. Chemically, the synthesis of SiO_2 involves hydrolysis and condensation of a precursor, such as tetraethyl orthosilicate (TEOS), in an appropriate solvent, such as ethanol or water, with or without the use of a catalyst.

$$SiOEt)_4 + H_2O + OH^- \rightarrow (OEt)_3Si(OH) + ROH$$

$$(OEt)_3Si(OH) + H_2O \rightarrow SiO_2 + 3EtOH$$

As these reactions proceed, a network of Si-O-Si bonds is formed and the viscosity of the solution increases due to the gel formation. Finally, the gel condenses and the particles precipitate. Many efforts have been dedicated to obtain silica coated MNPs using this approach. The group of Philipse has prepared them by precipitation of sodium silicate followed by hydrolysis of tetraethylorthosilicate (TEOS) in basic conditions [136].

Another strategy to obtain well coated nanoparticles is microemulsion. Yang et al. achieved this and went a bit farther by entrapping biological molecules inside the porous of the silica shell [137]. Aerosol methods also provide good results in magnetic nanoparticle silica encapsulation, as Tartaj et al. have demonstrated [138]. Yi et al.

prepared a soluble hybrid material consisting of MNPs and silica by a modified Stöber method [139]. The Stöber method for the preparation of monodisperse spherical silica particles, see Figure 1.9, in basic solution was published in 1968 [140].

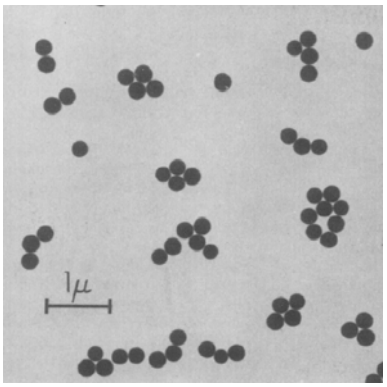

Figure 1.9 TEM micrograph of silica particles obtained by the Stöber method.

The use of silica as a coating permits also the tuning of the magnetic properties of the MNPs [141]. Besides, another advantage of silica is the presence of the silanol groups on the surface that can easily react with a wide variety of ligands carrying a diversity of functionalities. In this way, enzymes, proteins and other molecules that are useful for different biomedical applications can be anchor to the particle surface. Furthermore, besides surface functionalization, this material can be produced with a mesoporous structure, i.e. MCM-41 or SBA-15, with a pore size large enough to house MNPs and/or biological molecules [142]. These materials are amorphous but show a hexagonal arrangement of pores with a size that can be varied by adjusting the synthesis parameters. The group of Yang has used materials of this kind, SBA-15, to transport drugs such as ibuprofen [143].

Even though silica offers many potential advantages as a coating of MNPs, it also represents a controversial issue concerning the use of silica in biomedical applications with regard to toxicity. Some studies have found negative toxic effects of silica in living organisms; they have proven that silica nanoparticles cause lung fibrosis in rats, and toxic effects and alterations in the protein expression in HaCaT cells [144, 145].

However, others contrast these findings, for example, a study on this subject has been presented by Rondeau et al. [146], they concluded that it is indigestible, without nutritional value, but no toxic. When silica is ingested orally, it passes unchanged through the gastrointestinal tract, leaving no trace behind. Actually, a study on volunteer persons over 15 years showed that high levels of silica in water appeared to decrease the risk of dementia. This study found that with an increase of 10 milligram per day of the intake of silica in drinking water, the risk of dementia dropped by 11%.

1.4 Purpose of the thesis and goals

The work presented in this thesis can be classified in three main areas: (1) monodisperse ferrofluids for biomedical applications; (2) superparamagnetic beads for a biosensor; and (3) MNPs encapsulated in a polymer for drug delivery. All of them share the same fundamental perspective, which is to control the synthesis and properties of functionalized nanoparticles based on their magnetic properties. Each area of research is summarized in the following sections and a detailed discussion is presented in the following chapters.

1.4.1 Ferrofluids for biomedical applications

Our main objective in this area was to obtain aqueous dispersions of high quality iron oxide nanoparticles with a coating that could be easily functionalised and used in biomedical applications. Therefore, the nanoparticles were produced in organic solvents by thermal decomposition of organometallic precursors. Then these nanoparticles were transferred to aqueous medium. Finally, they were coated with a silica shell. For this purpose, we have followed a ligand exchange technique that consists on the substitution of the hydrophobic ligand used in the organic synthesis by a hydrophilic ligand. The exchange ligand was a compound consisting on a hydrocarbon chain having a silica precursor at one end and a group with a strong affinity for the surface of iron oxide particle, namely an iron coordination group. The silica precursor group was always triethoxysilane. Several iron coordination groups have been comparatively studied in this work: imidazole, phosphate and carboxylate.

The length of the hydrocarbon chain has been also systematically varied. Stable aqueous dispersions have been obtained with both short and long chain lengths. For short chain length, the best performance was obtained with N-(3-triethoxysilylpropyl)-4,5-dihydroimidazole and its imidazole iron coordination groups. Finally, in order to improve the biocompatibility of the nanoparticles, some of the samples were successfully covered with polyethylenglicol by reacting the silica coated nanoparticles with a PEG-alkoxysilane derivative.

1.4.2 Superparamagnetic beads for a biosensor

A second thrust of research in this dissertation involves the contribution to the development of a biosensor based on the changes in the impedance produced by iron oxide nanoparticles encapsulated in silica spheres when they interact with the capacitor plates. As we mentioned before, iron oxide nanoparticles obtained by the thermal decomposition method have better qualities than those obtained in aqueous media, but depending on the application for what they are desired it can be better to use the nanoparticles synthesized in aqueous media. After careful consideration and focusing on the final application, we synthesized MNPs by an aqueous method and subsequently we encapsulated them in silica spheres by a modified Stöber method. Afterwards, the nanospheres were functionalized with a siloxane that ends in a carboxylic group. Then, the spheres were attached to the capacitor plate surface by the sandwich technique [147]. In parallel, a plate was coated with a capture antibody, the same antibody that we have used to functionalize the nanosphere and was bonded by the carboxylic group. Then, an antigen was added to the suspension of nanospheres that binds to the antibody. The interaction of the system with the capacitor plates was investigated by means of an Enzyme-Linked Immuno Sorbent Assay (ELISA). In addition, the measurement of the impedance of the capacitor before and after the treatment has permitted us to determine the sensibility of this biosensor.

1.4.3 MNPs encapsulated in a polymer for drug delivery

The main objective is to design a multifunctional system able to combine the properties that will make it suitable to be used for therapy and diagnostics. We have developed in this work a multi-responsive system and it consists on a pH-responsive polymer that form microspheres with encapsulated MNPs that allows the magnetic core to enable externally controlled actuation under magnetic induction. Magnetic measurements have shown that the iron oxide nanoparticles are superparamagnetic and therefore are able to undergo a local increase of the temperature when an oscillating magnetic field is applied. Poly(4-vinylpyridine) is a pH-responsive material that can provide new opportunities for the organic-inorganic system and it is a widely studied polymer in our group. The synthesis of PVP polymer spheres is conducted without help of crosslinking or monomer polymerization but using a very simple modified nanoprecipitation process. Afterwards, magnetic polymer spheres P4VP-PEG were obtained by means of nanoprecipitation technique, in order to improve their stability in biological fluids, increase the blood circulation time and can be conveniently functionalized for targeting. The system with magnetically triggered heating and pH sensitivity can be potentially useful with some modifications for biomedical applications like separation, purification, MRI, targeted drug delivery and biosensors.

1.5 Bibliography

[1] O. Kreft, M. Prevot, H. Mohwald and G. B. Sukhorukov. Shell-in-shell microcapsules: A novel tool for integrated, spatially confined enzymatic reactions. *Angewandte Chemie-International Edition*, 46:5605–5608, 2007.

[2] I. Safarik and M. Safarikova, Magnetic nano- and microparticles in biotechnology. *Chemical Papers,* 63:497–505, 2009.

[3] K. S. Lee, M. H. Woo, H. S. Kim, E. Y. Lee and I. S. Lee, Synthesis of hybrid Fe3O4-silica-nio superstructures and their application as magnetically separable high-performance biocatalysts, *Chem. Commun.*, 25:3780–3782, 2009.

[4] J. J. Lai, K. E. Nelson, M. A. Nash, A. S. Hoffman, P. Yager and P. S. Stayton, Dynamic bioprocessing and microfluidic transport control with smart magnetic nanoparticles in laminar-flow devices. *Lab on a Chip* 9:1997–2002, 2009.

[5] D. S. Wang, J. B. He, N. Rosenzweig, Z. Rosenzweig, Superparamagnetic Fe_2O_3 beads-CdSe/ZnsS quantum dots core-shell nanocomposite particles for cell separation. *Nano Letters,* 4:409–413, 2004.

[6] D. Pouliquen, R. Perdrisot, A. Ermias, S. Akoka, P. Jallet and J. J. Lejeune. Superparamagnetic iron-oxide nanoparticles as a liver MRI contrast agent-contribution of microencapsulation to improved biodistribution. *Magnetic Resonance Imaging,* 7:619–627, 1989.

[7] Widder DJ, Greif WL, Widder KJ, Edelman RR and Brady TJ. Magnetite albuminum microspheres: A new MR contrast material. *American Journal of Roentgenology,* 148: 399–404, 1987.

[8] Weissleder R, Elizondo G, Wittenberg J, Rabito CA, Bengele HH, Josephson L, Ultrasmall superparamagnetic iron oxide: characterization of a new class of contrast agents for MR imaging. Radiology, 175:489–493, 1990.

[9] C. R. Tamanaha, S. P. Mulvaney, J. C. Rife and L. J. Whitman. Magnetic labeling, detection, and system integration. *Biosensors and Bioelectronic,s* 24:1–13, 2008.

[10] J. B. Haun, T. J. Yoon, H. Lee and R. Weissleder, Magnetic nanoparticle biosensors Wiley interdisciplinary reviews- Nanomedicine and nanobiotechnology, 2:291–304, 2010.

[11] T. T. Baby and S. Ramaprabhu. SiO_2 coated Fe_3O_4 magnetic nanoparticle dispersed multi-walled carbon nanotubes based amperometric glucose biosensor. *Talanta* 80:2016–2022, 2010.

[12] A. Jordan, R. Scholz, K. Maier-Hauff, M. Johannsen, P. Wust, J. Nadobny, H. Schirra, H. Schmidt, S. Deger, S. Loening, W. Lanksch and R. Felix. Presentation of a new magnetic field therapy system for the treatment of human solid tumors with magnetic fluid hyperthermia. *Journal of Magnetism and Magnetic Materials*, 225:118–126, 2001.

[13] M. Babincova, D. Leszczynska, P. Sourivong and P. Babinec. Selective treatment of neoplastic cells using ferritin-mediated electromagnetic hyperthermia. *Medical Hypotheses,* 54:177–179, 2000.

[14] C. Alexiou, W. Arnold, R. J. Klein, F. G. Parak, P. Hulin, C. Bergemann, W. Erhardt, S. Wagenpfeil and A. S. Lubbe. Locoregional cancer treatment with magnetic drug targeting. *Cancer Research*, 60:6641–6648, 2000.

[15] V. Ozdemir, B. Williams-Jones, S. J. Glatt, M. T. Tsuang, J. B. Lohr and C. Reist. Shifting emphasis from pharmacogenomics to theragnostics. Nature Biotechnology 24:942–947, 2006.

[16] A. Millán, F. Palacio, E. Snoeck, V. Serin and P. Lecante. *Polymer Nanocomposites.* Ed. Yiu-Wing Mai and Zhong-Zhen Yu, Woodhead Publishing Ltd, Cambridge, 2006.

[17] O. Veiseh, J. W. Gunn and M. Q. Zhang. Design and fabrication of magnetic nanoparticles for targeted drug delivery and imaging. Advanced Drug Delivery Reviews 62:284–304, 2010.

[18] A. Bjornerud and L. Johansson. The utility of superparamagnetic contrast agents in MRI: theoretical consideration and applications in the cardiovascular system. NMR in Biomedicine 17:465–477, 2004.

[19] Y. Zhang, N. Kohler and M. Q. Zhang. Surface modification of superparamagnetic magnetite nanoparticles and their intracellular uptake. *Biomaterials*, 23:1553–1561, 2002.

[20] E. Taboada, R. Solanas, E. Rodriguez, et al. Supercritical-Fluid-Assisted one-pot synthesis of biocompatible core(γ-Fe_2O_3)/shell(SiO_2) nanoparticles as high relaxivity T-2-contrast agents for magnetic resonance imaging. *Advanced Functional Materials,* 19:2319–2324, 2009**.**

[21] W. Schutt, C. Gruttner, U. Hafeli, M. Zborowski, J. Teller, H. Putzar and C. Schumichen, Applications of magnetic targeting in diagnosis and therapy - Possibilities and limitations: A mini-review. *Hybridoma,* 16:109–117, 1997.

[22] C. S. Brazel. Magnetothermally-responsive nanomaterials: Combining magnetic nanostructures and thermally-sensitive polymers for triggered drug release. *Pharmaceutical Research*, 26:644–656, 2008.

[23] A. Jordan, P. Wust, H. Fahling, W. John, A. Hinz and R. Felix. Inductive heating of ferrimagnetic particles and magnetic fluids - physical evaluation of their potential for hyperthermia. *International Journal of Hyperthermia*, 9:51–68, 1993.

[24] I. Tohnai, Y. Goto, Y. Hayashi, M. Ueda, T. Kobayashi and M. Matsui. Preoperative thermochemotherapy of oral cancer using magnetic induction hyperthermia (implant heating system: IHS). *International Journal of Hyperthermia*, 12:37–47, 1996.

[25] I. Hilger, W. Andra, R. Bahring, R. Hergt and W. A. Kaiser. Hyperthermic treatment of tumour tissue using iron(II,III)-oxide. *Biomed. Tech.*, 42:383–384, 1997.

[26] M. Yanase, M. Shinkai, H. Honda, T. Wakabayashi, J. Yoshida, T. Kobayashi. Antitumor immunity induction by intracellular hyperthermia using magnetite cationic liposomes. *Japanese Journal of Cancer Research*, 89:775–782, 1998.

[27] H. H. Kampinga and E. Dikomey. Hyperthermic radiosensitization: mode of action and clinical relevance. *International Journal of Radiation Biology,* 77:399–408, 2001.

[28] R. Rosensweig. Heating magnetic fluid with alternating magnetic field. *Journal of Magnetism and Magnetic Materials*, 252:370–374, 2002.

[29] R. Hergt and W. Andrä. *Magnetism in medicine*. Wiley-VCH: Weinheim 550–570, 2007.

[30] S. J. Han and S. Wang, Magnetic Nanotechnology for Biodetection. *JALA***,** 15:93–98, 2010.

[31] J. Wang, Y. Sun, L. Wang, X. Zhu, H. Zhang and D. Song, Surface plasmon resonance biosensor based on Fe_3O_4/Au nanocomposites. *Colloids and Surfaces B: Biointerfaces*, 81:600–606, 2010.

[32] O. Veiseh, J. W. Gunn and M. Zhang. Design and fabrication of magnetic nanoparticles for targeted drug delivery and imaging. Advanced Drug Delivery Reviews, 62:284–304, 2010.

[33] K. Widder, A. E. Senyei and D. G. Scarpelli. Magnetic microspheres – Model system for site specific drug delivery in-vivo. Proccedings of the society for experimental biology and medicine, 158:141–146, 1978.

[34] A. Senyei, K. Widder and G. Czerlinski. Magnetic guidance of drug-carrying microspheres. *J. Appl. Phys.*, 49:3578–3583, 1978.

[35] J. Kim, J. E. Lee, S. H. Lee, J. H. Yu, J. H. Lee, T. G. Park and T. Hyeon. Designed fabrication of a multifunctional polymer nanomedical platform for simultaneous cancer-targeted imaging and magnetically guided drug delivery. *Advanced Materials,* 20:478–483, 2008.

[36] Y. H. Deng, C. C. Wang, J. H. Hu, W. L. Yang and S. K. Fu. Investigation of formation of silica-coated magnetite nanoparticles via sol-gel approach. *Colloids and Surfaces A: Physicochemical and Engineering Aspects*, 262:87–93, 2005.

[37] D. X. Li, Q. He, Y. Yang, H. Mohwald and J. Li. Two-stage pH response of poly(4-vinylpyridine) grafted gold nanoparticles. *Macromolecules,* 41:7254-7256, 2008.

[38] R. I. Mahato. Water insoluble and soluble lipids for gene delivery. Advanced *Drug Delivery Reviews*, 57:699–712, 2005.

[39] A. Lubbe, C. Bergemann, H. Riess, et al. Clinical experiences with magnetic drug targeting: A phase i study with 4'-epidoxorubicin in 14 patients with advanced solid tumours*. Cancer Research* 56:4686–4693, 1978.

[40] J. Wang K. Matyjaszewski. Atom Transfer Radical Polymerization. *Chem. Rev.*, 101:2921–2990, 2001.

[41] S. Bhaskar, F. R. Tian, T. Stoeger, W. Kreyling, J. M. de la Fuente, V. Grazu, P. Borm, G. Estrada, V. Ntziachristos and D. Razansky. Multifunctional nanocarriers for diagnostics, drug delivery and targeted treatment across blood-brain barrier: perspectives on tracking and neuroimaging. *Particle and Fibre Toxicology*, 7:3, 2010.

[42] W. M. Pardridge. Drug targeting to the brain. *Pharmaceutical Research*, 24:1733–1744, 2007.

[43] F. J. Lazaro, A. R. Abadia, M. S. Romero, L. Gutierrez, J. Lazaro and M. P. Morales. Magnetic characterisation of rat muscle tissues after subcutaneous iron dextran injection. *Biochimica et Biophysica Acta-Molecular Basis of Disease*, 1740:434–445, 2004.

[44] A. H. Morrish. *The physical principles of magnetism*. John Wiley, 1965.

[45] O. Iglesias and A. Labarta. Finite-size and surface effects in maghemite nanoparticles: Monte Carlo simulations. *Physical Review B*, 63:184416, 2001.

[46] A. P. Ramirez. Colossal magnetoresistance. *Journal of Physics- Condensed Matter*, 9:8171–8199, 1997.

[47] R. H. Kodama. Magnetic nanoparticles. *Journal of Magnetism and Magnetic Materials*, 200:359–372, 1999.

[48] R. H. Kodama, S. A. Makhlouf and A. E. Berkowitz. Finite size effects in antiferromagnetic nio nanoparticles. Physical Review Letters ,79:1393–1396, 1997.

[49] L. Neel and C. R. Hedb. Anomalous magnetic nanostructural evolution in annealed CuCo granular thin films. *C. R. Hebd. Seances Acad. Sci.*, 228:664, 1949.

[50] W. F. Brown, Thermal fluctuations of a single-domain particle, *Physical Review*, 130:1677–1686, 1963.

[51] O. S. Selawry, M. N. Goldstein and T. McCormick. Hyperthermia in tissuecultured cells of malignant origin. Cancer Research 17:785–791, 1957.

[52] F. Gazeau, M. Levy and C. Wilhelm. Optimizing magnetic nanoparticle design for nanothermotherapy. *Nanomedicine,* 3:831–844, 2008.

[53] H. Kachkachi, A. Ezzir, M. Nogues and E. Tronc. Surface effects in nanoparticles : application to maghemite γ-Fe_2O_3. *Eur. Phys. J. B*, 14 :681–689, 2000.

[54] A. Millan, A. Urtizberea, N. Silva, F. Palacio, V. Amaral, E. Snoeck and V. Serin. Surface effects in maghemite nanoparticles. *Journal of Magnetism and Magnetic Materials*, 312:5–9, 2007.

[55] R. H. Kodama, A. E. Berkowitz, E. J. McNiff and S. Forner. Surface spin disorder in $NiFe_2O_4$ nanoparticles. *Physical Review Letters*, 77:394–397, 1996.

[56] R. H. Kodama, A. E. Berkowitz, E. J. McNiff and S. Foner. Surface spin disorder in ferrite nanoparticles. *Journal of Applied Physics*, 81:5552–5557, 1997.

[57] M. Respaud, J. M. Broto, H. Rakoto, A. R. Fert, L. Thomas, B. Barbara, M. Verelst, E. Snoeck, P. Lecante, A. Mosset, J. Osuna, T. O. Ely, C. Amiens and B. Chaudret. Surface effects on the magnetic properties of ultrafine cobalt particles. *Physical Review B*, 57 :2925–2935, 1998.

[58] R. J. Pollard, C. M. Cardile, D. G. Lewis, L. J. Brown, Characterization of FeOOH polymorphs and ferrihydrite using low-temperature, applied- field, Mossbauer-spectroscopy, Clay Minerals 27 (1) (1992) 57–71.

[59] J. M. D. Coey, and P. W. Readman. New spin structure in an amorphous ferric gel. Nature, 246:476–478, 1973.

[60] S. Koutani, G. Gavoille and R. Gerardin. Magnetic-behaviour of aggregates of small γ-Fe_2O_3 particles. *Journal of Magnetism and Magnetic Materials,* 123:175–183, 1993.

[61] S. Morup, and E. Tronc. Superparamagnetic relaxation of weakly interacting particles. Physical Review Letters, 72:3278–3281, 1994.

[62] R.M. Cornell, U. Schwertmann, *The iron oxides*. Wiley-VCH, 2003.

[63] M. F. Casula, P. Floris, C. Innocenti, A. Lascialfari, M. Marinone, M. Corti, R. A. Sperling, W. J. Parak and C. Sangregorio. Magnetic resonance imaging contrast agents based on iron oxide superparamagnetic ferroflufluids. *Chemistry of Materials*, 22:1739–1748, 2010.

[64] C.L. Tseng, I. L. Shih, L. Stobinski and F.H. Lin. Gadolinium hexanedione nanoparticles for stem cell labeling and tracking via magnetic resonance imaging. Biomaterials, 31:5427–35, 2010.

[65] M. Jeun, S. J. Moon, H. Kobayashi, H. Y. Shin, A. Tomitaka, Y. J. Kim, Y. Takemura, S. H. Paek, K. H. Park, K. W. Chung and S. Bae. Effects of Mn concentration on the ac magnetically induced heating characteristics of superparamagnetic $Mn_xZn_{1-x}Fe_2O_4$ nanoparticles for hyperthermia. *Applied Physics Letters*, 96:202511, 2010.

[66] K. L. McNerny, Y. Kim, D. E. Laughlin and M. E. McHenry. Chemical synthesis of monodisperse gamma-Fe-Ni magnetic nanoparticles with tunable Curie temperatures for self-regulated hyperthermia. Journal of Applied Physics, 107:312–313, 2010.

[67] K. B. Lee, S. Park and C. A. Mirkin. Multicomponent magnetic nanorods for biomolecular separations. Angewandte Chemie-International Edition, 43:3048–3050, 2004.

[68] H. W. Gu, P. L. Ho, K. W. T. Tsang, L.Wang and B. Xu. Using biofunctional magnetic nanoparticles to capture vancomycin-resistant enterococci and other gram-positive bacteria at ultralow concentration. Journal of the American Chemical Society, 125:15702–15703, 2003.

[69] B. D. Cullity. *Introduction to magnetic materials*. Wiley, CA, USA, 2009.

[70] K. J. Gallagher, W. Feitkchnet and U. Mannweiler. Mechanism of oxidation of magnetite to maghemite. *Nature*, 217:118–1121, 1968.

[71] G. F. Goya. Handling the particle size and distribution of Fe_3O_4 nanoparticles through ball milling. *Solid State Communications*, 130:783–787, 2004.

[72] T. Sugimoto. *Fine particle: synthesis, characterization and mechanism of growth*. Marcel Dekker, New York, 2000.

[73] A. Gutsch, H. Muhlenweg and M. Kramer. Tailor-made nanoparticles via gas-phase synthesis. *Small* 1:30–46, 2005.

[74] Y. I. Kim, D. Kim and C. S. Lee. Synthesis and characterization of $CoFe_2O_4$ magnetic nanoparticles prepared by temperature-controlled coprecipitation method. *Physica B-Condensed Matter*, 337:42–51, 2003.

[75] F. Bensebaa, F. Zavaliche, P. L'Ecuyer, R. W. Cochrane and T. Veres. Microwave-synthesis and characterization of Co-ferrite nanoparticles. *Journal of Colloid and Interface Science*, 277:104–110, 2004.

[76] C. R. Vestal and Z. J. Zhang. Magnetic spinel ferrite nanoparticles from microemulsions. *International Journal of Nanotechnology*, 1:240–263, 2004.

[77] J. G. Lee, J. Y. Park and C. S. Kim. Growth of ultra-fine cobalt ferrite particles by a sol-gel method and their magnetic properties. *Journal of Materials Science*, 33 :3965–3968, 1998.

[78] G. B. Ji, S. L. Tang, S. K. Ren, F. M. Zhang, B. X. Gu and Y. W. Du. Simplified synthesis of single-crystalline magnetic $CoFe_2O_4$ nanorods by a surfactant-assisted hydrothermal process. *Journal of Crystal Growth*, 270:156–161, 2004.

[79] S. H. Sun and H. Zeng. Size-controlled synthesis of magnetite nanoparticies. *Journal of the American Chemical Society*, 124:8204–8205, 2002.

[80] K. S. Suslick, M. M. Fang and T. Hyeon. Sonochemical synthesis of iron colloids. *Journal of the American Chemical Society*, 118:11960–11961, 1996.

[81] T. Gonzalezcarreno, M. P. Morales, M. Gracia and C. J. Serna. Preparation of uniform γ-Fe_2O_3 particles with nanometer-size by spray-pyrolysis. *Materials Letters,* 18:151–155, 1993.

[82] J. Wan, W. Cai, X. Meng and E. Liu. Monodisperse water-soluble magnetite nanoparticles prepared by polyol process for high-performance magnetic resonance imaging. Chemical Communications, 47:5004–5006, 2007.

[83] T. Hyeon. Chemical synthesis of magnetic nanoparticles. Chemical Communications, 8:927–934, 2002.

[84] C. Cannas, G. Concas, D. Gatteschi et al. How to tailor maghemite particle size in γ-Fe_2O_3-SiO_2 nanocomposites. *Journal of Materials Chemistry*, 12:3141–3146, 2002.

[85] G. Ennas,A. Musinu, G. Piccaluga G et al. Characterization of iron oxide nanoparticles in an Fe_2O_3-SiO_2 composite prepared by a sol-gel method. Chemistry of Materials, 10:495–502, 1998.

[86] M. Moffitt, L. McMahon, V. Pessel and A. Eisenberg, Size Control of Nanoparticles in Semiconductor-Polymer Composites. 2. Control via Sizes of Spherical Ionic Microdomains in Styrene-Based Diblock Ionomers, Chem. Muter. 1995, 7, 1185–1192

[87] B. He, Y. Ha, H. Liu, K. Wang, K. Y. Liew, Size control synthesis of polymer-stabilized water-soluble latinum oxide nanoparticles, Journal of Colloid and Interface Science 308 (2007) 105–111

[88] H. Amiri, R. Bustamante, A. Millán, N. J. Silva, R. Piñol, L. Gabilondo, F. Palacio, P. Arosio, M. Corti and A. Lascialfari. Magnetic and relaxation properties of multifunctional polymer-based nanostructured bioferrofluids as MRI contrast agents. *Mag. Reson. Med*., 66:1715–1721, 2011.

[89] A. B. Smetana, J. S. Wang, J. Boeckl, G. J. Brown and C. M. Wai. Fine-Tuning Size of Gold Nanoparticles by Cooling during Reverse Micelle Synthesis. *Langmuir*, 23:10429–10432, 2007.

[90] M. D. Shultz, W. Braxton, C. Taylor and E. E. Carpenter. One parameter control of the size of iron oxide nanoparticles synthesized in reverse micelles. *Journal of Applied Physics*, 105:07A522**,** 2009.

[91] H. Noritomi, N. Igari, K. Kagitani, Y. Umezawa, Y. Muratsubaki and S. Kato. Synthesis and size control of silver nanoparticles using reverse micelles of sucrose fatty acid esters. *Colloid and Polymer Science*, 288:887–891, 2010.

[92] R. Massart. Preparation of aqueous magnetic liquids in alkaline and acidic media. *Ieee Transactions on Magnetics*, 17 (2) 1247–1248.

[93] K. Park, H. Koerner and R. A. Vaia. Depletion-induced shape and size selection of gold nanoparticles. *Nano Letters*, 10:1433–1439, 2010.

[94] R. Massart, E. Dubois, V. Cabuil and E. Hasmonay. Preparation and properties of monodisperse magnetic fluids. Journal *of Magnetism and Magnetic Materials*, 149:1–5, 1995.

[95] T. Rheinlander, R. Kotitz, W. Weitschies and W. Semmler. Different methods for the fractionation of magnetic fluids. *Colloid and Polymer Science*, 278:259–263, 2000.

[96] T. Rheinlander, R. Kotitz, W. Weitschies and W. Semmler. Magnetic fractionation of magnetic fluids. Journal *of Magnetism and Magnetic Materials*, 219:219–228, 2000.

[97] J. W. Cheon, N. J. Kang, S. M. Lee, J. H. Lee, J. H. Yoon and S. J. Oh. Shape evolution of single-crystalline iron oxide nanocrystals. *Journal of the American Chemical Society*, 126:1950–1951, 2004.

[98] W. W. Yu, J. C. Falkner, C. T. Yavuz and V. L. Colvin. Synthesis of monodisperse iron oxide nanocrystals by thermal decomposition of iron carboxylate salts. *Chemical Communications*, 20:2306–2307, 2004.

[99] J. Park, E. Lee, N. M. Hwang, M. S. Kang, S. C. Kim, Y. Hwang, J. G. Park, H. J. Noh, J. Y. Kini, J. H. Park and T. Hyeon. One-nanometer-scale size-controlled synthesis of monodisperse magnetic iron oxide nanoparticles. *Angewandte Chemie-International Edition*, 44:2872–2877, 2005.

[100] J. Park, K. J. An, Y. S. Hwang, J. G. Park, H. J. Noh, J. Y. Kim, J. H. Park, N. M. Hwang and T. Hyeon. Ultra-large-scale syntheses of monodisperse nanocrystals. *Nature Materials*, 3:891–895, 2004.

[101] A. K. Gupta and M. Gupta. Synthesis and surface engineering of iron oxide nanoparticles for biomedical applications. *Biomaterials*, 26:3995–4021, 2005.

[102] R. J. Hunter. *Foundations of colloid science* Vol. 1. Clarendon, Oxford, UK, 1987.

[103] S. Mornet, S. Vasseur, F. Grasset and E. Duguet. Magnetic nanoparticle design for medical diagnosis and therapy. *Journal of Materials Chemistry*, 14:2161–2175, 2004.

[104] S. Laurent, D. Forge, M. Port, A. Roch, C. Robic, L. V. Elst and R. N. Muller. Magnetic iron oxide nanoparticles: Synthesis, stabilization, vectorization, physicochemical characterizations, and biological applications. *Chemical Reviews*, 108:2064–2110, 2008.

[105] R. S. Molday and D. Mackenzie. Immunospecific ferromagnetic iron-dextran reagents or the labeling and magnetic separation of cells. *Journal of Immunological Methods*, 52:353–367, 1982.

[106] C. W. Jung and P. Jacobs. Physical and chemical-properties of superparamagnetic iron-oxide MR contrast agents - Ferumoxides, Ferumoxtran, Ferumoxsil. Magnetic Resonance Imaging, 13:661–674, 1995.

[107] E. H. Kim, H. S. Lee, B. K. Kwak and B. K. Kim. Synthesis of ferrofluid with magnetic nanoparticles by sonochemical method forMRI contrast agent. *Journal of Magnetism and Magnetic Materials*, 289:328–330, 2005.

[108] N. Kohler, G. E. Fryxell and M. Q. Zhang. A bifunctional poly(ethyleneglycol) silane immobilized on metallic oxide-based nanoparticles for conjugation with cell targeting agents. *Journal of the American Chemical Society*, 126:7206–7211, 2004.

[109] M. Corti, A. Lascialfari, M. Marinone, A. Masotti, E. Micotti, F. Orsini, G. Ortaggi, G. Poletti, C. Innocenti and C. Sangregorio. Magnetic and relaxometric properties of polyethylenimine-coated superparamagnetic MRI contrast agents. Journal of Magnetism and Magnetic Materials, 320:E316–E319, 2008.

[110] J. R. Lai, K. Shaff, A. Ulman, K. Loos, N. L. Yang, M. H. Cui, T. Vogt, S. Estournes and D. C. Locke. Mixed iron-manganese oxide nanoparticles. *Journal of Physical Chemistry B*, 108:14876–14883, 2004.

[111] M. Hamoudeh and H. Fessi. Preparation, characterization and surface study of poly-epsilon caprolactone magnetic microparticles. *Journal of Colloid and Interface Science*, 300:584–590, 2006.

[112] M. Hamoudeh and H. Fessi. Elaboration of PLLA-based superparamagnetic nanoparticles: Characterization, magnetic behaviour study and in vitro relaxivity evaluation. *International Journal of Pharmaceutics*, 338:248–257, 2007.

[113] L. N. Okassa, H. Marchais, L. Douziech-Eyrolles, K. Herve, S. Cohen-Jonathan, E. Munnier, M. Soucé, C. Linassier, P. Dubois and I. Choupra. Optimization of iron oxide nanoparticles encapsulation within poly(D,L-lactide-co-glycolide) submicron particles. *European Journal of Pharmaceutics and Biopharmaceutics*, 67:31–38, 2007.

[114] T. Y. Liu, S. H. Hu, K. H. Liu, R. S. Shaiu, D. M. Liu and S. Y. Chen. Instantaneous drug delivery of magnetic/thermally sensitive nanospheres by a high-frequency magnetic field. *Langmuir*, 24:13306–13311, 2008.

[115] C. Pinto Reis, R. J. Neufeld, A. J. Ribeiro and F. Veiga. Nanoencapsulation I. Methods for preparation of drug-loaded polymeric nanoparticles. *Nanomedicine*, 2:8–21, 2006.

[116] M. L. Hans and A. M. Lowman. Biodegradable nanoparticles for drug delivery and targeting. *Current Opinion in Solid State and Materials Science*, 6:319–327, 2002.

[117] K. S. Soppimath, T. M. Aminabhavi, A. R. Kulkarni and W. E. Rudzinski. Biodegradable polymeric nanoparticles as drug delivery devices. J. Control Release, 70:1–20, 2001.

[118] D. Quintanar-Guerrero, E. Allemann, H. Fessi and E. Doelker. Preparation techniques and mechanisms of formation of biodegradable nanoparticles from preformed polymers. *Drug Development and Industrial Pharmacy*, 24:1113–1128, 1998.

[119] D. J. Jarmer, C. S. Lengsfeld and T. W. Randolph. Manipulation of particle size distribution of poly(L-lactic acid) nanoparticles with a jet-swirl nozzle during precipitation with a compressed antisolvent. Journal of Supercritical Fluids, 27:317–336, 2003.

[120] S. Salmaso, N. Elvassore, A. Bertucco, A. Lante and P. Caliceti. Nisin-loaded poly-L-lactide nano-particles produced by CO_2 anti-solvent precipitation for sustained antimicrobial activity. *International Journal of Pharmaceutics,* 287:163–173, 2004.

[121] H. Fessi, F. Puisieux, J. P. Devissaguet, N. Ammoury and S. Benita. Nanocapsule formation by interfacial polymer deposition following solvent displacement. *International Journal of Pharmaceutics*, 55:R1–R4, 1989.

[122] J. M. Barichello, M. Morishita, K. Takayama and T. Nagai. Encapsulation of hydrophilic and lipophilic drugs in PLGA nanoparticles by the nanoprecipitation method. Drug Development and Industrial Pharmacy, 25:471–476, 1999.

[123] T. Govender, S. Stolnik, M. C. Garnett, L. Illum, S. S. Davis, PLGA nanoparticles prepared by nanoprecipitation: drug loading and release studies of a water soluble drug. *Journal of Controlled Release* 57:171–185, 1999.

[124] D. Kuckling, C. D. Vo, S. E. Wohlrab, Preparation of nanogels with temperature-responsive core and pH-responsive arms by photo-crosslinking, Langmuir 18 (11) 4263–4269, 2002.

[125] B. R. Saunders, H. M. Crowther, and B. Vincent. Poly[(methyl methacrylate)-co-(methacrylic acid)] microgel particles: swelling control using pH, cononsolvency, and osmotic deswelling. *Macromolecules* 30:482, 1997.

[126] M. Bradley, J. Ramos and B. Vincent. Equilibrium and kinetic aspects of the uptake of poly(ethylene oxide) by copolymer microgel particles of Nisopropylacrylamide and acrylic acid. *Langmuir,* 21:1209–1215, 2005.

[127] G. H. Ma and T. Fukutomi. Preparation and chemical fixation of poly(4-vinylpyridine) microgel film with ordered structure. *Macromolecules*, 25:1870–1875, 1992.

[128] A. Loxley and B. Vincent. Equilibrium and kinetic aspects of the pH-dependent swelling of poly(2-vinylpyridine-co-styrene) microgels. *Colloid. Polym. Sci*., 275:1108–1114, 2006.

[129] J. I. Amalvy, E. J. Wanless, Y. Li, V. Michailidou and S. P. Armes. Synthesis and characterization of novel pH-responsive microgels based on tertiary amine methacrylates. *Langmuir,* 20:8992–8999, 2004.

[130] H. Hayashi, M. Iijima, K. Kataoka and Y. Nagasaki. pH-sensitive nanogel possessing reactive PEG tethered chains on the surface. *Macromolecules,* 37:5389–5396, 2004.

[131] D. X. Li, Q. He, Y. Yang, H. Mohwald and J. Li. Two-stage pH response of poly(4-vinylpyridine) grafted gold nanoparticles. *Macromolecules*, 41:7254–7256, 2008.

[132] M. Bradley and B. Vincent. Poly(vinylpyridine) core/poly(Nisopropylacrylamide) shell microgel particles: their characterization and the uptake and release of an anionic surfactant. *Langmuir*, 24:2421–, 2008.

[133] Y. Xu, L. Shi, R. Ma, W. Zhang, Y. An and X. Zhu. Synthesis and micellation of thermo-and pH-responsive block copolymer of poly(N-isopropylacrylamide)-block-poly(4-vinylpyridine). *Polymer,* 48:1711–1717, 2007.

[134] S. Y. Moon, S. Tanaka and T. Sekino. Crystal growth of thiol-stabilized gold nanoparticles by heat-induced coalescence. *Nanoscale Research Letters*, 5:813–817, 2010.

[135] S. R. Rudge, T. L. Kurtz, C. R. Vessely, L. G. Catterall and D. L. Williamson. Preparation, characterization, and performance of magnetic iron-carbon composite microparticles for chemotherapy. *Biomaterials,* 21:1411–1420, 2000.

[136] A. P. Philipse, M. P. B. Vanbruggen and C. Pathmamanoharan. Magnetic silica dispersions - preparation and stability of surface-modified silica particles with a magnetic core. *Langmuir,* 10:92–99, 1994.

[137] H. H. Yang, S. Q. Zhang, X. L. Chen, Z. X. Zhuang, J. G. Xu and X. R. Wang. Magnetite-containing spherical silica nanoparticles for biocatalysis and bioseparations. *Analytical Chemistry*, 76:1316–1321, 2004.

[138] P. Tartaj, T. Gonzalez-Carreno and C. J. Serna. Single-step nanoengineering of silica coated maghemite hollow spheres with tunable magnetic properties. *Advanced Materials*, 13:1620, 2001.

[139] D. K. Yi, S. T. Selvan, S. S. Lee, G. C. Papaefthymiou, D. Kundaliya and J. Y. Ying. Silica-coated nanocomposites of magnetic nanoparticles and quantum dots. *Journal of the American Chemical Society,* 127:4990–4991, 2005.

[140] W. Stöber, A. Fink and E. Bohn. Controlled growth of monodisperse silica spheres in micron size range. *Journal of Colloid and Interface Science*, 26:62–69, 1968.

[141] P. Tartaj, C. J. Serna, Microemulsion-assisted synthesis of tunable superparamagnetic composites, *Chemistry of Materials*, 14:4396–4402, 2002.

[142] S. Giri, B. G. Trewyn, M. P. Stellmaker, V. S. Y. Lin, Stimuli-responsive controlled-release delivery system based on mesoporous silica nanorodscapped with magnetic nanoparticles, *Angewandte Chemie-International Edition*, 44:5038–5044, 2005.

[143] P. P. Yang, S. S. Huang, D. Y. Kong, J. Lin and H. G. Fu. Luminescence functionalization of SBA-15 by YVO4 : Eu^{3+} as a novel drug delivery system. *Inorganic Chemistry*, 46:3203–3211, 2007.

[144] Y. Chen, J. Chen, J. Dong and Y. Jin. Comparing study of the effect of nanosized silicon dioxide and microsized silicon dioxide on fibrogenesis in rats. *Toxicol. Ind. Health*, 20:21-27, 2004.

[145] X. Yang, J. Liu, H. He, L. Zhou, C. Gong, X. Wang, L. Yang , J. Yuan, H. Huang, L. He, B. Zhang and Z. Zhuang. SiO_2 nanoparticles induce cytotoxicity and protein expression alteration in HaCaT cells. *Particle and Fibre Toxicology,* 7:1, 2010.

[146] V. Rondeau, H. Jacqmin-Gadda, D. Commenges, C. Helmer and J. F. Dartigues. Aluminum and silica in drinking water and the risk of Alzheimer's disease or cognitive decline: Findings from 15-year follow-up of the PAQUID cohort. *American Journal of Epidemiology*, 169:489–496, 2009.

[147] L. Wide. *Radiommunoassay methods*. Kirkham & Hunter, E&S Livingstone, Edingburgh, 1970.

Chapter 2

Experimental and methods

2.1 Introduction

In this chapter materials and methods are described, as well as the experimental procedures for the synthesis of the MNPs that are used in the work described in next chapters. These samples are prepared in both aqueous and organic solvents. As the formation mechanisms of the particles are different depending on the reaction media, a brief summary of mechanisms is given in order to explain the main differences between the MNPs, and reveal the characteristics that can be expected for the particles obtained in aqueous media and organic media. The morphological, chemical and physical characterization of six different ferrofluids is also included in this chapter.

2.2 Experimental

Depending on the application of MNPs, it is not only the size what is important. Many times the synthesis conditions need to be tuned so that the resulting nanoparticles have uniform size, and homogeneous shape. Moreover, the chemical composition and the crystal structure of these materials are desirable because they influence the behaviour of the ferrofluids. The reproducibility of the synthesis is also relevant in order to get ferrofluids with the same characteristics. Eventually, nanoparticle agglomeration must be avoided, so that the final product can be easily dispersed in a solution [1].

As we have previously explained, there are different procedures to prepare MNPs, however, we will focus here on aqueous media and on thermal decomposition of organic precursors in organic media. Depending on the application of the ferrofluid we choose, we will select the synthetic procedure that implies better conditions for that specific application.

2.2.1 A survey of methods for the production of ferrofluids in organic media

The production of ferrofluids in organic media has been widely studied. High temperature decomposition of organic precursors in organic media leads to monodisperse nanoparticles, but what is also important is that the method permits to tune the mean size of the nanoparticles. Moreover, the high growing temperature used in this method yields nanoparticles with high crystallinity. There are several methods based on the thermal decomposition of organic precursors, as summarized in Table 2.1. Several factors have to be considered in the synthesis process: nature of the solvent, temperature of reaction, types of precursor and surfactant and their concentrations, and even the speed at which the reactants are added, [2−5].

The use of metalorganic precursors and organic solvents in the production of inorganic nanoparticles was introduced in the middle 90s, when Murray et al prepared highly crystalline CdSe nanoparticles in this way [14]. Later, Alivisatos et al applied this method to the production of γ -Fe_2O_3 with variable particle size [6]. They used iron cupferron complexe $Fe(Cup)_3$ (Cup: N-nitrosophenylhydroxylamine, $C_6H_5N(NO)O^-$) as precursor in trioctylamine solvent, and they could vary the size of the nanoparticles from 4 to 10 nm by increasing the quantity of $Fe(Cup)_3$ injected and the reaction temperature. Since then, many other groups have used this methodology to synthesize nanoparticles of several compounds in a wide range of sizes.

Table 2.1: Methods for the production of ferrofluids in organic media

Precursor	Solvent	Surfactant	Reaction T	Particle size	Reference
$Fe(Cup)_3$	Trioctylamine	-	250-300ºC	4-10 nm	[6]
$Co(acac)_2{\cdot}4H_2O$	Diphenylether	Oleic acid Trioctylphosphine	100-300ºC	1-15 nm	[7]
$Pt(acac)_2$ $Fe(CO)_5$	Octyl ether	Oleic acid Oleylamine	298ºC	4 nm	[8]
$Fe(CO)_5$	Octyl ether	Oleic acid or lauric acid	298ºC	4-16 nm	[9]
$Fe(acac)_3$	Phenyl ether	Oleic acid Oleylamine	265ºC	4-20 nm	[10]
$Fe(CO)_5$	Decalin	Polyisobutene	170ºC	2-10 nm	[11]
$FeCl_2{\cdot}4H_2O$ $FeCl_3{\cdot}6H_2O$	Diethylene glicol	N-methyl diethanolamine	210-220ºC	6-17 nm	[2]
FeO(OH)	1-octadecene	Oleic acid	350ºC	20-30nm	[12]
$FeCl_2{\cdot}4H_2O$ $FeCl_3{\cdot}6H_2O$	1-octadecene	Oleic acid	300ºC	3-50 nm	[4]
$Fe(acac)_3$	Dibenzylether	Decanoic acid	200ºC	3-50 nm	[13]

In 2001 Murray and his group described the synthesis of Co and FePt nanoparticles based on high temperature decomposition of organic precursors. In order to obtain Co nanoparticles they decomposed cobalt acetylacetonate in diphenylether, and oleic acid and trioctylphosphine as stabilizers at 200ºC. Tailoring the ratio of the concentration of reagents to that of surfactants, and the temperature, they control the nanoparticles size in a range of 1−15 nm [7]. In other paper they

described the synthesis of 4 nm FePt nanoparticles. They used $Pt(acac)_2$ and $Fe(CO)_5$ as metal precursors and decomposed them in octyl ether with oleic acid and oleylamine as surfactants at 300ºC [8]. The same year, Hyeon and col. reported a two step synthesis of maghemite nanoparticles with a size range of 4–16 nm. In a first step they add $Fe(CO)_5$ to a mixture containing octyl ether and oleic acid or lauric acid at 100ºC, then they rose the temperature to 298ºC for 1h. In the second step they oxide the sample with $(CH_3)_3NO$. The nanoparticles were highly crystalline and monodisperse [9]. In 2002 Sun et al got 4 nm Fe_3O_4 nanoparticles by decomposition of $Fe(acac)_3$ in phenyl ether with 1,2-hexadecanediol, oleic acid, and oleylamine under nitrogen at 265ºC. To make larger Fe_3O_4 nanoparticles, they used a seed-mediated growth method [10].

Another variation of the high temperature decomposition method is to employ polymers instead of surfactants for the control of the particle size and to avoid nanoparticle agglomeration. Butter and col. reported the preparation of Fe nanoparticles with a 2 to 5 nm size in dilute solutions of decalin containing polyisobutene at 170ºC [11]. In 2004, Caruntu et al. described a method based on high temperature hydrolysis of chelate iron alkoxide complexes in solutions of the corresponding alcohol, diethylene glycol, and *N*-methyl diethanolamine. They obtained the chelate iron alkoxide from $FeCl_2 \cdot 4H_2O$ and $FeCl_3 \cdot 6H_2O$ and diethylene glycol, then a NaOH solution was added and leave to react for 5 h. They were able to produce nanoparticles from 6 to 17 nm [2]. In the same year, Yu was the first to report the synthesis of iron oxide nanoparticles with a particle size larger than 20 nm using non-toxic hydrated iron oxides as iron precursor in octadecene and oleic acid [12]. The next year, Jana et al. used an analogous procedure to obtain magnetite from 3 to 50 nm but in this case they started from iron chlorides instead hydrated iron oxides [4]. In 2010, Guardia and col. reported the effect of decanoic acid as a surfactant on the synthesis of iron oxide nanoparticles by thermal decomposition of $Fe(CO)_5$ in dibenzyl ether. They achieved nanoparticles ranging from 5 to 30 nm [13].

2.2.2 Synthesis of IOMNPs in organic solvents by thermal decomposition of $Fe(CO)_5$

In this work, we have used the synthesis method proposed by the group of Hyeon that yields highly crystalline and monodisperse γ-Fe_2O_3 nanoparticles [9]. As it can be seen in Figure 2.1, this procedure, which allows a variation of the particle size by controlling the experimental parameters, is based on the thermal decomposition of an iron precursor in the presence of a surfactant and subsequently the product is oxidized. The iron precursor is $Fe(CO)_5$, the solvent is dioctyl ether (OE) or dichlorobencene (DCB), the surfactant is oleic acid, and the oxidant is trimethylamine oxide.

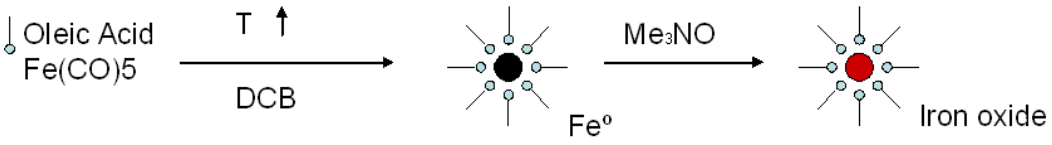

Figure 2.1 Iron oxide organic synthesis scheme.

Mechanisms of reaction: The formation of iron oxide nanoparticles in the Hyeon method occurs in several steps:

Step 1. Decomposition: In a first stage the $Fe(CO)_5$ complex is decomposed according to the following global reaction:

$$Fe(CO)_5 \rightarrow Fe^o + 5CO \quad (1)$$

According to Redl et al. the decomposition of the complex occurs already at 170°C, liberating all CO that is no longer observed in IR [15]. After decomposition of the precursor the iron seems to be in the form of Fe-oleate coordination compounds [16].

Step 2. Nucleation and growth. After an initation time, nucleation of Fe nanoparticles occurs.

$$\text{Fe-oleate} \rightarrow \downarrow \text{Fe NPs} \quad (2)$$

Fe-oleate complexes are very stable in solution and consequently initation times in the presence of oleic acid are large and the supersaturation at the burst of nucleation is very high, thus favouring monodispersity, as shown by Casula et al [17]. Nucleation of Fe nanoparticles occurs at 300ºC when the temperature is increased after decomposition of $Fe(CO)_5$. However, even when the reactants are added by rapid injection at 280–300ºC, initation times can be as long as 1 h. Using ligands weaker than oleate, such as oleylamine, or no ligand at all, results in shorter nucleation times and broader size distributions. The initation time and subsequently the size dispersion are also dependent of the temperature and of the reactants concentration.

Step 3. Oxidation. In the presence of a mild oxidant, trimethyl amine oxide, iron nanoparticles are oxidized to γ-Fe_2O_3.

$$\text{Fe NPs} + (CH_3)_3NO \rightarrow \gamma\text{-}Fe_2O_3 \quad (3)$$

The process of oxidation is not straightforward, but it goes through intermediate phases, first wüstite (FeO) and then magnetite (Fe_3O_4) [5]. Therefore, it is very important to ensure a complete oxidation to avoid a mixture of iron oxide phases in the final ferrofluid.

Particle size can be varied from 4 to 16 nm by controlling the experimental parameters. Particles in the order of 20 nm can be obtained by seeding the reaction media. Figure 2.2 shows a TEM micrograph of an organic ferrofluid prepared in this way.

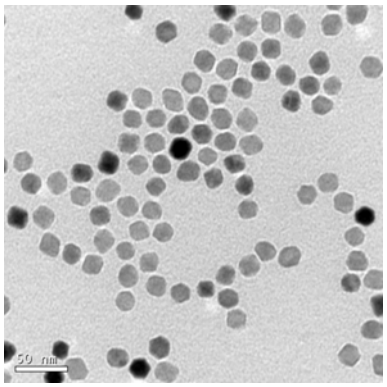

Figure 2.2 Transmission electron micrograph of an organic ferrofluid.

2.2.2.1 Procedure for the synthesis of organic MNPs suspensions

We have synthesised several ferrofluids in organic media that were later used in chapter 3 and 5 in the production of aqueous suspensions for biomedical applications. As pointed out above, the Hyeon method was used. The experimental set-up is shown in Figure 2.3. The organic solvent is placed in a three neck rounded flask together with the surfactant. A refrigerant is adapted to the central neck, and it is topped with a bubbler. The other two necks are closed with septa. In one of them a thermocouple is placed through the septum in order to control the reaction temperature. The last neck is used to inject the reactants. The procedure can be described as follows. An argon flux is passed through the experimental set up in order to remove the air. The temperature is raised to 100ºC and then the iron pentacarbonyl is injected through the septum. Then the temperature is raised gradually until the solvent boiling point. The reaction is left to react till the colour changes from yellow to black, from 2 to 48 hours, depending on the carbonyl/surfactant ratio. Iron nanoparticles were formed in this process. In order to obtain iron oxide nanoparticles the system is cooled to room temperature for oxidation. The oxidation is carried out by either employing a mild oxidant such as trimethylammonium oxide or by atmospheric air at high temperature.

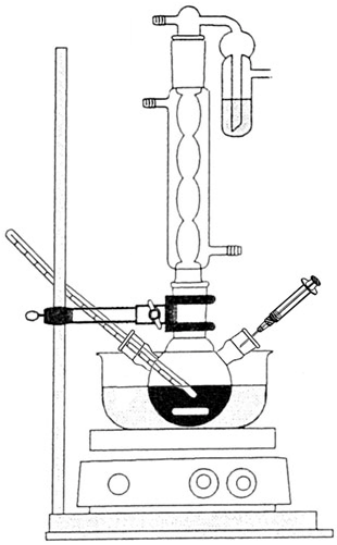

Figure 2.3 Experimental set up.

Five different organic ferrofluids were produced. The reaction conditions are summarized in Table 2.2, indicating the solvent, the precursor, the oleic acid and the oxidant quantities.

Table 2.2: Synthesis of an organic ferrofluid stabilized by oleic acid

Sample	Chapter	Solvent	$Fe(CO)_5$	Oleic acid	Trimethylamine oxide
A0	2	20 ml OE	0.4 ml	3.41 g	0.68 g
A1	3	40 ml DCB	0.8 ml	2.2 g	1.36 g
A2	3	30 ml OE	0.6 ml	3.4 g	air
A3	3	20 ml OE	0.4 ml	2.2 g	air
A4	5	40 ml DCB	0.8 ml	2.2 g	1.36 g

OE = dioctyl ether; DCB = dichlorobencene

2.2.3 Ferrofluids in aqueous media

The process of iron oxide precipitation in aqueous media is really complex. Iron(III) ions are initially in the form of $[Fe(H_2O)_6]^{3+}$ octahedral units [18]. These units link to each other by hydrolysis reactions generating protons, and the pH of the solution decreases to a level at which hydrolysis stops. When a base is added to the solution, the pH increases rapidly, and the hydrolysis process is restarted until the pH reaches a new equilibrium value, which depends on the iron concentration and the hydrolysis ratio, n = [OH]/[Fe]. Continuous hydrolysis results in the formation of dimers, then trimers and then linear iron polymers [18, 19] that become branched as n increases, as it can be seen in Figure 2.4. The precipitates are finally formed from these iron polymers by condensation [18, 20].

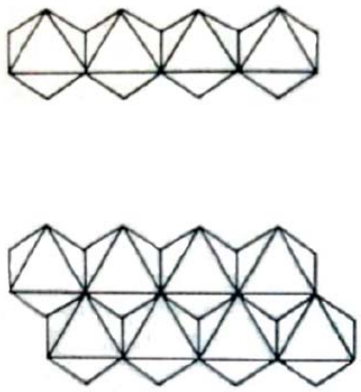

Figure 2.4 Chains of $Fe(H2O)_6]^{2+}$ octahedra.

Magnetite can be formed by addition of an alkali solution to an aqueous solution containing Fe(III) and Fe(II) in a molar ratio of 2. As explained above the hydrolysis of Fe(III) ions occurs readily at acid pH forming amorphous hydrated iron (III) oxides. Above pH=7, the Fe(II) ions also precipitate, first as green rust ($Fe(OH)_2$), and then as magnetite by redisolution of Fe(II) and Fe(III) intermediate oxides. The overall reaction can be expressed as:

$$[Fe(H_2O)_6]^{2+} + 2[Fe(H_2O)_6]^{3+} + 8OH \rightarrow Fe_3O_4 + 4H_2O$$

Magnetite is sensitive to oxidation transforming into maghemite. In aqueous solution is frequent to obtain mixtures of both phases, but oxidation in air is not the only way to transform Fe_3O_4 in γ-Fe_2O_3. Various electron or ion transfers are involved depending upon the pH of the suspension.

$$Fe_3O_4 + 2H^+ \rightarrow \gamma\text{-}Fe_2O_3 + Fe^{2+} + H_2O$$

The oxidation of magnetite to maghemite is a topotactic transformation. That implies migration of ferrous ions from the interior to the surface through the lattice framework, creating vacancies to maintain the charge balance.

A typical crystallization process involves two stages: 1) a short burst of nucleation when the concentration of the species reaches critical supersaturation, and 2) a slow growth of the nuclei by diffusion of the growth units to the particle surface. To produce monodisperse iron oxide nanoparticles, these two stages must be separated. This means that nucleation should be avoided during the period of growth like in a LaMer precipitating system, see Figure 2.5. In this system the particle size decreases with the concentration of reactants [21].

In iron oxide aqueous systems, the precipitation occurs by condensation of polymeric precursors, which size will increase with the iron concentration in solution. Thus, one may expect that the size of iron oxide particles precipitated in aqueous solutions should increase with the concentration of iron in the medium, as it is actually the case.

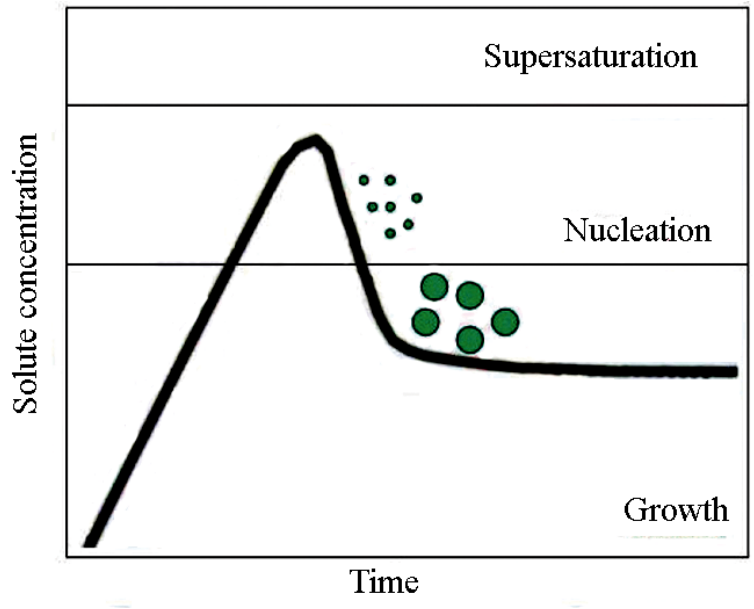

Figure 2.5 Formation mechanism of uniform particles in solution. LaMer diagram.

Nevertheless, uniform particles can also be obtained after multiple nucleation and growth stages (Figure 2.6). This spontaneous process occurs because larger particles are more energetically favoured than smaller particles [22]. Molecules on the surface of a particle are energetically less stable than the ones already well ordered and packed in the interior. Large particles, exhibit lower surface to volume ratio that results in a lower energy state. As the system tries to lower its overall energy, molecules on the surface of a small particle will tend to detach and diffuse through solution and then attach to the surface of larger particle. Therefore, the number of smaller particles continues to decrease, while larger particles continue to grow. In aqueous media, Ostwald ripening causes the diffusion of monomers from smaller to larger particles due to greater interaction of the single monomer molecules in the larger particles. The rate of this diffusion process is linked to the solubility of the monomer in the continuous water phase.

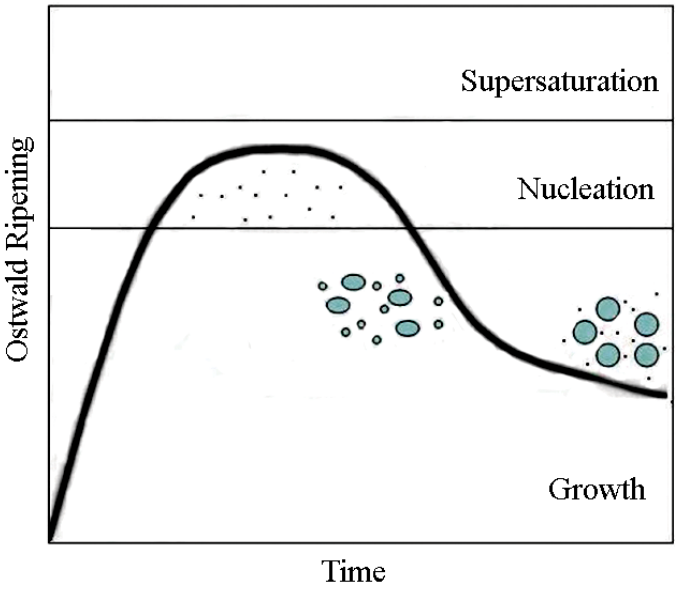

Figure 2.6 Formation mechanism of uniform particles in solution. Ostwald ripenning.

The main advantage of iron oxide production in aqueous media is that the nanoparticles are already in a biological fluid. The principal drawbacks of this procedure is that the resulting nanoparticles are not homogeneous in shape and size, see Figure 2.7, and due to the complex mechanisms involved, it is difficult to control the iron oxide phase that originates a coexistence of different phases. Nevertheless, depending on the application for which the MNPs are destined, these drawbacks can be irrelevant.

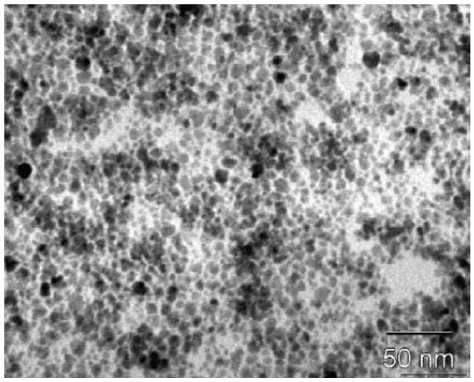

Figure 2.7 Transmission electron micrograph of an aqueous ferrofluid.

2.2.4 Procedure for the synthesis of aqueous MNPs suspensions

The methodology used here for the production of aqueous iron oxide ferrofluids consists on the formation of maghemite nanoparticles by basic hydrolysis of iron halogenide precursors and subsequent coating with a silica shell by different methods employing tetraethyl orthosilicate (TEOS) as silica precursor. We employed iron bromides as precursors because it is easier to control the crystalline phase than with other halogenate precursors.

In a typical synthesis of maghemite nanoparticles, 0.5 ml of $FeBr_3$ 1M were mixed in a beaker with 0.25 ml of $FeBr_2$ 1M. Then 3.75 ml of NaOH 1M were added with mechanical stirring and maintained 30 min under agitation.

2.3 Methods

2.3.1 Chemical analysis

The chemical characterization of the ferrofluids consisted of iron titration, thermogravimetric analysis, gel permeation chromatography and nuclear magnetic resonance. Iron titration was used to analyse the presence of Fe(II) ions in the particles in order to determine the maghemite/magnetite ratio because XRD is not enough to differentiate between these two iron oxide structures. We used thermogravimetric analysis to quantify the amount of organic compounds in the particle coating. Finally, we also use gel permeation chromatography and nuclear magnetic resonance to determine the composition and molecular weight of the polymers that were used as coatings

2.3.1.1 Iron titration

The percentage of Fe(II) and total Fe in iron oxide samples is determined by titration with a standard solution of potassium dichromate (VI). Amounts of iron oxide samples were dissolved in concentrated HCl, and then H_3PO_4 was added to decolorize

the solution by formation of colourless Fe(III) complexes, that makes the detection final point more clear and increase the reaction speed.

The overall titration reaction to determine the Fe(II) quantity is:

$$6Fe^{2+} + Cr_2O_7^{2-} + 14H^+ \rightarrow 6Fe^{3+} + 2Cr^{3+} + 7H_2O$$

In order to determine the total iron content all of the iron in solution must be in the Fe(II) state prior to titration. Thus, the sample solution was treated with tin (II) chloride in hot HCl media to reduce any amount of Fe(III) in the sample:

$$SnCl_4^{2-} + 2\ Fe^{3+} + 2Cl^- \rightarrow SnCl_6^{2-} + 2\ Fe^{2+}$$

The excess Sn(II) is then removed by reaction with mercury (II) chloride, which produces insoluble mercury (I) chloride:

$$SnCl_4^{2-} + 2\ HgCl_2 \rightarrow SnCl_6^{2-} + Hg_2Cl_2$$

The $HgCl_2$ addition has to be fast and at low temperature in order to avoid the following reaction:

$$SnCl_4^{2-} + HgCl_2 \rightarrow SnCl_6^{2-} + Hg$$

Potassium dichromate (VI) solution turns green as it reacts with the Fe(II) ions. Nevertheless, we have used a redox indicator, ferroin, for a more clear detection. Ferroin changes its colour from orange to pale green in the absence of Fe(II). The standard procedure is to put three drops of ferroin in the dissolved and decoloured sample and titrate it with potassium dichromate (VI) 0.01M. In order to determine the content of Fe(II) in the sample we dissolved the washed sample in HCl and H_3PO_4, then we added three drops of ferroin and titrated with potassium dichromate(VI) 0.01M.

Following this procedure we are able to say if we have a sample composed by maghemite or a mixture of maghemite and magnetite. If we find Fe(II) we can say that

we have some magnetite in our system, otherwise, if no Fe(II) was found, we can point that we have only maghemite. But we have to take into account that this is only valid in case the XRD pattern shows only the spinel structure.

2.3.1.2 Thermogravimetric analysis

Thermogravimetric analysis (TGA) is a type of assay performed on liquid or solid samples that determines changes in weight in relation to a gradual change in temperature in a controlled atmosphere. Simultaneous measurement of these two properties improves and simplifies interpretation of the results. Variations in weight denote evaporation of the solvents when no change in temperature is observed, but when there is an exothermic or endothermic change it can be due to a reaction or degradation process, a change in the composition of the sample occurs. When no change in weight and an exothermic or endothermic process is observed it involves melting or crystallization.

We use this methodology to know the concentration of some organic samples or find the relation between iron oxide nanoparticles and surfactant. The measurements were performed using a Mettler Toledo Star System TGA/SDTA851e in the presence of N_2 gas as inert atmosphere or air in order to get an oxidative atmosphere, with a heating rate of 20ºC/min. The temperature in many testing methods reaches 800ºC. The analyser consists of a high-precision balance with a container loaded with the sample. The container is placed in a small electrically heated oven with a thermocouple to accurately measure the temperature. The atmosphere may be purged with an inert gas to prevent oxidation or other undesired reactions. But some times an oxidative atmosphere is required in order to study the oxidation of maghemite.

2.3.1.3 Gel permeation chromatography

Gel permeation chromatography (GPC) is a term used for the separation of polymers depending on their size or their hydrodynamic volume. Separation occurs via the use of porous beads packed in a column. This differs from other separation methods which depend in chemical or physical interactions to separate polymers. The

smaller polymers can enter into the pores more easily and therefore spend more time in these pores, increasing their retention time. Larger polymers spend little if any time in the pores and are eluted quickly. All columns have a range of molecular weights that can be separated.

When a polymer is characterized, it is important to consider the polydispersity index (PDI) as well as the molecular weight. Polymers can be characterized by a variety of definitions for molecular weight including the number average molecular weight (M_n), the weight average molecular weight (M_w), the size average molecular weight (M_z), or the viscosity molecular weight (M_v).

The sample preparation consists of the dispersion of 1 mg of polymer in 1 ml of THF. The dispersion was filtered through a 0.45 μm organic filter. In our case molecular weight distribution (Mw/Mn) of the polymer was evaluated by GPC performed on a Alliance Waters 2695 auto-sampler separation module equipped with a Waters 2420 ELSD detector on two in line Phenogel 5 μm Linear/ Mixed (2) (7.8x300 mm) columns with a mixture of tetrahydrofuran /(methanol/ ethanol amine (99/1)) (70/30) as eluent at a flow rate of 1ml/min at 35℃. Polystyrene standards were used for calibration.

2.3.1.4 ^{1}H-NMR

Nuclear magnetic resonance (NMR) is based in the response of the magnetic nucleus of a substance to a magnetic field. The nuclei absorb the electromagnetic energy and then emit it. This energy absorbance occurs at a specific resonance frequency which depends on the magnetic field and other factors. But not all the atom nuclei are magnetic (non-zero nuclear spin), as it depends on the number of protons and/or neutrons. The most commonly studied magnetic nucleus is ^{1}H.

^{1}H-NMR is the application of nuclear magnetic resonance in NMR spectroscopy with respect to ^{1}H nuclei within the molecules of a substance, in order to determine the structure of its molecules. Simple NMR spectra are measured in solution, and solvent

protons must not be allowed to interfere. Deuterated solvents especially for use in NMR are preferred, like deuterated chloroform, $CDCl_3$.

^{1}H-NMR spectra of most organic compounds are characterized by chemical shifts in the range +12 to -4 ppm and by spin-spin coupling between protons. The integration curve for each proton reflects the abundance of the individual protons. ^{1}H-NMR spectra of the polymers were recorded at 300 MHz in $CDCl_3$ solution at room temperature using a BRUKER ARX-300 spectrometer.

2.3.2 Structural characterization

Some of the characterization techniques for nanomaterials differ from the characterization methods for macroscopic materials. Actually, the synthesis and study of nanomaterials have been rapidly developed since we have the appropriate methodologies to observe them. Since the transmission electron microscopes were developed the observation of nanoparticles and nanomaterials was easily achieved. Nowadays, we are able to study the morphology and the size, but also the structure of these materials with a transmission electron microscope tool, the selected area electron diffraction. Moreover, chemical information about the samples can be obtained by means of another transmission electron microscope tool, the electron energy loss spectroscopy. Due to these applications, the transmission electron microscope is a very helpful device for nanoscience. Otherwise, it is also useful the utilisation of classical characterization tools as infrared, dynamic light scattering or X ray diffraction, that are cheaper and more accessible.

2.3.2.1 Fourier transform infrared spectroscopy

The main aim of infrared (IR) absorption spectroscopy is to measure how a sample absorbs light at different wavelength. Chemical bonds have specific frequencies at which they vibrate corresponding to energy levels. Resonant frequencies can be related to the strength of the bond and the mass of the atoms. Thus the frequency of the vibrations can be associated with a particular bond type. In order to analyze a sample a monochromatic light beam is directed to the sample and how

much of the light is absorbed is measured. This step is repeated for each distinct wavelength. Fourier transform infrared spectroscopy (FTIR) is a less intuitive way to obtain information. This technique is based in the impact of a beam containing many different frequencies of light at once to the sample, and measures how much of that beam is absorbed by it. Then, the beam is modified to contain a different combination of frequencies, giving a second data point. This process is repeated many times. Afterwards, a computer takes all these data and gives the absorption at each wavelength.

The samples were measure in a Spectrum 100 FTIR, its optical module contains a Helium Neon laser, which emits visible, continuous wave radiation at a wavelength of 633 nm and a maximum power of 1 mW. This system enables to collect data over a total range of 7800 to 370 cm^{-1} with a best resolution of 0.5 cm^{-1}.

2.3.2.2 X-ray diffraction

Powder x-ray diffraction (XRD) is a method for determining the localization of atoms within a crystal, in which a beam of x-rays interacts with the crystal powders and diffracts into specific directions. From the angles and intensities of these diffracted beams, the positions of the atoms in the sample can be determined, as well as their chemical bonds, their disorder, the nanoparticles average size and various other information.

Relative to other methods of analysis, powder diffraction allows for rapid and non-destructive analysis of multicomponent mixtures without complicated sample preparation. The positions, corresponding to lattice distances, and the relative intensity of the peaks are indicative of a particular phase and material, providing a "fingerprint" for comparison to the standards database Joint Committee on Powder Diffraction Standards (JCPDS).

The XRD patterns of the dry nanoparticles samples were obtained using a D-Max Rigaku diffractometer equipped with a CuKa1 radiation source. The dry powders were

separated from the as prepared organic suspensions by addition of acetone, washed three times with acetone, and dried in air.

2.3.2.3 Dynamic light scattering

The potential uses for metal oxide nanoparticles are often size dependent. Dynamic light scattering is a physical technique that can be used to determine the size distribution of small particles in suspension. The basic principle in this technique is the measurement of the scattering of an incident monochromatic and coherent beam of light in to a sample (composed by particles in suspension) with time. DLS measures Brownian motion of the particles in solution and relates this to the size of these particles. The particle size distributions are often reported in terms of volume, number or scattering intensity but usually produce different interpretations of the results, despite the data come from exactly the same sample. When comparing size results obtained by DLS with electron microscopy, it must be noticed that the best corresponding DLS size distribution for comparison is the number distribution for us, because in microscopy techniques particle are counted and sorted into histograms from the images.

The DLS measurements were preformed on a Malvern Zetasizer Nano-ZS (Malvern Instruments, Malvern, UK). Diluted suspensions of the samples were irradiated with red light (HeNe laser, wavelength λ= 632.8 nm) and the intensity fluctuations of the scattered light (detected at a backscattering angle of 173º) analysed to obtain an autocorrelation function. Samples were measured in disposable polystyrene cuvettes at a temperature of 25℃. Data were acquired in automatic mode, ensuring enough photons were accumulated for the result to be statistically relevant. The software (DTS v 5.03) incorporates a "data quality report" that indicates good quality for all data obtained, and provides both the size mean and polydispersity index (PdI), employing the size distribution data obtained by intensity. Measurements were conducted in triplicate.

2.3.2.4 Transmission electron microscopy

Transmission electron microscopy (TEM) is a microscopy technique based on a beam of electrons that is transmitted through a sample. The electrons interact with the sample as they pas through it and an image is formed. The image is magnified and focused in an imaging device, as a fluorescent screen, on a photographic film, or registered in a digital camera. TEMs are capable of imaging at a significantly higher resolution than light microscopes. At smaller magnifications TEM image contrast is due to absorption of electrons in the material, due to the thickness and composition of the material. At higher magnifications complex wave interactions modulate the intensity of the image, requiring expert analysis of observed images. Alternate modes of use allow us to observe chemical properties, crystal orientation and electronic structure as well as the sample image.

Electron energy loss spectroscopy (EELS) is a technique that can be performed inside a TEM and permits to obtain maps of elements of a sample. In order to achieve that, a sample is exposed to electron beam energy. The electron paths are slightly deflected and detected so the energy loss can be measured. The inner shell ionizations are especially useful for determining the elemental components of the sample.

Selected area electron diffraction (SAED) is a crystallographic technique associated to a TEM microscope. The electron beam hits the sample, and the electrons are diffracted to particular angles, allowing the characterization of the crystalline structure of a selected area. The result is an image that consists of a series of spots called SAED patterns that are a projection of the reciprocal lattice. This technique is similar to x-ray diffraction but the area of analysis is in the nanometer scale.

Sample preparation is a necessary prerequisite for TEM. In order to be transparent to an electron beam, the samples must be thin, typically about 100 nm or less depending on the average atomic number of the material. Particulate materials sample preparation normally consists on transferring a suspension of the particles in a solvent to a carbon coated grid, and letting the solvent to evaporate. Our TEM samples were

prepared by putting a drop of the as prepared suspension on a carbon coated copper grid and then dried in air. The grid was then placed under a Philips CM-30 instrument. The images were taken at an acceleration voltage of 300 kV. Another microscope that we have used is a Hitachi 800MT with Gatan Multiscan chamber working at an acceleration voltage of 200 kV. EELS spectra were obtained in a Gatan Image Filter (GIF2000) coupled to a Jeol 2010F microscope.

2.3.3 Magnetic characterization

The magnetic behaviour of the MNPs that compose our systems is very important in order to decide if they are suitable for the potential applications that they are conceived for. Measurements of magnetization provide us information about the sample magnetic properties, like superparamagnetism, a valuable property for certain applications requiring the particles to be single domain and to remain not aggregated after the removal of a magnetic field. But we also are interested in the heating capacity of the MNPs. The SAR of a ferrofluid depends on the magnetic field strength and the field frequency. But it also depends on the ferrofluid characteristics, as the magnetic particle size and the magnetic particle concentration.

2.3.3.1 Magnetic measurements SQUID

Measurements of magnetization versus applied field at a fixed temperature provide us information about the response of the MNPs to a magnetic gradient. The measurement of the magnetization while the temperature is increasing allows us to estimate the magnetic size of the particles and also to calculate the blocking temperature of the ferrofluid, in other words, the temperature above which the sample becomes superparamagnetic.

The magnetic properties of nanoparticles were determined with a commercial SQUID magnetometer (MPMS, Quantum Design). The measurements were performed on ferrofluid samples in organic and aqueous solvents. The dispersions were diluted down to a certain concentration and then frozen inside a capsule of gelatine or polycarbonate depending on the solvent.

2.3.3.1 SAR

SAR was determined by a calorimetric method using a special purpose magneto-thermal setup [23] working under adiabatic conditions. Compared to current nonadiabatic installations, this setup and method allows direct measurement of sample temperature increments with negligible heat losses, overcoming the limitation of heat dissipation for SAR estimation in standard SAR equipments.

2.4 Characteristics of the organic MNPs suspensions

Five different organic suspensions samples of monodisperse iron oxide nanoparticles, A0−A4, have been prepared, according to the methods described above, which have been used in the following chapters as the starting materials for the preparation of biological ferrofluids. Sample A0 has been used to explore the magnetothermic effect of iron oxide nanoparticles when they are submitted to an alternating magnetic field. Samples A1, A2 and A3 have been used in chapter 3 for the preparation of monodisperse silica coated aqueous ferrofluids for biomedical applications. And sample A4 has been used in chapter 5 for the preparation of polymer coated aqueous ferrofluids for drug delivery. Here we present the results of the structural characterization of these samples. The main structural parameters are shown in Table 2.3.

Table 2.3: Structural parameters of the organic ferrofluids

Sample	Structure	Diameter (nm) (TEM)	Hydrodynamic diameter (DLS)
A0	98.7% Maghemite 1.3 % Magnetite	11.6 ± 1	14 nm
A1	Magnetite & Maghemite	5.9 ± 1	11 nm
A2	Magnetite & Maghemite	9.6 ± 1.5	15.5 nm
A3	97.2 % Maghemite 2.8 % Magnetite	13.5 ± 2.5	11 nm
A4	99.97% Maghemite 0.03 % Magnetite	5.7 ± 1	_

Fig. 2.8 shows the x-ray diffraction patterns of dry powder samples separated from the as prepared organic suspensions by addition of acetone as described in section 3.2.2. All the patterns show the typical broad peaks of nanoparticles of iron oxide spinel structure at angles 2θ close to 2.95, 2.52 2.09, 1.70, 1.61, 1.48 corresponding to (2 2 0), (3 1 1), (4 0 0), (4 2 2), (5 1 1) and (4 4 0) reflections of maghemite crystal structure. No other peaks are observed apart from these ones, confirming the phase purity of the samples.

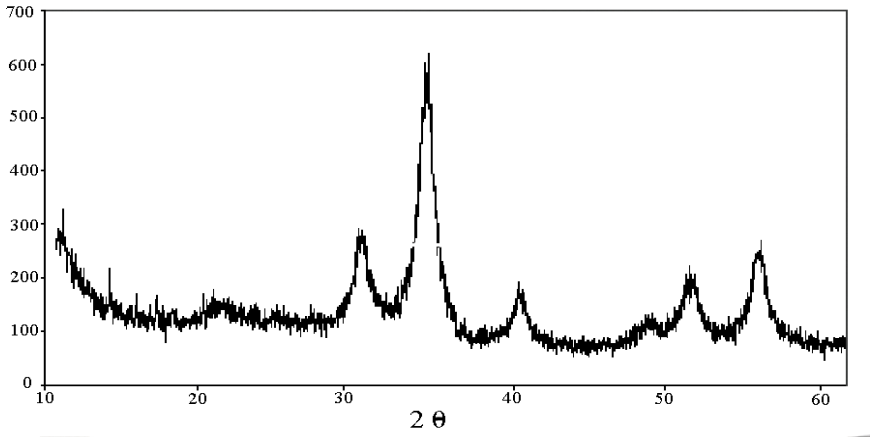

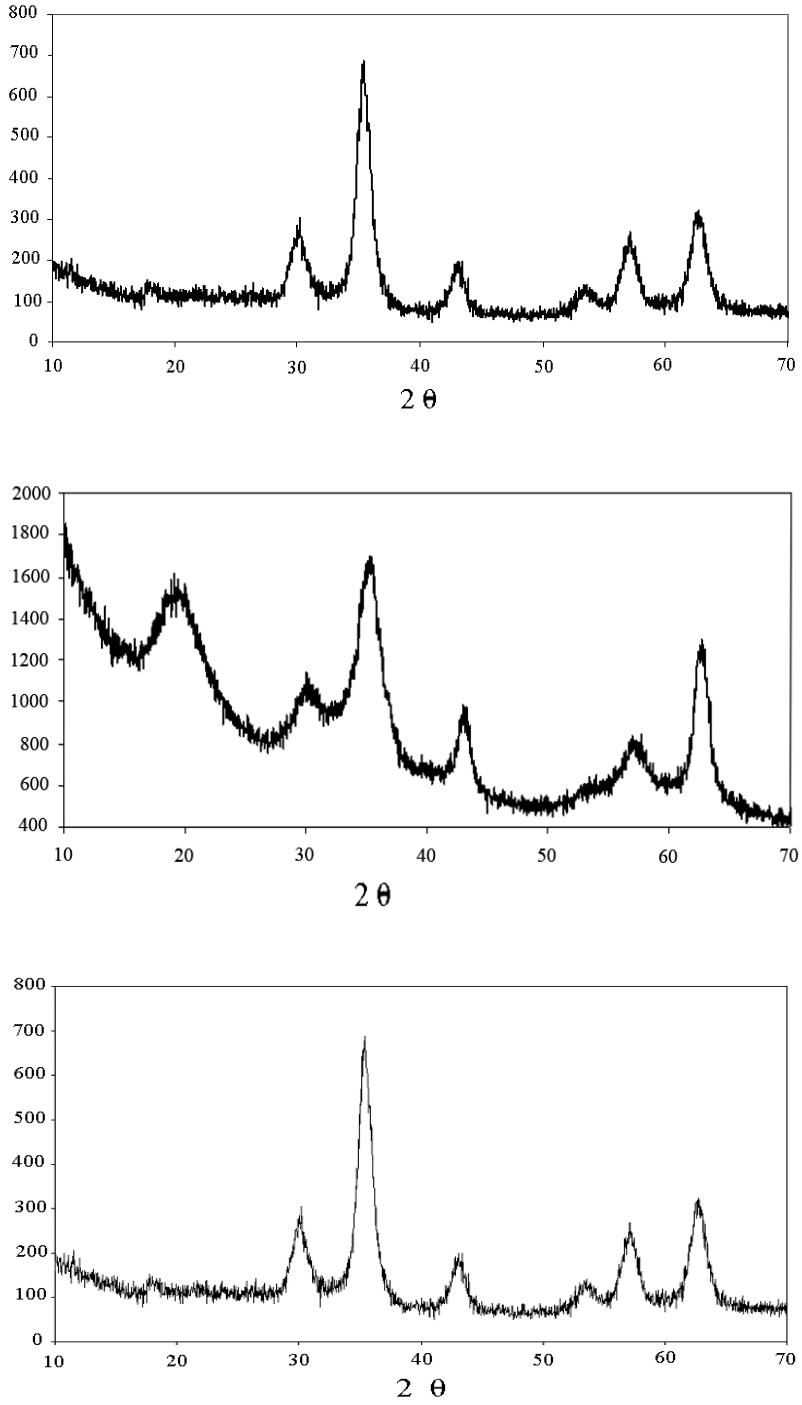

Figure 2.8 XRD of A0, A1, A2 and A4 powder samples.

The crystal structure of sample A3 was determined from electron diffraction patterns that are also consistent with maghemite crystal structure as shown in Fig. 2.9. By the titration method we find that this sample is composed by 97.2 % of maghemite.

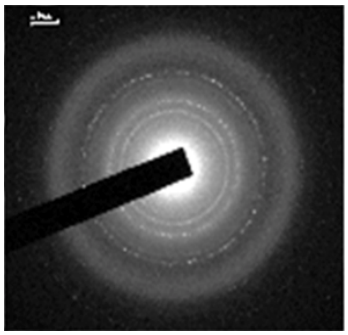

Figure 2.9 Electron diffraction pattern of sample A3 showing rings corresponding to interplanar distances: 2.99, 2.51, 2.10, 1.65, and 1.50 A that are close to the main reflections in maghemite structure: (220), (311), (400), (422), (511), (440) (2.95, 2.52, 2.09, 1.70 and 1.48 A).

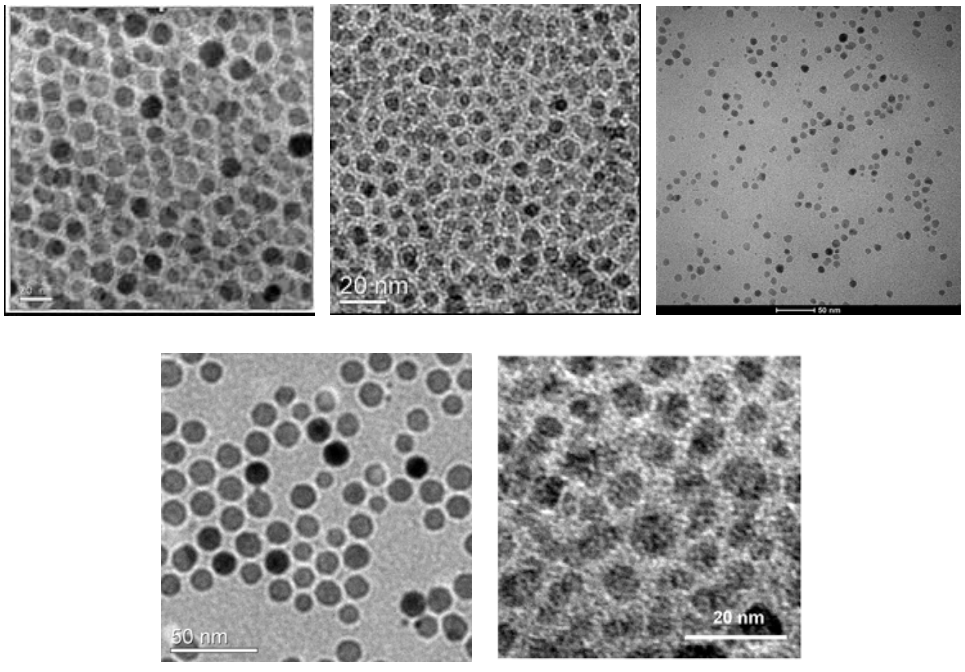

Figure 2.10 TEM image of the as prepared iron oxide nanoparticle samples A0, A1, A2, A3 and A4.

TEM images in Fig 2.10 show, in all cases, electron-dense spherical nanoparticles covered with a layer of light material corresponding to the oleic acid coating.

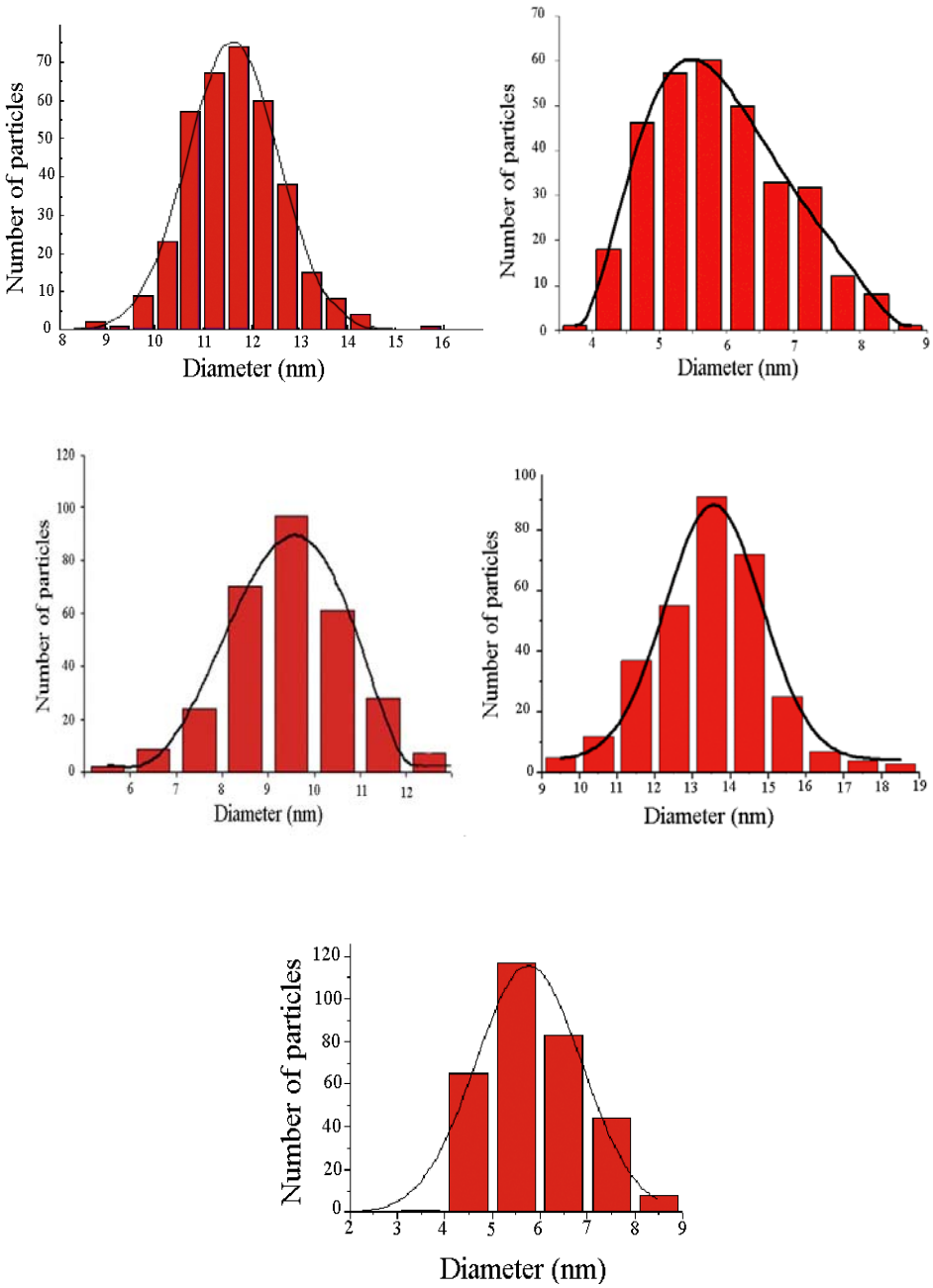

Figure 2.11 Histograms of TEM nanoparticle size distributions of A0−A4 samples.

A particle size analysis performed over a population of 300 nanoparticles yield narrow size distributions with average sizes 11.6 ± 1 nm, 5.9 ± 1 nm, 9.6 ± 1.5 nm, 13.5 ± 2.5 nm, and 5.7 ± 1 nm for samples A0, A1, A2, A3 and A4, respectively. Histograms shown in Fig 2.11 fit well to log-normal distributions.

The distribution of hydrodynamic sizes from DLS measurements are shown in Fig. 12. The average hydrodynamic diameters, $D_{H,}$ are 14, 11, 15.5 and 11 for samples A0, A1, A2 and A3 respectively. Comparing D_H values with D_{TEM} values it is apparent that the former are consistently higher than the later, as it should be expected because the hydrodynamic diameter includes the shell of surfactant and solvation molecules around the particle.

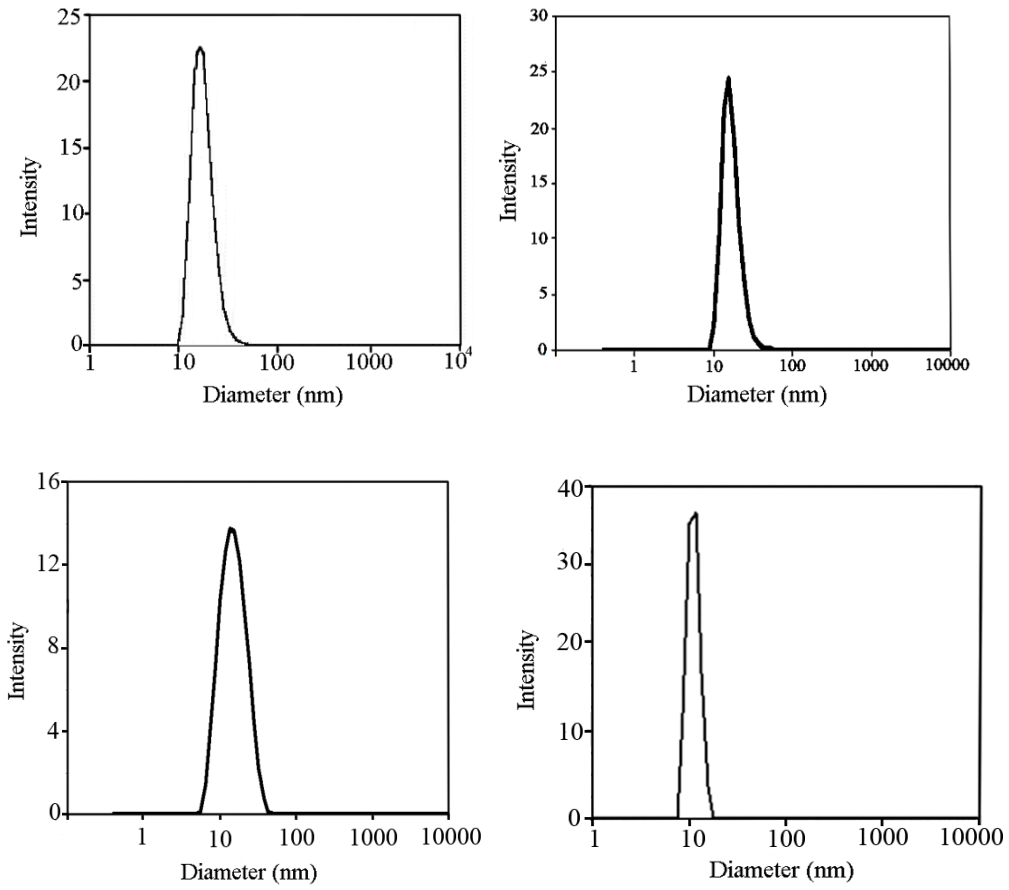

Figure 2.12 Hydrodynamic diameter of A0−A3 samples.

Sample A3 was also examined by thermogravimetry. The TGA plot is shown in Fig. 2.13. For instance, a loss of 47.5wt% can be observed in between 200ºC and 400ºC that can be attributed to evaporation of the OA surfactant layer covering the iron oxide nanoparticles.

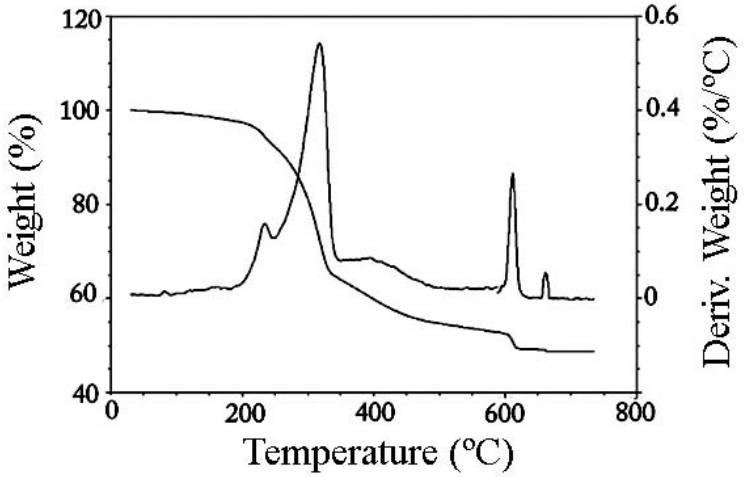

Figure 2.13: TGA profile of the washed and dried IO@OA sample.

2.5. Magnetic properties of the organic MNPs suspensions

The magnetic properties of the precursor organic ferrofluids have been also determined. The sample A4 was found to have 99.97% of maghemite in its composition by the titration method. An additional method to identifying the iron oxide phase was to measure the saturation magnetization of the sample. The magnetization curves of sample A4 (Figure 2.14a) indicate a superparamagnetic behaviour at 200 K, with no hysteresis, and a blocked magnetic moment at 5 K, with coercive field of 240 Oe. The saturation magnetization M_S was 75 emu/g Fe_2O_3, that is in agreement with the typical values for maghemite [24]. The anisotropy constant was estimated from the analysis of the ac susceptibility measurements. The out-of-phase susceptibility component χ'' Figure 2.14b presented a maximum at the average blocking temperature T_B (χ'') [25].

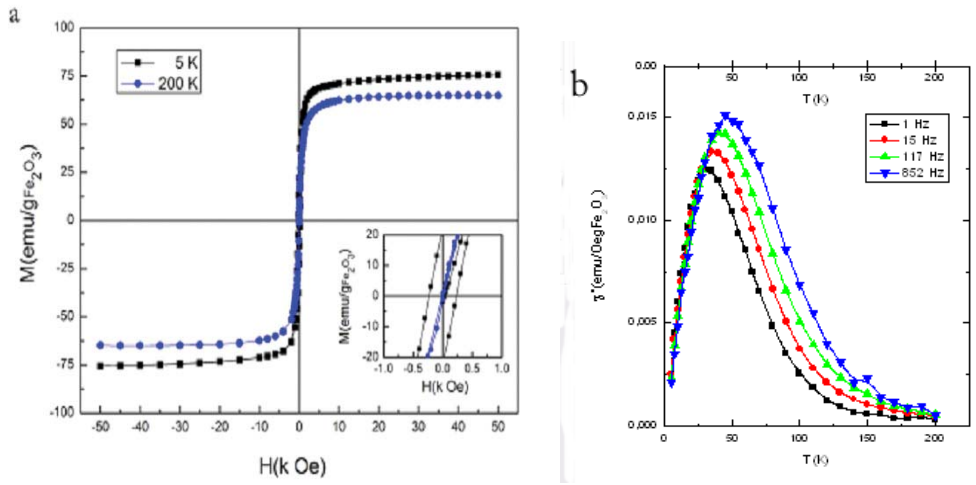

Figure 2.14 a) Magnetization curves at 200 and 5K, b) Susceptibility.

The dependence of T_B with the excitation frequency of the alternating field was well described by the Arrhenius law. The fitting to the expression:

$$T_B(\chi'') = \left(\frac{U}{K_B}\right) \ln\left(\frac{1}{2\pi f \tau_0}\right)$$

where the activation energy U is, as a first approximation, proportional to the average particle volume:

$$U = K_{eff} V$$

The effective anisotropy constant K_{eff} = 1.7 x 10^5 erg/cm^3 (1.7 x 10^4 J/m^3) was in the range expected for maghemite nanoparticles [26].

2.6 Magnetothermic properties of the organic MNPs suspensions

The amount of heat released by magnetic nanoparticles subject to an alternating magnetic field is a key factor for some biomedical applications, like magnetic fluid hyperthermia for cancer treatment or thermally-assisted drug release. Thus, it is important to determine the specific absorption rate (SAR) of the ferrofluid we use.

In practice, the spatial arrangement, concentration and possible agglomeration of the magnetic nanoparticles within the tissues may differ considerably from those of the initial ferrofluid. Therefore, these are also parameters to take into account when studying the nanoparticles performance, since they can modify their heating capacity and, consequently, the heat they produce. In particular, the magnetic nature of the particles may give rise to inter-particle interactions. Although the effects of such interactions have been widely studied from the point of view of magnetic properties, very few works dealing with such effects on the heating ability are found in the literature. Here we present a SAR study of three ferrofluids obtained from the same sample in order to find how the concentration affects the heating capacity.

SAR accounts for the heating power per mass unit of dissipating material. Direct temperature increments, ΔT, obtained upon application of ac-magnetic-field pulses during a time interval, Δt, were determined. SAR was then calculated as

$$SAR = \left(\frac{1}{m_{NP}} \right) C_t \left(\frac{\Delta T}{\Delta t} \right)$$

where m_{NP} is the mass of magnetic material and C_t, the heat capacity of the whole sample. For the case of maghemite or magnetite nanoparticles, widely used due to their biocompatibility, these sizes lie well below the critical size of single domain particles. Such particles are likely to lie also in the superparamagnetic regime, in which the heat dissipation is due to the thermal relaxation of magnetic moments. In this situation, it has been demonstrated that monodisperse particles give optimum SAR values, and that the heating power decreases strongly as the standard deviation of the

size distribution increases [27]. As iron oxide nanoparticles with an average diameter of 5 nm are very small to produce significant SAR values, we selected sample A0, a ferrofluid with an average size bigger than 10 nm. The A0 sample was composed of well dispersed, highly-crystalline and monodisperse nanoparticles with an average diameter of 11.6 nm, and an initial concentration of 8.14 mg/ml. Its structure was determined by the titration method, ant it was found to be 98.7% maghemite. Moreover we profit the chance to study the variation of the SAR value with the sample concentration. First of all, a magnetic characterization of three different concentrations of this ferrofluid was performed (see Table 2.4). As shown in Figure 2.15, the M(H) curves reveal several effects typical of the presence of magnetic interactions, such as the decrease of initial susceptibility values, as it can be seen in Table 2.4.

Table 2.4: SAR values for different concentration

Sample	Concentration (mg/ml)	SAR (W/g)	X”
FF100	8.14	0.38	5.22
FF50	4.65	0.47	5.52
FF25	1.89	0.89	6.12

The initial susceptibility is larger for the dilutions than for the original fluid, which responds less readily to the applied field than the dilutions. This fact suggests that as the ferrofluids concentration increases, the alignment of the nanoparticle magnetic moments parallel to the external field is hindered.

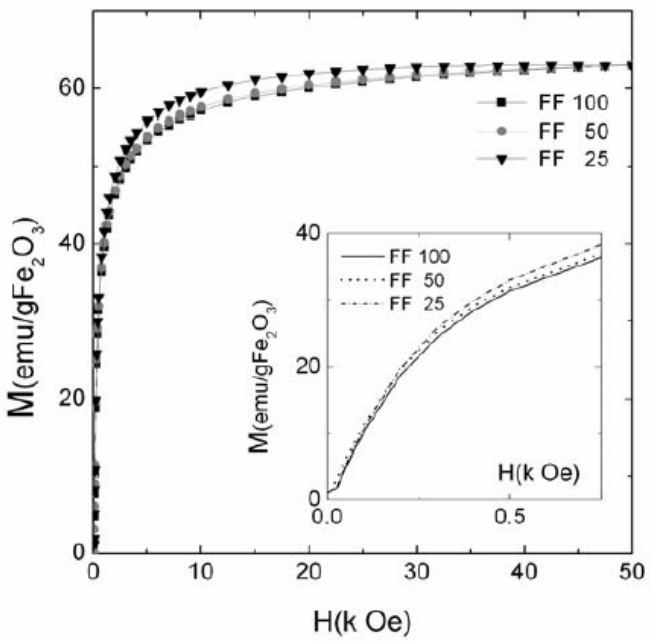

Figure 2.15 dc magnetization curves at room temperature. Inset: detail susceptibility variation at low fields.

As an example of this type of measurements, Figure 2.16 shows three pulses, one for each sample. Due to the low concentration of the samples, we measured T values lower than 1^{o}C, fact that explains the slight dispersion of the experimental data. Given that the original and diluted ferrofluids come from the same batch, with identical magnetic nanoparticles, SAR values, expressed in watts per gram of magnetic material, should be also similar, and so should the increments. However, these increments are higher for the dilutions, respectively, about 24 % and 134 % higher, for samples FF50 and FF25. This fact points out a loss of heating power with increasing ferrofluid concentration.

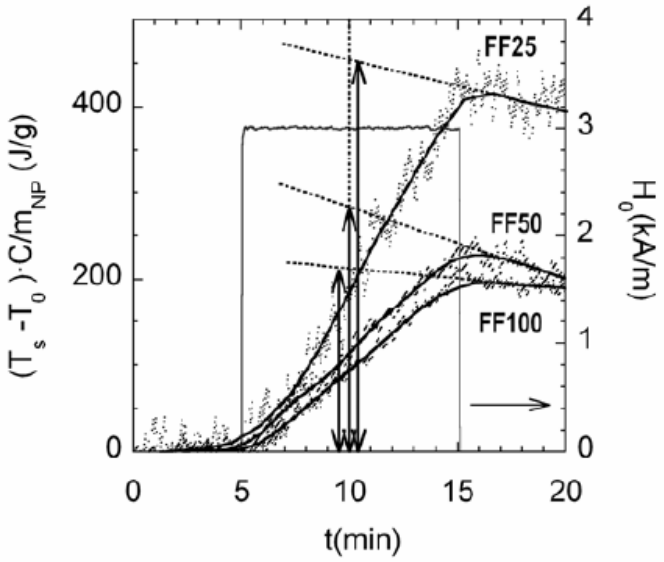

Figure 2.16 Heating steps at f= 109 kHz: experimental data with a smooth field. The dotted lines are extrapolation of the T drifts after ac-field application.

As it can be observed in Table 2.4, the SAR of a ferrofluid, measured at 315 K, 3 kA/m and 109 kHz was found to double as the ferrofluids concentration was decreased by a factor 4.

Summarily, in our case, four times more concentrated sample implies half SAR value, that is, half the nanoparticle mass can be used to obtain the same temperature increase, because the concentration of the sample promote interactions between particles.

2.7 Characteristics of aqueous prepared ferrofluids

Ferrofluid B1 was synthesised as we described before. In Figure 2.17 it can be seen the TEM micrograph of the sample, the shape of the nanoparticles is irregular and the size dispersion is wide, but we can estimate an average size of 5 nm (Figure 2.18).

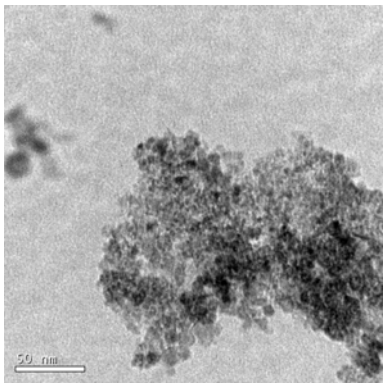

Figure 2.17 Transmission electron micrograph of ferrofluid B1.

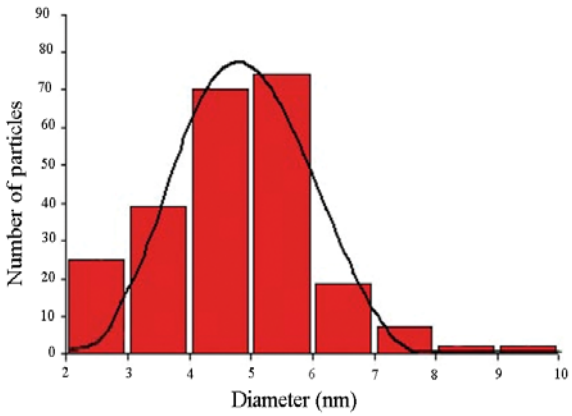

Figure 2.18 Histogram of iron oxide aqueous nanoparticles.

From Figure 2.17 we can say that the particles are agglomerated, moreover it confirmed by DLS (Figure 2.19). The XRD pattern, in Figure 2.20, shows that the sample is composed by iron oxide inverse spinel structure, as it can be maghemite and

magnetite. We can also indicate that the peaks are very broad due to that the sample is composed by small nanoparticles.

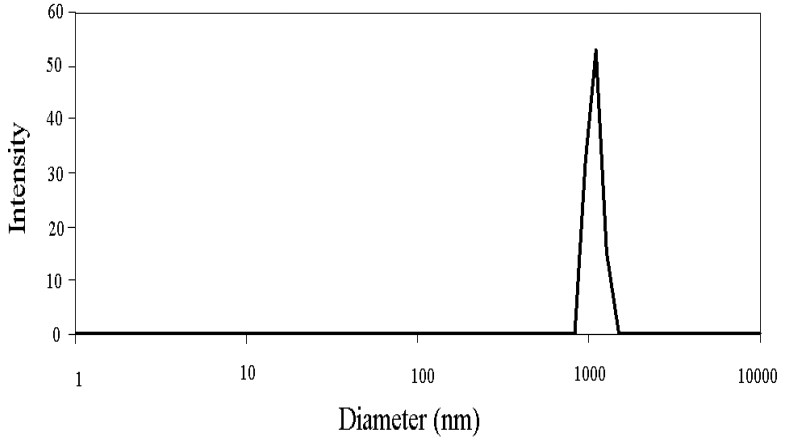

Figure 2.19 DLS of iron oxide aqueous nanoparticles.

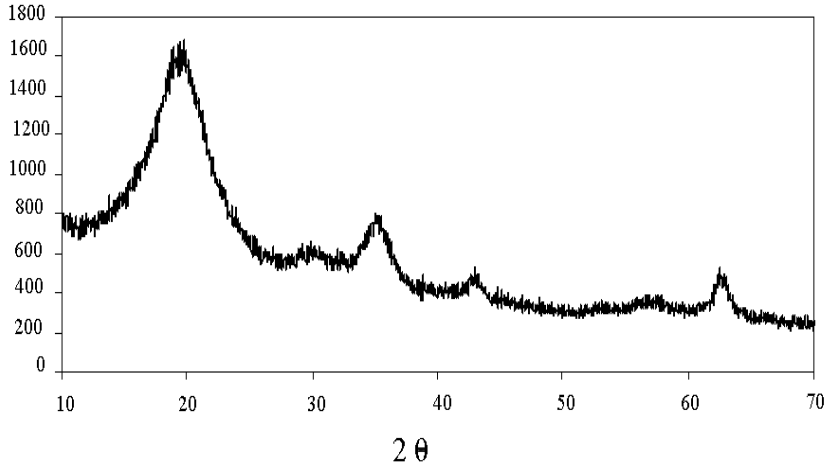

Figure 2.20 DRX of iron oxide aqueous nanoparticles.

To summarize we use Table 2.5 in order to have an easy view of the average size of the samples we employ in next chapters.

Table 2.5: Samples, chapter, and average size of the MNPs

Sample	Chapter	Diameter (nm)
A0	2	11.6
A1	3	5.9
A2	3	9.6
A3	3	13.5
A4	5	5.7
B1	4	~5

2.8 Bibliography

[1] G. Cao. *Nanostructures and Nanomaterials: Synthesis, Properties and Applications*. Imperial College Press London, 2004.

[2] T. Hyeon. Chemical synthesis of magnetic nanoparticles. *Chemical Communications*, 8:927–934, 2003.

[3] D. Caruntu, G. Caruntu, Y. Chen, C. J. O'Connor, G. Goloverda and V. L. Kolesnichenko. Synthesis of variable-sized nanocrystals of Fe_3O_4 with high surface reactivity. *Chemistry of Materials,*16:5527–534, 2004.

[4] N. R. Jana, Y. Chen and X. Peng. Size- and shape-controlled magnetic (Cr, Mn, Fe, Co, Ni) oxide nanocrystals via a simple and general approach. *Chem. Mater*., 16:3931, 2005.

[5] J. Park, E. Lee, N. M. Hwang, M. S. Kang, S. C. Kim, Y. Hwang, J. G. Park, H. J. Noh, J. Y. Kini, J. H. Park and T. Hyeon. One-nanometer-scale size-controlled synthesis of monodisperse magnetic iron oxide nanoparticles. Angewandte Chemie-International Edition, 44:2872–2877, 2005.

[6] J. Rockenberger, E. C. Scher and A. P. Alivisatos. A new nonhydrolytic single-precursor approach to surfactant-capped nanocrystals of transition metal oxides. *Journal of the American Chemical Society,* 121:11595–11596, 1999.

[7] C. B. Murray, S. H. Sun, W. Gaschler, H. Doyle, T. A. Betley and C. R. Kagan. Colloidal synthesis of nanocrystals and nanocrystal superlattices. *Journal of Research and Development*, 45:47–56, 2001.

[8] S. H. Sun, E. E. Fullerton, D. Weller and C. B. Murray. Compositionally controlled FePt nanoparticle materials. IEEE Transactions on Magnetics, 37:1239–1243, 2001.

[9] T. Hyeon, S. S. Lee, J. Park, Y. Chung and H. Bin Na. Synthesis of highly crystalline and monodisperse maghemite nanocrystallites without a size-selection process. *J. Am. Chem. Soc.*, 123:12798–12801, 2001.

[10] S. Sun and H. Zeng. Size-controlled synthesis of magnetite nanoparticles. *J. Am. Chem. Soc.,* 124:8204–8205, 2002.

[11] K. Butter, A.P. Philipse and G.J. Vroege. Synthesis and properties of iron ferrofluids. *Journal of Magnetism and Magnetic Materials*, 252:1–3, 2002.

[12] W. W. Yu, J. C. Falkner, C. T. Yavuz and V. L. Colvin. Synthesis of monodisperse iron oxide nanocrystals by thermal decomposition of iron carboxylate salts. Chemical Communications, 20:2306–2307, 2004.

[13] P. Guardia, N. Perez, A. Labarta, X. Batlle, Controlled synthesis of iron oxide nanoparticles over a wide size range. *Langmuir,* 26:5843–5847, 2010.

[15] F. X. Redl, C. T. Black, G. C. Papaefthymiou, R. L. Sandstrom, M. Yin, H. Zeng, C. B. Murray and S. P. O'Brien. Magnetic, electronic, and structural characterization of

nonstoichiometric iron oxides at the nanoscale. *J. Am. Chem. Soc*., 126:14583–14599, 2004.

[16] J. van Wonterghem, S. Mørup, S. W. Charles and S. Wells. An investigation of the chemical reactions leading to the formation of ultrafine amorphous $Fe_{100-x}c_x$ alloy particles. *J. Colloid Interface Sci*., 121: 558–563, 1988.

[17] M. F. Casula, Y. W. Jun, D. J. Zaziski, E. M. Chan, A. Corrias and A. P. Alivisatos. The concept of delayed nucleation in nanocrystal growth demonstrated for the case of iron oxide nanodisks. *J. Am. Chem. Soc.*, 128:1675–1682, 2006.

[18] C. M. Flynn. Hydrolysis of inorganic iron(III) salts. *Chemical Reviews*, 84:31–41, 1984.

[19] J. Rose, A. Manceau, A. Masion and J. Y. Bottero. Structure and mechanisms of formation of $FeOOH(NO_3)$ oligomers in the early stages of hydrolysis. *Langmuir*, 13:3240–3246, 1997.

[20] E. Matijevic. Preparation and properties of uniform size colloids. Chemistry of Materials, 5:412–426, 1993.

[21] V. K. Lamer and R. H. Dinegar. Theory, production and mechanism of formation of monodispersed hydrosols. Journal of the American Chemical Society 72:4847–4854, 1950.

[22] W. Ostwald. *Lehrbuch der Allgemeinen Chemie*. Leipzig, Germany, 1885.

[23] E. Natividad, M. Castro and A. Mediano. Accurate measurement of the specific absorption rate using a suitable adiabatic magnetothermal setup. *Applied Physics Letters*, 92:093116, 2008.

[24] H. H. Kampinga and E. Dikomey. Hyperthermic radiosensitization: mode of action and clinical relevance. *International Journal of Radiation Biology*, 77:399–408, 2001.

[25] F. Luis, J. M. Torres, L. M. Garcia, J. Bartolome, J. Stankiewicz, F. Petro_, F. Fettar, J. L. Maurice and A. Vaures. Enhancement of the magnetic anisotropy of nanometer-sized Co clusters: Influence of the surface and of interparticle interactions. *Physical Review B,* 65: 094409, 2001.

[26] J. W. Cheon, N. J. Kang, S. M. Lee, J. H. Lee, J. H. Yoon and S. J. Oh. Shape evolution of single-crystalline iron oxide nanocrystals. *Journal of the American Chemical Society*, 126:1950–951, 2004.

[27] R. Rosensweig. Heating magnetic fluid with alternating magnetic field. *Journal of Magnetism and Magnetic Materials*, 252:370–374, 2002.

Chapter 3

Core-Shell ferrofluids for biomedical applications

3.1 Introduction

As it has been pointed out in chapter 1, there is a broad range of applications for magnetic nanoparticles in biology and medicine. Consequently, the structural requirements for each application are also variable. For instance, biotechnological applications such as enzyme carriers, separation, purification, analysis, catalysis and processing need particles with a large size and high magnetic moment [1]. However, *in vivo* applications require a more complex particle structure. That is especially true in the case of magnetic resonance imaging contrast agents targeted drug delivery and cancer therapy [2-4]. Before going into the structural requirements for these applications, let us remind the advantages they may bring. Superparamagnetic nanoparticles (SPN) with respect to usual contrast agents have higher responses necessary to reach single cell detection [5]. Concerning cancer therapy, this technique is already in clinical phase for particles directly injected in the tumour [6], and they will be really useful when they are biologically vectorised so they can reach tumours that, due to their location and/or small size, are currently not accessible by other therapies [7]. In addition, they would avoid most of the undesirable secondary effects associated with radiotherapy and chemotherapy treatments [8]. Moreover, therapy and diagnosis with SPN could be performed simultaneously, thus entering the most promising area of theranostics [9].

Coming back to the structural requirements for *in vivo* applications, the first one is, of course, biocompatibility. Apart from that, there are three important issues to be

considered: 1) optimal magnetic performance, which is obtained when the nanoparticles are monodisperse; 2) high facility to penetrate biological barriers, this requires small hydrodynamic sizes, which in single-core iron oxide nanoparticles (IO) are minimized with a narrow shell; and 3) easy particles functionalization, which requires to have them coated with an adequate reactive surface. This chapter addresses these three issues.

Concerning the first issue, aqueous preparation methods are simple, cheap and, therefore, the favourite for industrial production. However aqueous methods are associated with high size dispersion and interparticle agglomeration that may diminish their magnetic performance. These problems are overcome by organic methods that allow a precise control of the particle size, particle size dispersion and particle agglomeration [10]. The problem with organic methods is that, in order to control the particle growth, they use hydrophobic surfactants. That makes the resulting particles non dispersible in water.

With respect to the second and third issues, the main strategies to coat and redisperse these hydrophobic particles in aqueous media are [11−12]: 1) to attach amphiphilic molecules to the hydrophobic surface [13−14], and 2) to coat the particles with polymeric or silica shells [15−17]. The first approach yields small single-core nanoparticles as desired but the multifunctionalization requires complex chemical processing. The second approach facilitates further multifunctionalization of the particles by means of remnant surface reactive groups in the coating, such as the silanol groups on silica coatings [18−20].

In the following we will consider several chemical routes to obtain aqueous suspensions of functionalized magnetic nanoparticles departing from nanoparticles produced in organic solvents.

3.1.1 Transferring nanoparticles from organic to aqueous media

A summary of typical coating methods used for transferring NPs dispersed in an organic solvent to an aqueous medium is given in Table 3.1.

Table 3.1: Phase transfer routes from organic to aqueous medium for nanoparticles

Type of coating	Chemical route	Example
Carboxylic acid	Oxidation of double bond in oleic acid	O_3 [21], $KMnO_4$ [22]
	Intercalation	Pluronic F-127 [23], PMMA-PEO [24], Tetradecene [15], PEI [24], Cyclodextrine [11]
Polymers	In situ precipitation of nanoparticles in polymer matrixes	Norbornano [25], HOOC-PEG-COOH [26]
	In situ polymerization in the presence of nanoparticles	2-Bromopropionilesther [27]
	Micelle methods	PMAO–PEG [13]
	Particle encapsulation	DSP-PEG-Biotine [28]
Liposomes	Micelle methods	PEG-PE +PC [29]
	Sol-gel	TEOS [30]
Silica	Microemulsion	Silsesquioxano [31]
	Heterogeneous nucleation	Ciclohexane/igepal [32]
Gold	Bridge bifunctional molecule	$HS(CH_2)_{10}COOH$ [33]
	Reduction of Au	$HAuCl_4$ [34]

In the first method, the particle surface is modified from hydrophobic to hydrophilic affinity without removal of the oleic molecules. This is achieved by oxidation of the oleic acid double bond by a strong oxidant, such as $KMnO_4$ or O_3. The oxidation produces the breaking of the double bond and creates a carboxylic group at the end, without affecting the carboxylic group at the other chain end interacting with the iron oxide surface [21, 22]. This method has the advantage that the surface of the IO core is never altered during the process.

When the coating material is a polymer, the stability of the resulting nanoparticles depends on several factors: the ratio between hydrophobic and hydrophilic parts in the polymer chain, the chain length, the anchoring bond, and the polymer conformation. The most popular chemical route for polymer coating is the intercalation of the hydrophobic part of an amphiphilic polymer with the surfactant hydrocarbonous chain [11, 15, 23, 24]. A second route is *in situ* iron oxide precipitation [25, 26] and a third one, *in situ* polymerization, which consists in using monomers as surfactants that are later polymerized to form compact polymer coatings [27]. Besides those, micelle methods based on the use of amphiphilic polymers as surfactants are simple and versatile [13].

An example of nanoparticle encapsulation into liposomes was given by Gopalakhrisnan et al. These authors prepared hybrid vesicles of CdSe quantum dots by dispersing them together with phospholipids that formed the double liposome membrane [28]. The amount of nanoparticles encapsulated inside the liposome can be adjusted by regulating the volume of the organic solvent and the ratio of nanoparticles. Another possibility is to encapsulate nanoparticles in phospholipid block-copolymers micelles. In this way, the formation of single-core nanoparticles can be achieved [29].

Inorganic coatings can also be very effective, especially silica and gold coatings. Gold is an ideal inert material and it is also biocompatible. Besides, gold surfaces can be easily functionalised with macromolecules or any other ligand having a thiol terminal group (-SH). Moreover, it confers optical properties to the material due to superficial plasmons. Gold-IO dimmer structures can be built by epitaxial growth of

magnetite particles on preformed Au nanoparticles [32]. Another strategy is to use bifunctional molecules with a thiol group at one end and a carboxylic group at the other (i.e. 11-mercaptoundecanoic acid) to link both types of particles [33]. The formation of core-shell structures can be achieved by thermal decomposition of gold organic precursors as gold acetate, or by reduction of HAuCl4 in a mixture of water/chloroform/oleilamine in the presence of IO nanoparticles [34].

Silica coatings are very versatile as they allow a control of shell thickness, shell porosity, encapsulation of drugs and other active components, surface functionalization, etc. For this reason they have been the choice in this work.

3.1.2 Use of silanes for particle coating and redispersion in water

Silanes are outstandingly useful materials because as they are organic-inorganic compounds they provide the characteristics of inorganic networks (mechanical and thermal stability) and of organic compounds (hydrophobic/hydrophilic nature or biochemical reactivity) [35, 36]. Besides, silica is biocompatible and inert and the chemistry for the functionalization of silica surfaces is well established, thus opening the way for bioconjugation [17, 18]. The stabilization of silica colloids at pH 7 is realized by electrostatic repulsion because the isoelectric point is in between 3 and 4. Silica coating is usually conducted by hydrolysis of alkoxysilane precursors, such as TEOS, and the most popular procedure is probably the Stöber method [37]. Besides TEOS, a preferred organosilica precursor is APTS that permits to obtain amino functionalized nanoparticles or silsesquioxane (TMA-POSS) [31, 38].

The Stobër method is carried out in water/alcohol medium. A priori, this is unpractical for our purpose because IO@OA particles are not dispersible in this medium. There are several options to overcome this problem: 1) to carry out the hydrolysis in a microemulsion system; 2) to transfer the particles into water after surface modification; 3) a direct coating by hydrolysis of tetraethoxysilane (TEOS) precursor in organic medium; 4) to replace the oleic acid with an organic alkoxysilane precursor by ligand exchange and then perform the hydrolysis of this precursor.

Some of the methods pointed out above may present inconveniences. The first one usually yields multi-core nanoparticles [19, 20]. The second presents several alternatives. One of them uses secondary surfactants, such as cetyltrimethylammonium bromide [38], to transfer the IO@OA nanoparticles to water/ethanol media, and there, they are coated with TEOS. Another alternative is the exchange of the primary surfactant by a hydrophilic ligand containing alkoxysilane groups that can be hydrolysed to form a silica monolayer. Following this approach, Kohler [39] coated IO@OA with poly(ethylene glycol) (PEG) trialkoxisilane in toluene, and Shen et al. [40] coated Pt@Fe_3O_4 core-shell nanoparticles with methoxy-poly(ethylene glycol) silane also in toluene. Then, both of them coated the particles with TEOS in an ethanol/water mixture to obtain Fe_2O_3@MPEG-sil/SiO_2 core-shell nanoparticles that were dispersible in various biological fluids. However, this method may lead to multi-core particles with relatively large sizes (100–200 nm).

The third method may present interparticle gelation problems [41]. On the other hand, the fourth method has been used with success for coating several types of nanoparticles [42]. For instance, Liz-Marzan et al. [43] describe a method for coating gold nanoparticles with silica that uses silane coupling agents as surface primers to render the particle surface able to interact with TEOS. Silane coupling agents act as surface primers providing the nanoparticle surface with silanol groups, and therefore endowing them with chemical affinity for silica. During this first step, the small organic ions initially adsorbed onto the surface are displaced by the coupling agents, which show a larger adsorption affinity. In a second step, sodium silicate solution is added to the dispersion to promote the formation of a thin, dense and relatively homogeneous silica layer around the particles using the silanol groups as anchor points. The particles can then be transferred into ethanol and coated with a silica layer of a controlled thickness by the Stöber process.

3.1.3 Dispersing hydrophobic nanoparticles in water by ligand exchange

A number of ligand exchange methods are classified in Table 3.2. Ligand exchange by bifunctional molecules is a simple process that consists on the

substitution of the surfactant employed in their synthesis by a hydrophilic ligand. Bifunctional molecules have, at least, two functional groups: one that interacts with the nanoparticle surface with strength enough as to displace the surfactant; and another that stabilizes the particles in water usually by electrostatic interactions [12, 45–48].

Table 3.2: Examples of ligand exchange techniques using different ligands

Type of molecule	Example
Bifunctional molecules	DMSA [12], phosphonates [44], citric acid [45], dopamine [46], dendrimers [47], TMAOH [48].
Polymers	PAA-PAH [49], HOOC-PEG-COOH [50].
Silanes	Silane-PEG [39], APTS [38], Thiolsilane [51], Aminosilane [51], Phosphatosilane [52].

Polymers used for ligand exchange contain a carboxylic group that can replace oleic acid. The exchange is carried out in hard conditions (high temperatures and vigorous stirring) because of the slow replacement kinetic of the polymer owing to its large volume [49–50]. The factors determining the stability of the nanoparticles in suspension have already been commented above.

When the purpose is to coat particles with silica it is quite convenient to use exchange ligands having alkoxysilane groups. Several trialkoxysilanes used as exchange ligands by Weller et al. for gold and CdTe nanoparticles are presented in Figure 3.1 [51, 52]. Gold particles were already synthesized in the presence of ligand 1, and CdTe nanoparticles were coated later on by exchange of cysteamine-stabilized CdTe nanoparticles with ligand 1. Then, different silanes (ligands 2, 3, and 4) were condensed on the resulting particle surface, leading to a cross-linked, negatively charged shell.

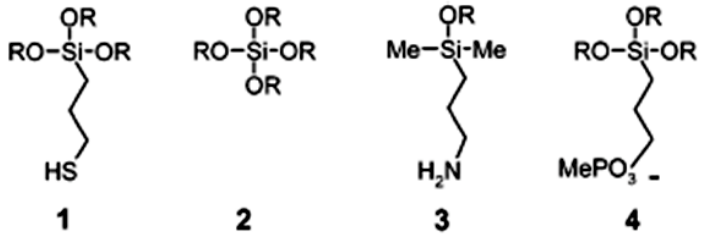

1: R = methyl, 2 and 3: R = ethyl, and 4: R = H.

Figure 3.1 Trialkoxysilanes used by Weller et al.

3.1.4 Our approach for the production of silica coated aqueous dispersions

In this chapter we investigate methods for the production of monodispersed silica coated aqueous dispersions based on the ligand exchange approach. The oleic acid surfactant is exchanged by an organic iron coordinating compound ending in an alkoxysilane group (Figure 3.2). Then, the alkoxysilane precursor layer is hydrolysed in an organic solvent, and the particles are immediately transferred into water to get a stable aqueous dispersion. Finally, the particles are covered with a silica layer by a modified Stöber method.

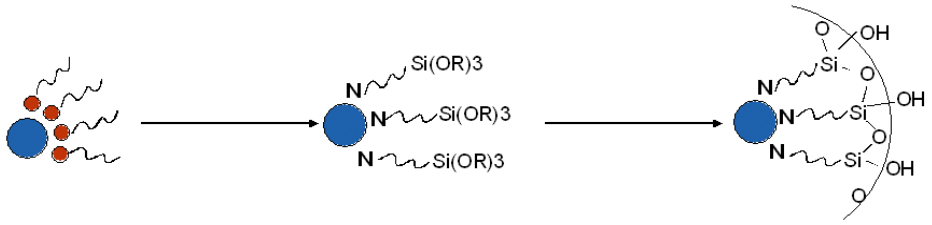

Figure 3.2 Preparation of iron oxide aqueous dispersions.

Two types of ligands have been used: i) commercial short chain organosilanes with a stronger affinity for iron oxide surface than oleic acid, which is the surfactant usually employed in the synthesis of the NPs; and ii) long chain ligands with a molecular structure similar to that of oleic acid. For type i) ligands the following compounds have been selected: 1) diethyl [2-(triethoxysilyl)ethyl]phosphonate

(DTESP); and 2) N-(3-triethoxysilylpropyl)-4, 5-dihydroimidazole (TESDI). For type ii) ligands, there was no commercial choice available. Therefore, we have synthesized the organoalkoxysilane precursor, 3-(triethoxisilyl) propylureido dodecanoic acid (TESPDA), which is structurally similar to oleic acid.

In the first ligand of type i), DTESP (Figure 3.3a), the iron coordinating group is phosphonate and it is separated by an ethylene chain from the trialkoxisilane group. This organophosphorus compound contains a phosphoryl group that may interact efficiently with many metal ions. Besides, the hydrolysis of siloxane group will form an organic-inorganic coating stabilizing the nanoparticles in aqueous medium.

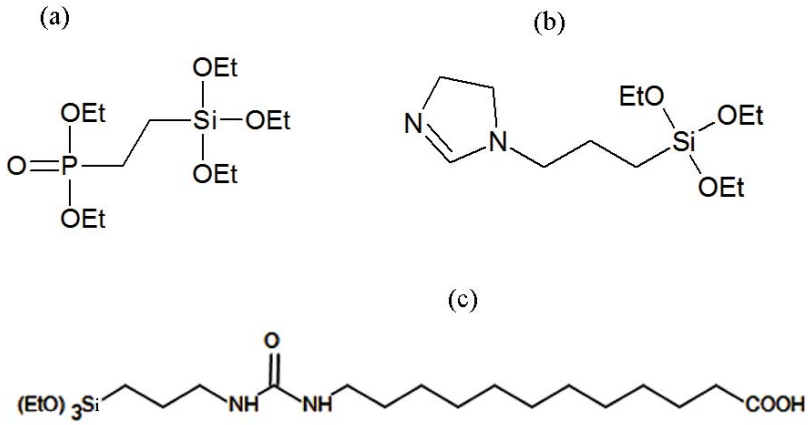

Figure 3.3 Chemical structures of silane precursors: a) diethyl [2-(triethoxysilyl)ethyl]phosphonate (DTESP), b) N-(3-triethoxysilylpropyl)-4,5-dihydroimidazole (TESDI), c) , 3-(triethoxisilyl) propylureido dodecanoic acid (TESPDA).

The second ligand of type i), TESDI (Figure 3.3b), is widely used in the functionalization of mesoporous materials for different applications, i.e. precious metal ions adsorbents, and direct ethanol fuel cells [53, 54]. The coordinating group is imidazole and the spacer is a propyl chain. The imidazole group is also able to interact with metal ions on the particle surface and generate hydrophilic organic-inorganic shells by hydrolysis of the siloxane group.

The ligand of type ii), TESPDA (Figure 3.3c), has a long chain structure and a carboxylic acid ending group. The carboxylic group, as the one in oleic acid, is able to interact with the nanoparticle and, as the other silanes, it has the potential to achieve single core-shell nanoparticles in aqueous dispersion.

3.2 Experimental

3.2.1 Synthesis

Synthesis of IO@OA nanoparticles. Iron oxide nanoparticles coated with oleic acid were prepared following the method proposed by Hyeon as described in chapter 2, samples A1, A2 and A3.

Synthesis of IO@DTESP and IO@TESDI particle aqueous suspensions. 1 ml of IO@oleic acid octyl ether nanoparticle suspension was washed with acetone and dried with Argon for three times. The resulting solid was dispersed in 10 ml of hexane containing 0.1 ml of alkosysilane precursor by sonication and then separated by magnetic decantation and dried with Argon. After repeating this procedure at least once, the solid was redispersed in water to obtain a IO@Silane particle aqueous suspension.

*Synthesis of IO@DTESP@TEOS and IO@TESDI@TEOS particles***.** An amount of IO@silane dried powder sample was dispersed in 4 ml of isopropanol by sonication, then 1 ml of water was added and sonicated for an extra 5 minutes time. After that 300 µl of a NH4OH/ethanol 1:1 mixture were added and sonicated again. Finally, 2.5 ml of the resulting suspension was mixed with 25 ml of isopropanol containing 70 µl of TEOS and stirred for 24 hours.

Synthesis of IO@DTESP@TEOS@Sil-PEG and IO@TESDI@TEOS@Sil-PEG particles. 100 µl of N-(triethoxysililpropyl) O-polyethyleneoxide urethane (Sil-PEG) were added to 15 ml of IO@Silane@TEOS particle suspension and stirred during 24 hours.

Synthesis of TESPDA. The synthesis of TESPDA was carried out by condensation of the amine alkyl carboxylic acid with trialkoxysilane isocyanate by means of urea bridges as represented in scheme 3. In a standard procedure, 2.15 g of 12-aminododecanoic acid (1) were dissolved in a mixture of 8 ml of acetic acid, 16 ml of ethanol, and 16 ml of chloroform, then 2.5 g of 3-cyanobutyltriethoxysilane (2) were added, and the solution was kept under stirring overnight to obtain the alkoxysilane precursor (3).

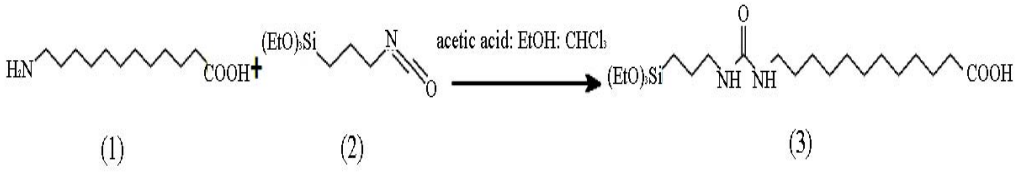

Figure 3.4 Synthesis of the silane precursor.

Synthesis of IO@TESPDA particles. An scheme of the procedure is shown in Fig. 3.4. 10 ml of IO@OA organic suspension were mixed with 0.3 ml of TESPDA and 15 ml of acetone. The resulting nanoparticles were separated with the help of a magnet and the solution was discarded. This operation was repeated twice. Then, the iron oxide nanoparticles were dispersed in 30 ml of hexane during 10 minutes and then treated with 1 ml of alkoxysilane solution. After 15 minutes stirring, 0.1 ml of NH_4OH/ethanol (1:1 by volume) and 0.1 ml of Milli-Q water were added and sonicated during 3 minutes. The sample was well dispersed. Subsequently the sample was magnetically stirred during 4 hours. Then a quantity of 20 ml of Milli-Q water was added. The organic and aqueous phases were easily separated, the aqueous phase containing all the magnetic nanoparticles.

3.2.2 Physical and chemical characterization

The characterization of the materials has been carried out using techniques described in chapter 2. Namely, XRD, TEM, TGA, DLS and SQUID magnetometer.

3.3 Results

3.3.1 Use of short chain organosilanes with iron coordinating groups

3.3.1.1 DTESP

The organic ferrofluid A1, described in chapter 2 has been used for these experiments. The ligand exchange has been performed as described in the experimental section. Figure 3.5 shows the two liquid phases before and after the coating with the phosphate organosilane. It is clear that all the particles passed to the aqueous medium after coating. The colour of the particles becomes lighter due to the silica layer around the black magnetite particles. The aqueous suspension remains stable for several days.

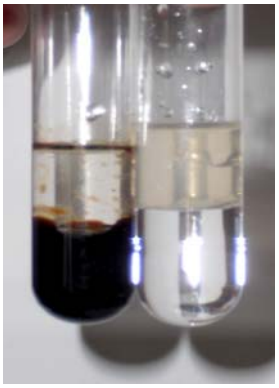

Figure 3.5 Images of the organic and aqueous media before and after ligand exchange.

In Figure 3.6 we can see some TEM micrographs of the sample dispersed in water. The particles seem to be agglomerated in assemblies of different sizes up to 100 nm. The particle size analysis for individual iron oxide nanoparticles yield an average size of 6.2 ± 0.6 nm. A histogram is shown in Figure 3.7. Comparing this size with that of the original organic ferrofluid, D=5.9 ± 1 nm (see sample A1 in chapter 2), we can see that the diameter of the particles has slightly increased after the ligand exchange. Figure 3.8 shows DLS plots of the aqueous suspension. The distribution of hydrodynamic diameters is bimodal with one population with average size D_H=65 nm,

corresponding to small aggregates and a second population with average size D_H=290 nm that corresponds to larger aggregates probably formed by secondary aggregation of the smaller ones. Let's remind that the original ferrofluid had a hydrodynamic size of 11 nm corresponding to individual nanoparticles. Therefore a particle agglomeration has taken place during the coating reaction.

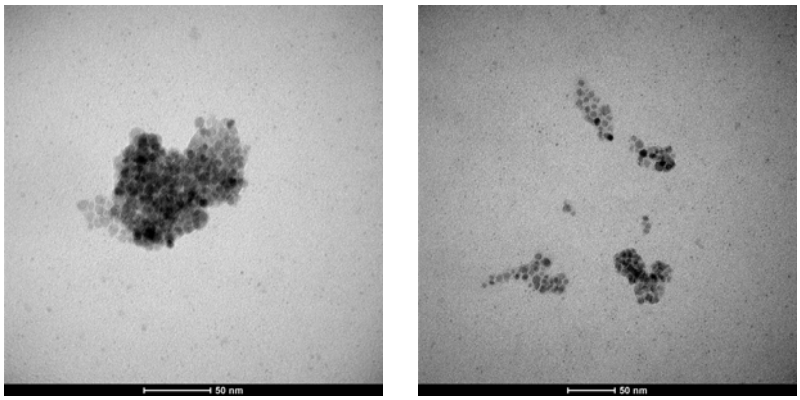

Figure 3.6 TEM micrographs of IO@DTESP nanoparticles.

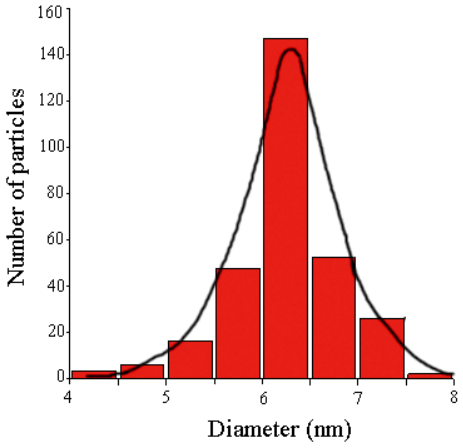

Figure 3.7 Histogram of IO@DTESP nanoparticles.

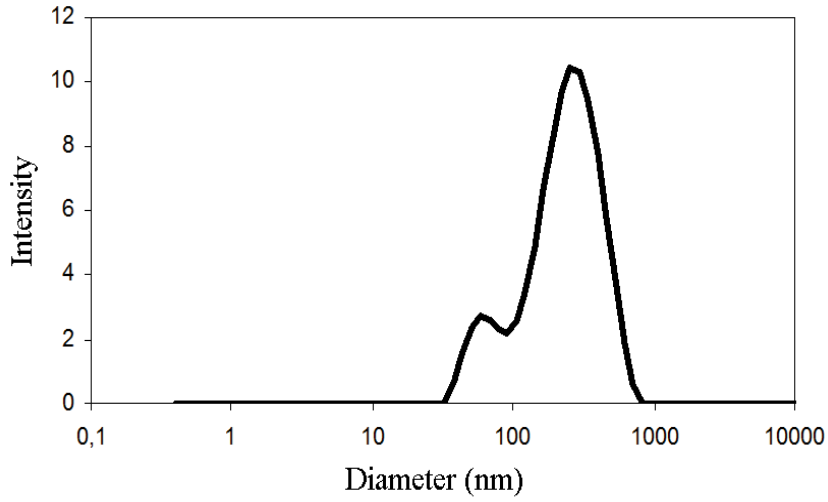

Figure 3.8 DLS of IO@DTESP nanoparticle aqueous suspensions.

In a second stage the IO@DTESP nanoparticles were coated with TEOS. With that purpose, an amount of aqueous suspension of these particles was redispersed in a mixture of isopropanol and water. Then, NH_4OH was added to catalyse the hydrolysis of TEOS on the surface of the silane-stabilized nanoparticles. Figures 3.9 and 3.10 show the corresponding TEM image and DLS plot after the hydrolysis of TEOS. Comparing with TEM results before coating, it is apparent that the layer of lighter material around the aggregates is broader after coating with TEOS indicating the deposition of a new layer of TEOS around the particles. Nevertheless, the DLS peak does not show any significant shift to larger sizes indicating that the average size has not changed too much in comparison with the total particle size. It is also clear from DLS plot that the coating process did not cause any particle aggregation. Aqueous suspensions of IO@DTESP@TEOS were quite stable along the time (Figure 3.11).

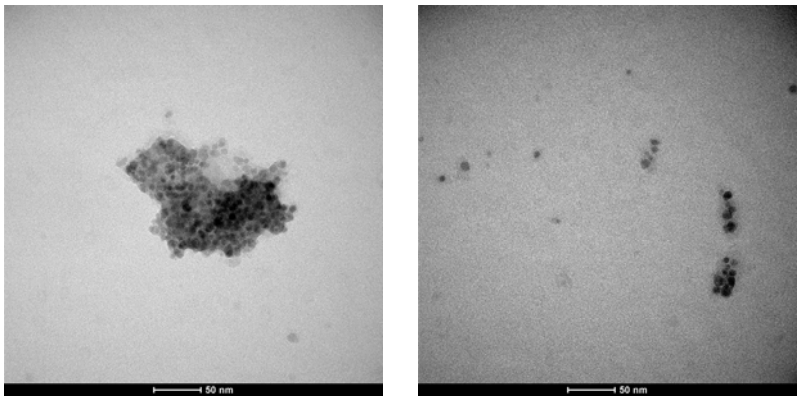

Figure 3.9 TEM micrographs of IO@DTESP@TEOS nanoparticles

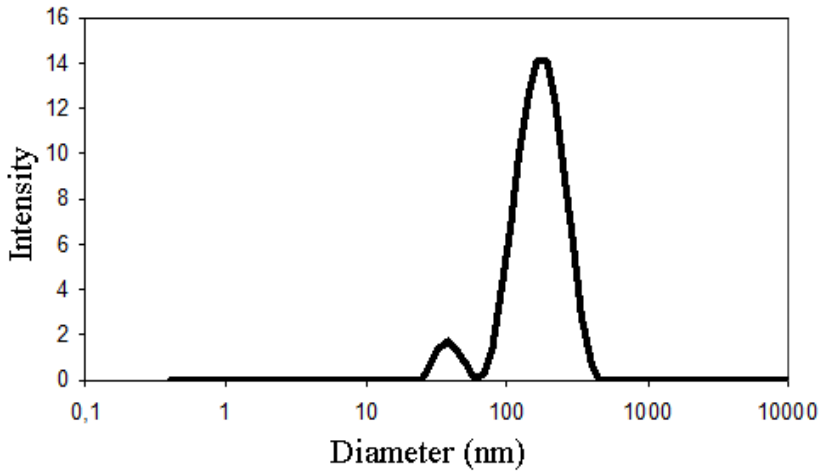

Figure 3.10 DLS of IO@DTESP@TEOS nanoparticle aqueous suspensions.

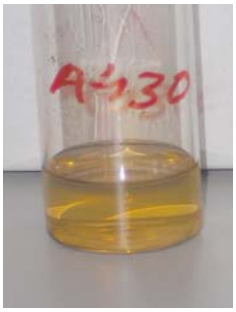

Figure 3.11 Photograph of iron oxide nanoparticles coated with TEOS stabilized in water.

In a last step the IO@DTESP@TEOS nanoparticles were coated with PEG in order to improve their biocompatibility, make then more stable in the blood stream, and make then invisible to macrophages. The choice of PEG for surface coating is founded on its protein anti-adherence properties that make it the preferred polymer coating by far for *in vivo* applications of nanoparticles in general. The anchoring of PEG to the surface was performed by hydrolysis of a PEG trialkoxysilane precursor following the procedure described in the experimental section. The TEM micrographs (Figure 3.12) and DLS plots (Figure 3.13) show that the particles have not experienced important changes during the process. The small size and aqueous stability of the resulting nanoparticle makes them very appropriate for biomedical applications.

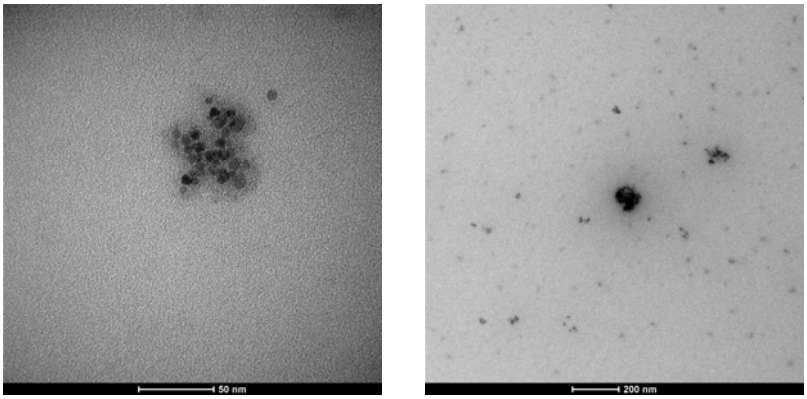

Figure 3.12 TEM micrographs of iron oxide nanoparticles coated with TEOS (left) and Sil-PEG (right).

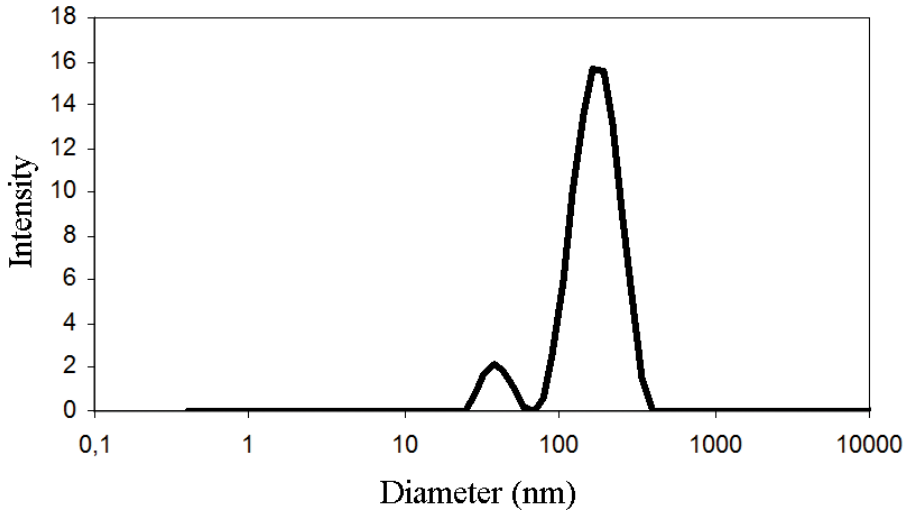

Figure 3.13: DLS of iron oxide nanoparticles coated by TEOS and Sil-PEG.

3.3.1.2 TESDI

The procedure to obtain aqueous suspensions of magnetic nanoparticles using TESDI as ligand exchange organosilane precursor was similar to that used for DTESP. The starting material was with the sample A2, described in chapter 2, with an average diameter of 9.6 ± 1.4 nm. In a first step, the original nanoparticles were dispersed in hexane where the ligand exchange was carried out. Then, the nanoparticles were transferred to water. Figure 3.14 shows the nanoparticle dispersion in water. In a further step, the nanoparticles were coated with TEOS in isopropanol/water media. As it can be appreciated in Figure 3.15, the transferred nanoparticles could be easily dispersed in water with better stability than in the added octyl ether.

Figure 3.14 Photograph of iron oxide nanoparticles suspension after coating with TDESDI in water (right).

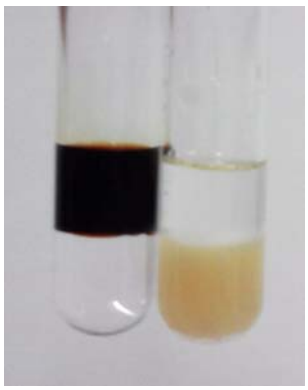

Figure 3.15: Photograph of iron oxide nanoparticles in a two phase octyl ether/water system as prepared (left) and after coating with TEOS (right). Notice that all the silica coated nanoparticles are in the bottom water phase.

In order to study the size, the shape and the state of aggregation of the nanoparticles in the aqueous suspension we analyse them by TEM and DLS. Figure 3.16 shows two TEM micrographs of the sample. The nanoparticles seem to have the same size as the former nanoparticles that is 9.6 nm, and they form aggregates. In Figure 3.17 we can see the histogram of the particle size obtained from TEM micrographs. In the second micrograph we can observe some aggregates produced by nanoparticle agglomeration that are also evident in DLS plots (Figure 3.18).

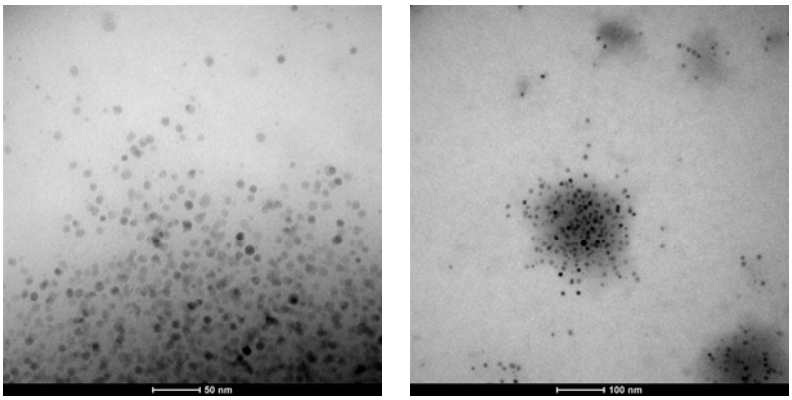

Figure 3.16 TEM micrograph of iron oxide nanoparticles coated with TESDI in water.

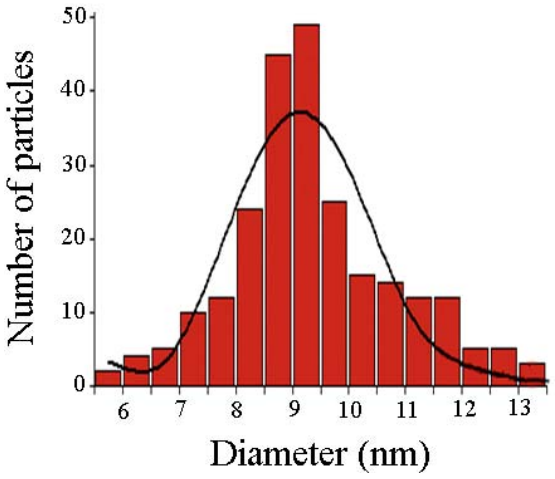

Figure 3.17 Histogram of the particle size distribution.

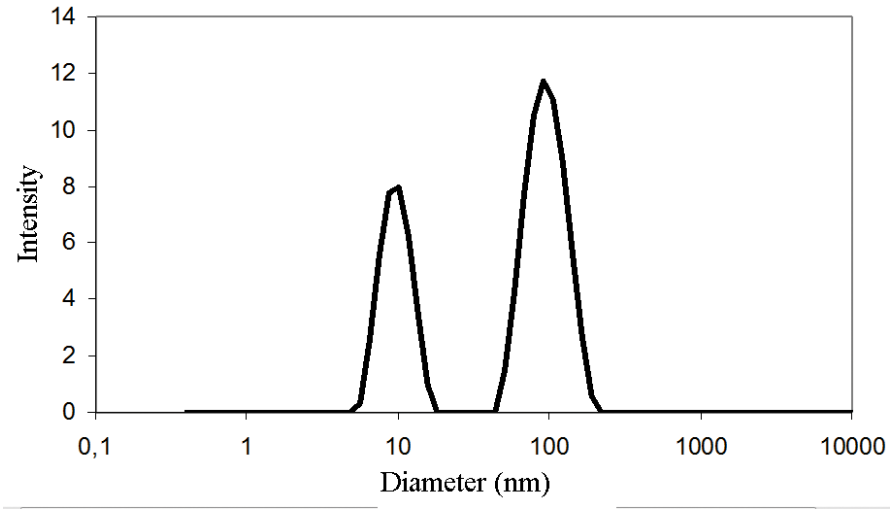

Figure 3.18 DLS of iron oxide nanoparticles stabilized by means of TESDI in water.

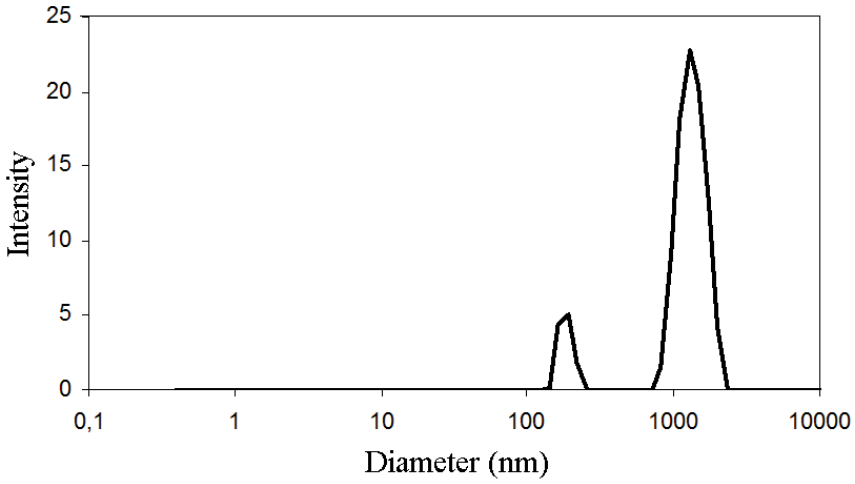

Figure 3.19 DLS of iron oxide nanoparticles stabilized by means of TEOS.

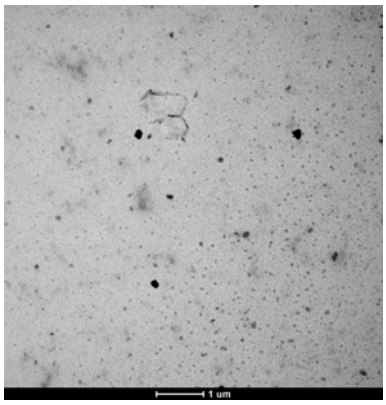

Figure 3.20: TEM micrograph of iron oxide nanoparticles coated with TEOS.

An examination of the suspension by DLS shows the presence of agglomerates (Figure 3.20). That presence is not as abundant as it appears in the plot. As the plot signal corresponds to the intensity of scattered light, large particles scatter proportionally more than small particles. This is reflected on TEM images (Figure 3.19) that shows that the ratio of agglomerates in number is relatively low.

3.3.2 Use of long chain organosilanes with iron coordinating groups, TESPDA

The third approach to obtain single–core aqueous stable nanoparticles has been based on the use of exchange organosilane ligands with long hydrocarbon chains, such as TESPDA. In this case, the starting organic ferrofluid was sample A3 described in chapter 2. Aqueous dispersions of iron oxide nanoparticles coated with an organosilica layer IO@silane were prepared according to the procedure described in the experimental section. First, sample A3 powders were precipitated with acetone and redispersed in a solution of the alkoxysilane precursor in hexane by ultrasounds. Then, the hydrolysis of the alkoxysilane precursor was carried out by addition of water and ammonia. After addition of an aqueous phase and stirring, all the particles passed to the aqueous phase as shown in Figure 3.21. In order to obtain an individual coating of the particles it is necessary to perform the ligand substitution by successive steps of dispersion and reprecipitation in acetone/alkoxysilane mixtures. In the absence of this

procedure the resulting particles were dispersible in water but they showed intense aggregation as observed by TEM and DLS (data not shown).

Figure 3.21 Left: IO@AO nanoparticles in organic medium. Right: IO@TESPDA nanoparticles in aqueous medium.

The characteristics of the aqueous dispersion sample are shown in the next figures. A TEM image of the IO@silane sample is shown in Figure 3.22. It is clear from the image that the particles are also rounded and uniform in size. Although the silica shell was hard to distinguish in most cases due to the low contrast, it was occasionally observed in some particles. The inset in Figure 3.22 shows a particle with a dark nucleus of 14.6 nm in diameter surrounded by a layer with a 6.0 nm in thickness. Histogram and Gaussian fitting of the particle size distribution is shown in Figure 3.23. The estimated mean diameter was 13.5 nm, and the standard deviation was 3 nm, thus very similar to those of the as prepared sample. However, a DLS analysis of the aqueous suspension (Figure 3.24) yields an average hydrodynamic diameter of 20 nm, which is 9 nm larger than that of the organic dispersion. This diameter is in accordance with the TEM size of particle in Figure 3.22 that is 20.6 nm. It is well known that compounds that mainly consist in hydrocarbonous structures have low contrast in TEM images. Analysis by EDX (Figure 3.25) confirms the presence of Fe and Si in the sample. The Cu and Cr signals appearing in the spectrum come from the grid and the sample holder, respectively.

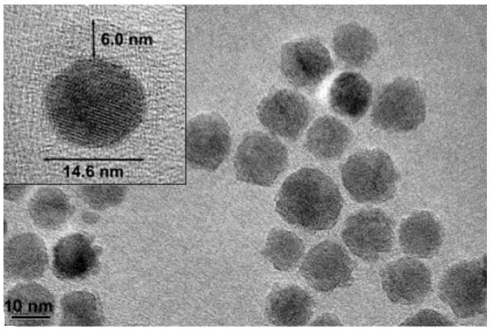

Figure 3.22 TEM image of IO@silane particles. In the insert HRTEM image of a particle surrounded by a halo with a thickness of 6 nm.

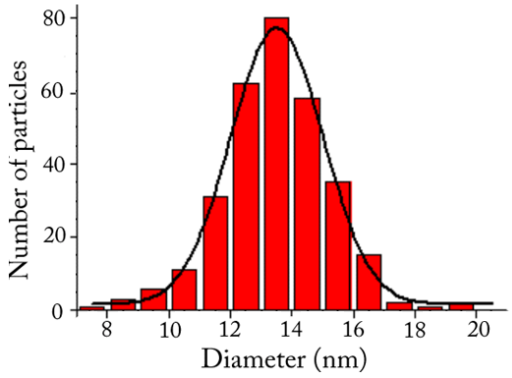

Figure 3.23 Histogram of the particle size distribution.

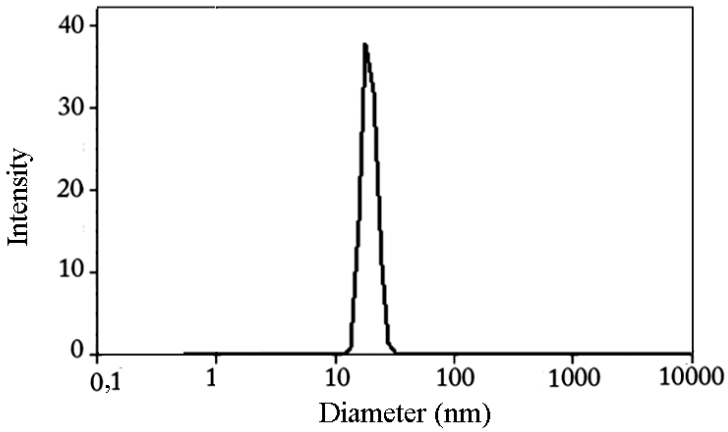

Figure 3.24 DLS of IO@silane in aqueous medium.

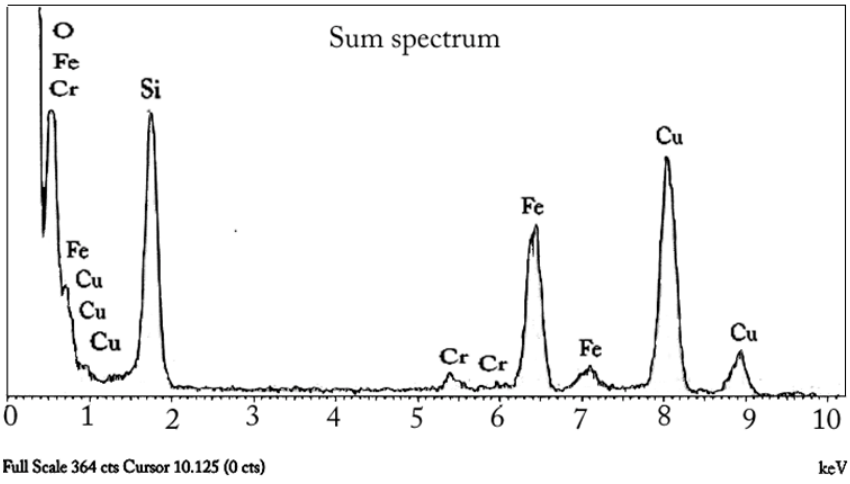

Figure 3.25 EDX spectrum of the IO@silane sample.

The resulting nanoparticles are single-core, have a small hydrodynamic diameter, 20 nm, and no agglomeration is observed. This new procedure opens multiple possibilities for an easy functionalization of the particles because of the large array of trialkoxide precursors available, including luminescent dyes, and anchoring groups for drugs, antibodies and other biological functionalities.

3.3.2.1 Magnetic Properties

The three most important magnetic parameters of SPN for most biomedical applications are: saturation magnetization, M_S, important for separation, purification, processing and targeted drug delivery, magnetic anisotropy, K, important for MRI and out-of-phase ac susceptibility, χ'', important for hyperthermia. In order to determine the values of these parameters in our ferrofluids, we have measured the variation of the magnetization with a field, and the variation of the ac susceptibility with the temperature, in both organic and aqueous dispersions. $M_S(H)$ plots are shown if Figure 3.26 after subtracting the contribution from the fluid and the silica sample holder. The shape of the curves is very similar in both cases, but there is a difference of scale that may be due to surface effects from different coatings or to uncertainties in the determination of iron concentration in the aqueous dispersion due to an incomplete

dissolution of the particles. The curves do not reach saturation; instead they show a region of linear increase of the magnetization with the field that is typical in maghemite particles in the nanometre size range. The curves have been fitted to a modified Langevin function:

$$M = M_S L\left(\frac{\mu H}{k_B T}\right) + \chi H \qquad (1)$$

where M_S is the saturation magnetization and μ is the average magnetic moment of the core. The linear contribution to the magnetization, χH, is an additional term that is often used for antiferromagnetic and ferromagnetic nanoparticles [55, 56]. The fits yield values of 43.3 and 38.6 emu/g(Fe_2O_3) for, respectively, the organic and aqueous dispersions. These values are lower than the bulk value (76 emu/g(Fe_2O_3)), as expected for particles of their size. The M_S decrease in nanoparticles has been attributed to a "magnetically death layer" with a thickness that have been estimated in 1 nm [57]. A fitting to eq. 2 in ref [55] yields a thickness of 1.07 nm for the organic sample and 1.29 nm for the aqueous dispersion, which are in good agreement with the referred model.

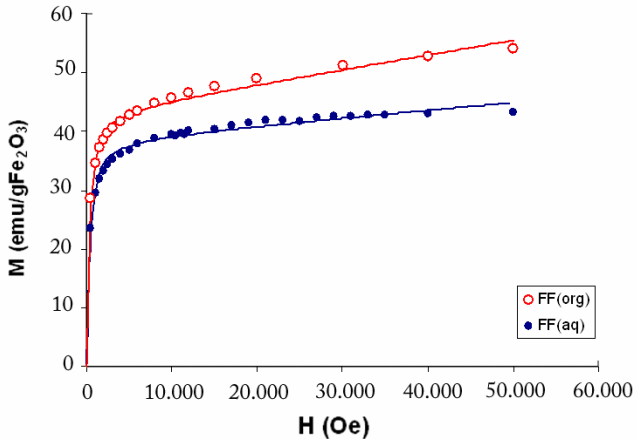

Figure 3.26 Variation of the magnetization with the magnetic field for organic and aqueous dispersions.

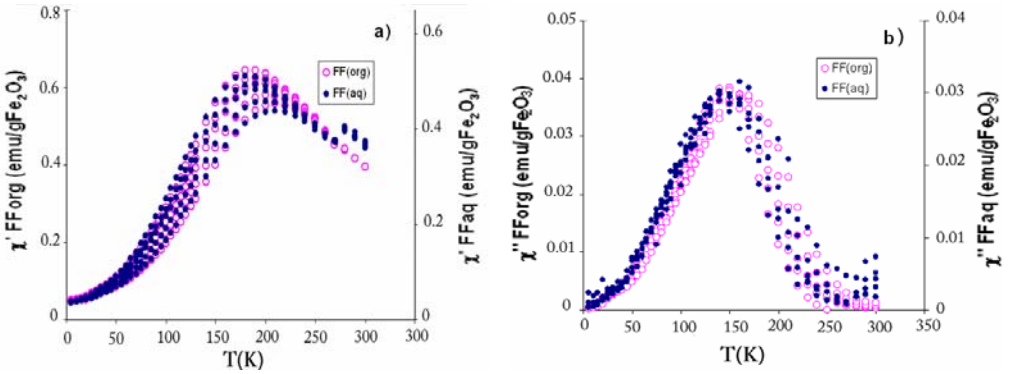

Figure 3.27 Variation of the in-phase (a) and out-of-phase (b) ac magnetic susceptibility with the temperature for organic and aqueous dispersions, at several frequencies of the alternating field (1 Hz, 5 Hz, 15 Hz, 117 Hz and 852 Hz).

AC measurements are presented in Figure 3.27. The data correspond well to superparamagnetic behaviour, as expected for 13.5 nm maghemite particles. Again, as in the case of *M(H)* data, there is a difference of scale between the organic and the aqueous dispersions. The scaling factor is very similar in both cases. It is known that magnetic properties of nanoparticles are very sensitive to surface binding state [58]. Actually, it has already been found in magnetite nanoparticles that an increase on the thickness of the coating layer causes a decrease of the magnetization with slight changes in the blocking temperature [59], as it is observed here. Once re-scaled, the data from both dispersions are similar for temperatures below the freezing temperature (around 270 K). Therefore, the Néel relaxation behaviour of the particles is hardly changing in the process of hydrophilization. A detailed analysis of the data within the Néel theory of relaxation yields blocking temperatures, at 117 Hz, of $T_B(FF_{org})$ = 160 K and $T_B(FF_{aq})$ = 150.7 K, time relaxation constants of $-\log\tau_0(FF_{org})$ = 24,6 and $-\log\tau_0(FF_{aq})$ = 21,1, and effective anisotropy constants $K_{eff}(FF_{org}) = 3{,}8\cdot10^5$ erg/cm^3 and $K_{eff}(FF_{aq}) = 3{,}1\cdot10^5$ erg/cm^3. Thus, the analysis reveals some difference between organic and aqueous suspensions: T_B decreases slightly, τ_0 increases, and U decreases.

Above the freezing temperature, there is a sudden susceptibility increase, particularly in χ', in the case of aqueous dispersion that is absent in the organic dispersion. This increase can be attributed to the onset of Brown relaxation that is not appearing in the organic dispersion. Thus, contrary to the case of Néel relaxation, Brown relaxation is indeed affected by the dispersing medium. The Brownian relaxation time can be expressed as:

$$\tau_{\mathrm{B}} = \left(\frac{3\eta V_{hyd}}{K_B T} \right) \tag{2}$$

where η is the viscosity of the medium, and V_{hyd} is the hydrodynamic volume, respectively. Thus, the differences of intensity must be related to differences of the solvent viscosity that hinder the rotation of the particles in the organic medium with respect to water. This can be of considerable importance for magnetothermic applications.

3.4 Conclusions

Phase transfer of iron oxide nanoparticles from organic to aqueous solvents has been achieved by ligand exchange of oleic acid with three different organoalkoxysilanes. The shape and size of the original nanoparticles are maintained after the phase-transfer process in all cases. The diethylphosphatoethyltriethoxysilane ligand yielded stable aqueous dispersions, but the resulting particles were agglomerated to some extent. The N-(3-triethoxysilylpropyl)-4,5-dihydroimidazole ligand presented similar results but with a lower degree of agglomeration was lower, so thatthe quantity of single-core nanoparticles was substantially increased. This can be due to the interactions between the iron oxide and the silanes functional groups. As the phosphate group interacts weaker than the imidazole with the iron oxide nanoparticle, the concentration of free silane increases and condense forming agglomerates. In both cases the single-core particles can be isolated from the agglomerated particles by filtration, magnetic separation or centrifugation.

Alternatively, by means of 3-(triethoxisilyl) propylureido dodecanoic acid, we have described a straightforward procedure to transfer high quality iron oxide nanoparticles synthesized in organic medium into aqueous medium forming single core-shell nanoparticle suspensions. The phase transfer is more

efficient than in the methods described before, probably due to the fact that the long chain permits a better ordered disposition of ligands around the the nanoparticles. The aqueous magnetic nanoparticles maintain the shape, crystallinity and size distribution of the original organic nanoparticles, as well as with short chain ligands. The magnetic studies of organic and aqueous ferrofluids are consistent with the superparamagnetic behaviour of the nanoparticles.

To summarize we can conclude that the first two ligand exchange procedures employing two short chain commercial silanes permit to obtain stable aqueous suspensions of iron oxide nanoparticles. The phosphateligand, produces agglomerates and the imidazol ligand a mixture of single-core nanoparticles and agglomerated nanoparticles. The main drawback of these procedures is is a low yield. The ferrofluids obtained in these ways can be useful in biomedical applications after separation of aggregates by filtration, magnetic separation or centrifugation. In the third procedure, using a long chain ligand, the transfer from organic to aqueous medium is more effective, and it yields single-core aqueous suspensions, which was one of the purposes of this work. Besides, the resulting nanoparticles can be further coated with a silica layer that can be easily functionalized by hydrolysis of biofunctional molecules having alkoxysilane groups. Therefore these methodology can be very useful for the production of multifunctional biomedical magnetic nanoparticle suspensions.

3.5 Bibliography

[1] O. Kreft, M. Prevot, H. Möhwald, and G. B. Sukhorukov. Shell-in-shell microcapsules: a novel tool for integrated, spatially confined enzymatic reactions. *Angew. Chem. Int. Ed*., 46:5605–5608, 2007.

[2] Y. W. Jun, J. H. Lee and J. Cheon. Chemical design of nanoparticle probes for high-performance magnetic resonance Imaging. *Angew. Chem. Int. Ed*., 47:5122 – 5135, 2008.

[3] H. B. Na, I. C. Song andT. Hyeon. Inorganic nanoparticles for MRI contrast agents. *Adv. Mater*., 21:2133–2148, 2009.

[4] R. Weissleder, A. Moore, U. Mahmood, R. Bhorade, H. Benveniste, E. A. Chiocca and J. P. Basilion. In vivo magnetic resonance imaging of transgene expresión. *Nat. Med*., 6:151–154 2000.

[5] A. Jordan, R. Scholz, K. Maier-Hauff, M. Johannsen, P. Wust, J. Nadobny, H. Schirra, H. Schmidt, S. Deger and S. Loening. Presentation of a new magnetic field therapy system for the treatment of human solid tumors with magnetic fluid hyperthermia. *J. Magn. Magn. Mater*., 225:118–126, 2001.

[6] M. Johannsen, U. Gneveckow, L. Eckelt, A. Feussner, N. Waldoefner, R. Scholz, S. Deger, P. Wust, S. Loening and A. Jordan. Clinical hyperthermia of prostate cancer using magnetic nanoparticles: presentation of a new interstitial technique. Int J Hyperther, 21:637–647, 2005.

[7] Q. A. Pankhurst, N. K. T. Thanh, S. K. Jones and J. Dobson. Progress in applications of magnetic nanoparticles in biomedicine. *J. Phys. D: Appl. Phys*. 42:224001, 2009.

[8] V. Ozdemir, B. Williams-Jones, S. J. Glatt, M. T. Tsuang, J. B. Lohr and C. Reist. Shifting emphasis from pharmacogenomics to theragnostics. *Nature Biotech*., 24:942–946, 2006.

[9] S. G. Kwon, Y. Piao, J. Park, S. Angappane, Y. Jo, N.-M. Hwang, J.-G. Park and T. Hyeon. Kinetics of monodisperse iron oxide nanocrystal formation by "heating-up" process. *J. Am. Chem. Soc*., 129:12571–12584, 2007.

[10] T. Hyeon, S. S. Lee, J. Park, Y. Chung and H. B. Na. Synthesis of highly crystalline and monodisperse maghemite nanocrystallites without a size-selection process. J. Am. Chem. Soc., 123:12798–12801, 2001.

[11] Y. Wang, J. Feng Wong, X. Teng, X. Z. Lin, and H. Yang. "Pulling" nanoparticles into water:phase transfer oleic acid stabilized monodisperse nanoparticles unto aqueous solutions of cyclodextrin. *Nano Lett*., 3: 1555–1559, 2003.

[12] Y. Jun, Y. M. Huh, J. Choi, J. H. Lee, H. T. Song, S. Kim, S. Yoon, K. S. Kim, J. S. Shin, J. S. Suh and J. Cheon. One-step synthesis of core(Cr)/shell(γ-Fe_2O_3) nanoparticles. *J. Am. Chem. Soc*., 127:5732–5733, 2005.

[13] W. W. Yu, E. Chang, C. M. Sayes, R. Drezek and V. L Colvin. Aqueous dispersion of monodisperse magnetic iron oxide nanocrystals through phase transfer. *Nanotech*., 17:4483–4487, 2006.

[14] T. Zhang, J. Ge, Y. Hu and Y. Yin. A General Approach for Transferring Hydrophobic Nanocrystals into Water. *Nano Lett.,* 7:3203–3207, 2007.

[15] T. Pellegrino, L. Manna, S. Kudera, T. Liedl, D. Koktysh, A. L. Rogach, S. Keller, J. Raedler, G. Natile and W. J. Parak. Hydrophobic nanocrystals coated with an amphiphilic polymer shell: a general route to water soluble nanocrystals. *Nano Lett*., 4:703–707, 2004.

[16] U. Jeong, X. Teng, Y. Wang, H. Yang and Y. Xia. Superparamagnetic colloids: controlled synthesis and niche applications . *Adv. Mater*., 19:33–60, 2007.

[17] Y. Piao, A. Burns, J. Kim, U. Wiesner and T. Hyeon. Designed fabrication of silica-based nanostructured particle systems for nanomedicine applications. *Adv. Funct. Mater*., 18:3745–3758, 2008.

[18] M. Liong, J. Lu, M. Kovochich, T. Xia, S. G. Ruehm, A. E. Nel, F. Tamanoi and J. I. Zink. Multifunctional inorganic nanoparticles for imaging, targeting, and drug delivery. *ACS Nano*, 2:889–896, 2008.

[19] D.C. Lee, F.V. Mikulec, J.M. Pelaez, B. Koo and B.A. Korgel. Synthesis and Magnetic Properties of Silica-Coated FePt Nanocrystals. *J. Phys. Chem. B,* 110:11160–11166, 2006.

[20] A. T. Heitsch, D. K. Smith, R. N. Patel, D. Ress and B. A. Korgel. Multifunctional particles: Magnetic nanocrystals and gold nanorods coated with fluorescent dye-doped silica shells. *J. Solid State Chem.,* 181:1590–1599, 2008.

[21] S. Y. Lee and M. T. Harris. Surface modification of magnetic nanoparticles capped by oleic acids: Characterization and colloidal stability in polar solvents. *Journal of Colloid and Interface Science*, 293:401–408, 2006.

[22] F. Herranz, M. P. Morales, A. G. Roca, M. Desco and J. Ruiz-Cabello. A new method for the rapid synthesis of water stable superparamagnetic nanoparticles. *Chemistry: A European Journal,* 3:215–222, 2008.

[23] T. K. Jain, M. A. Morales, S. K. Sahoo, D. L. Leslie-Pelecky and V. Labhasetwar. Iron oxide nanoparticles for sustained delivery of anticancer agents. *Molecular Pharmaceutics*, 2:194–205, 2005.

[24] A. M. Smith, H. Duan, M. N. Rhyner, G. Ruan and S. Nie, S. A systematic examination of surface coatings on the optical and chemical properties of semiconductor quantum dots. *Physical Chemistry Chemical Physics*, 8:3895–3903, 2006.

[25] K. D. Belfield and Li, Z. Norbornene-functionalized diblock copolymers via ring-opening metathesis polymerization for magnetic nanoparticle stabilization. *Chemistry of Materials*, 18:5929–5936, 2006.

[26] F. Hu, L. Wei, Z. Zhou, Y. Ran, Z. Li and M. Gao. Preparation of Biocompatible Magnetite Nanocrystals for In Vivo Magnetic Resonance Detection of Cancer. *Advanced Materials,* 18:2553–2556, 2006.

[27] S. Gravano, R. Dumas, K. Liu and T. E. Patten. Methods for the surface punctionalization of γ-Fe_20_3 nanoparticles with initiators for atom transfer radical polymerization and the formation of core-shell inorganic-polymer structures. *Journal of Polymer Science: Part A: Polymer Chemistry,* 43:3675–3688, 2005.

[28] G. Gopalakrishnan, C. Danelon, P. Izewska, M. Prummer, P.Y. Bolinger, I. Geissbuhler, D. Demurtas, J. Dubochet and H. Voge. Multifunctional lipid/quantum dot hybrid nanocontainers for controlled targeting of live cells. *Agewante Chemie International Ed*., 45:5478–5483, 2006.

[29] B. Dubertret, P. Skourides, D. J. Norris, V. Noireaux, A. Brivanlou and A. Libchaber. In Vivo Imaging of Quantum Dots Encapsulated in Phospholipid Micelles. *Science*, 298:1759–1762, 2002.

[30] M. Aslam, L. Fu, S. Li and V. P. Dravid. Silica encapsulation and magnetic properties of PePt nanoparticles. *Journal of Colloid and Interface Science*, 2005, 290, (2), 444–449, 2005.

[31] B. L. Frankamp, N. O. Fischer, R. Hong, S. Srivastava and V. M. Rotello. Surface modification using cubic silsesquioxane ligands. Facile synthesis of water metal oxide nanoparticles*. Chem. Mater*., 18:956–959, 2006.

[32] M. Zhang, B. Cushing and C. O'Connor. Synthesis and characterization of monodisperse ultra-thin silica-coated magnetic nanoparticles. *Nanotechnology*, 19:085601, 2008.

[33] J. Lim, R. D. Tilton, A. Eggeman and S. Majetich. Design and synthesis of plasmonic magnetic nanoparticles. *Journal of Magnetism and Magnetic Materials,* 311:78–83, 2007.

[34] J. S. Choi, Y. W. Jun, S. Yeon, H. Kim, J. S. Shin and J. W. Cheon. Biocompatible hetero-structured nanoparticles for multimodal biological detection. *Journal of the American Chemical Society,* 128:15982–15983, 2006.

[35] H. Schmidt. New type of non-crystalline solids between inorganic and organic materials. *J. Non-Cryst. Solids*, 73:681–691, 1985.

[36] C. Sanchez and F. Ribot. Design of hybrid organic-inorganic materials synthesized by sol-gel chemistry. *New J. Chem.,* 18(10) 1007–1048, 1994.

[37] W. Stöber, A. Fink and E. Bohn. Controlled growth of monodisperse silica spheres in micron size range. *Journal of Colloid and Interface Science*, 26:62–69, 1968.

[38] J. Kim, J. E. Lee, J. Lee, J. H. Yu, B. C. Kim, K. An, Y. Hwang, J. G. Park, J. Kim. and T. Hyeon. Magnetic fluorescent delivery vehicle using uniform mesoporous silica spheres embedded with monodisperse magnetic and semiconductor nanocrystals. *J. Am. Chem. Soc.,* 128:688–, 2006.

[39] N. Kohler, G. E. Fryxell and M. Zhang. A bifunctional poly(ethylene glycol) silane immobilized on metallic oxide-based nanoparticles for conjugation with cell targeting agents**.** *J. Am. Chern. Soc.,* 126:7206–7211, 2004.

[40] R. Shen, P. H. C. Camargo, Y. Xia and H. Yang. Silane-based poly(ethylene glycol) as a primer for surface modification of nonhydrolytically synthesized nanoparticles using the Stöber method. *Langmuir*, 24:11189–11195, 2008.

[41] K. Woo, J. Hong and J. P. Ahn. Synthesis and surface modification of hydrophobic magnetite to processible magnetite@silica-propylamine. *J. Magn. Magn. Mater.*, 293:177–181, 2005.

[42] M. I. Shukoor, F. Natalio, H. A. Therese, M. N. Tahir, V. Ksenofontov, M. Panthöfer, M. Eberhardt, P. Theato, H. C. Schröder, W. E. G. Müller and W. Tremel. Fabrication of a silica coating on magnetic γ-Fe_2O_3 nanoparticles by an immobilized enzyme. *Chem. Mater.*, 20:3567–3573, 2008.

[43] Liz-Marzan, LM, Giersig M and Mulvaney P. Synthesis of nanosized gold−silica core−shell particles. Langmuir, 12:4329–4335, 1996.

[44] D. B. Robinson, H. J. Persson, H. Zeng, G. Li, N. Pourmand, S. Sun and S.X. Wang. DNA-functionalized MFe_2O_4 (M=Fe, Co or Mn) nanoparticles and their hybridization to DNA-functionalized surfaces. *Langmuir,* 21:3096–3103, 2005.

[45] E. Taboada, E. Rodriguez, A. Roig, J. Oro, A. Roch and R. N. Muller. Relaxometric and Magnetic Characterization of Ultrasmall Iron Oxide Nanoparticles with High Magnetization. Evaluation as Potential T_1 Magnetic Resonance Imaging Contrast Agents for Molecular Imaging. *Langmuir*, 23:4583–4588, 2007.

[46] C. Xu, K. Xu, H. Gu, R. Zheng, H. Liu, X. Zhang, Z. Guo and B. Xu. Dopamine as A Robust Anchor to Immobilize Functional Molecules on the Iron Oxide Shell of Magnetic Nanoparticles. *J. Am. Chem. Soc.,* 126:9938–9939, 2004.

[47] C. Duanmu, I. Saha, Y. Zheng, B. M. Goodson and Y. Gao. Dendron-functionalized superparamagnetic nanoparticles with switchable solubility in organic and aqueous media: matrices for homogeneous catalysis and potential MRI contrast agents. *Chemistry of Materials,* 18:5973–5981, 2006.

[48] V. Salgueriño-Maceira, L. M. Liz-Marzán and M. Farle. Water-Based Ferrofluids from Fe_xPt_{1-x} Nanoparticles Synthesized in Organic Media. Lagmuir, 20:6946–6950, 2004.

[49] T. Zhang, J. Ge, Y. Hu and Y. Yin. A general approach for transferring hydrophobic nanocrystals into water. *Nano Letters*, 7 (10) 3203-3207, 2007.

[50] J. Xie, C. Xu, N. Kholer, Y. Hou and S. Sun. Controlled PEGylation of monodisperse Fe_3O_4 nanoparticles for reduced non-specific uptake by macrophage cells. *Advanced Materials*, 19:3163–3166, 2006.

[51] A. Schroedter and H. Weller. Ligand design and bioconjugation of colloidal gold nanoparticles. *Angew. Chem. Int. Ed.,* 41:3218–3221, 2002.

[52] A. Schroedter, H. Weller, R. Eritja, W. E. Ford and J. M. Wessels. Biofunctionalization of silica-coated CdTe and gold nanocrystals. *Nano Lett*., 2:1363–1367, 2002.

[53] T. Kang Y. Park, K. Choi, J. Sang and J. Yi. Ordered mesoporous silica (SBA-15) derivatized with imidazole-containing functionalities as a selective adsorbent of precious metal ions. Journal of Materials Chemistry, 14**:**1043**–**1049**,** 2004.

[54] K. S. Roelofs, H. Thomas and S. Thomas. Dihydrogenimidazole modified silica-sulfonated poly(ether ether ketone) hybrid materials as electrolyte membranes for direct ethanol fuel cells. *Materials Science and Engineering B*, 176:727**–**735**,** 2011.

[55] S.H. Kilcoyne and R. Cywinski. Ferritin: A model superparamagnet. *J. Magn. Magn. Mater*., 140–144:1466–1467, 1995.

[56] B. Martinez, A. Roig, X. Obradors, E. Molins, A. Rouanet and C. Monty. Magnetic properties of γ-Fe2O3 nanoparticles obtained by vaporization condensation in a solar furnace. *J. Appl. Phys.,* 79:2580–2587, 1996.

[57] A. Millan, A. Urtizberea, N. J. O. Silva, F. Palacio, V. S. Amaral, E. Snoeck and V. Serin. Surface effects in maghemite nanoparticles. *J. Magn. Magn. Mater.,* 312:L5–L9, 2007.

[58] E. Tronc, A. Ezzir, R. Cherkaoui, C. ChaneHac, M. Nogués, H. Kachkachi, D. Fiorani, A.M. Testa, J.M. Grenèche and J.P. Jolivet. Surface-related properties of γ-Fe_2O_3 nanoparticles. *J. Magn. Magn. Mater.,* 221:63–79, 2000.

[59] L. Fu, V.P. Dravid and D.L Johnson. Self-assembled (SA) bilayer molecular coating on magnetic nanoparticles. *Appl. Surf. Sci.,* 181:173-178, 2001.

Chapter 4

Superparamagnetic beads for a biosensor

4.1 Introduction

Nanoparticulate materials have risen great interest in the last decades, particularly after new specific characterization techniques and synthetic procedures allowing the study of their unique properties became available. It is well known that materials at the nanometric scale can present qualitatively different behaviour than their analogous materials in bulk do not show. In this sense, nanoparticulate magnetic materials are a clear example. The novel physical properties these materials exhibit can be exploited in many and interesting applications and can be used in fields such as information storage, environmental decontamination, cooling fluids, inks, lubricants, biomedicine, etc. Indeed, magnetic nanoparticles present appealing possibilities in biomedicine [1]. Because of their response to a magnetic field gradient they can be used as magnetic carriers, as they can be moved and fixed at distance and throughout human tissues. They can be directed to a particular target and there release a specific drug or molecule, in a magnetic-driven drug delivery process. They are able to be used as contrast agents to enhance the image contrast in magnetic resonance imaging (MRI). They can also be heated at distance by applying an alternating magnetic field as part of a hyperthermia process. Moreover, they can be a part of important *ex vivo* applications, like magnetic separation where the nanoparticles can be functionalized with a molecule that specially recognizes an analyte and thus separate it from solution, and biosensors, as it will be shown in this chapter.

One of the major demands in biomedicine is the early diagnosis of diseases. A large number of research groups are developing new methodologies to measure biomolecules and cells with high sensitivity in order to enable and improved the detection of a wide range of targets including DNA, RNA, proteins, enzymes, drugs, pathogens, and tumour cells. In particular, the development of biosensors involves the participation of multidisciplinary groups due to the necessity of integration of chemistry, physics, medicine, molecular biology and informatics. A biosensor is a device that includes a biological entity to measure in a selective way, specific substances of biological importance, and it can be used in fields such as environmental science, food science and biomedicine.

Nowadays the design of biosensor parameters is focused on improving sensitivity and providing detection in real times. Grant et al. presented a new strategy to detect biomolecules. They have developed a protease biosensor that is able to detect trypsin, by means of physical adsorption on the surface of silica nanobeads and detecting it by fluorescence resonance energy transfer. The nanosensors demonstrated a limit detection of 12.3 g/ml with a response time of 2 min [2]. Another strategy has been reported by Fan and col. They describe a new technology based on the measurement of the Brownian motion of polymer nanobeads using a microparticle tracking velocimetry to detect antigen–antibody interactions [3]. The group of Goodey have developed a chip biosensor that use polystyrenepoly(ethylene glycol) and agarose microspheres to detect a variety of analytes including acids, bases, metal cations, and antibody reagents. Identification and quantification of analytes occurs via colorimetric and fluorescence changes to the indicator molecules that are covalently attached to the polymeric microspheres [4].

Magnetic nanoparticle materials have been an interesting object of study in biosensing due to the improvement of sensibility, and their capacity to be integrated in multianalyte systems. Maghemite and magnetite are both iron oxides that present special properties in the nanometric scale. They are widely used in biomedical applications. The superparamagnetic behaviour from iron oxide nanoparticles confers magnetic properties to the materials that manifest only under a magnetic filed. When

the field is taken away, the particles do not retain any magnetic remanence. Zhang et al have reported a theoretical study for the detection of magnetic nanoparticles in sensors based on the Hall Effect [5]. An experimental approximation of biosensors based on the Hall Effect has been proposed by Thanh and co-workers. They have developed a sensor that can provide real-time profiles for the detection of Dynabeads M-280 under a magnetic field with a resolution of 0.04 beads per μm^2 [6]. Another approach to use magnetic particles in biosensors has been described by Ghionea and col. They present a detection scheme for a immunoassay sensor based on antigen-antibody interactions by means of a microwave circuit and using magnetic beads that improve the signal [7]. The advantages of using magnetic nanoparticles were highlighted in a study carried out by Qui et al. In this work, the magnetic core–shell Fe_3O_4@Au nanoparticles attached to the surface of a magnetic electrode were applied to study the immobilization of myoglobin. The electrochemistry of the nanocomposite was characterized by electrochemical impedance spectroscopy, and cyclic voltammetry. This system shows potential application for fabricating novel biosensors [8].

A number of iron oxides are biocompatible as they are present in living organisms. However, to be used in biomedical applications is fundamental to keep them in a reduced size by preserving them from agglomeration by a protective layer that can be composed by different materials. Organic coatings are widely employed in the field of biosensors in order to obtain core-shell nanoparticles. Patris and col. [9] have developed an electrochemical immunosensor assay for the determination of *anti-Clostridium tetani* antibody in serum. The antigen was immobilized above superparamagnetic beads coated with streptavidin and then they were put in contact with the tetani antibody. Later they react with a peroxidase-labeled anti-IgG. The resulting immunobeads were retained onto the carbon working electrode by means of a magnet. The quantity of tetani antibody in the samples was determined by an amperometric method. The assay was less time consuming than the ELISA method and can be easily implemented using a portable electrochemical device. Mak and his group have reported an electromagnetic biosensor that employed magnetic labelled

analytes (proteins, antibodies, DNA) with a magnetic system for binding strength measurements [10]. By labelling these analyte molecules with superparamagnetic polystyrene microbeads and by generation of an electrochemical current at the microelectrodes the successful biochemical recognition can be transformed into an electrical signal. The application of a magnet on the microbead labels can be used to separate non-specific from specific bindings allowing the measurement of the binding force between the molecules. The data could be obtained in a single measurement and, the instrument required is very low cost.

However, organic coatings use to be chemically unstable. Silica is an inorganic biocompatible coating that avoids agglomeration and confers to iron oxide core-shell nanoparticles stability in physiological media. Moreover, silica posses free silanol groups localized at the surface, which can interact chemically with different molecules providing a high added value to the system. Jang et al. have described a method to functionalize well-dispersed silica coated iron oxide nanoparticles with magnetic cores of 10 nm in diameter and about 2 nm thick silica shell [11]. First, the particles were synthesized using a coprecipitation method. Then, they were coated with a silica layer by means of TEOS hydrolysis and condensation. Next, the particles were bonded to the amino group of APTS. The carbonyl groups that point outward can be covalently attached to the amine groups of antibodies, enzymes, proteins, etc. through the formation of a very stable amide bond. This experiment successfully showed the functionalization procedure of the magnetic nanobeads with some proteins. This kind of materials based on nanobeads-protein bonding has been widely studied for biosensing and for biological markers [12, 13].

One of the main objectives in magnetic biosensors is how to achieve materials with high chemical stability, superparamagnetic behaviour, with a considerable size of a few hundreds of nanometres, and the capacity to be functionalized with a biological vector. These are the reasons why we decided to design a system able to integrate magnetic nanoparticles into a solid material. These nanoparticles are protected by a silica coating in a core-shell structure, which provide mass and stability to the system, and also points of anchoring to functionalize the particles with biological entities.

In the design of systems for biological applications is of great interest to take into account the specific applications for what it has been conceived for. Consequently, each case requires a group of characteristics to be accomplished by the materials for the smooth running of the biological system. In most applications the size and morphology of the entire system is of remarkable importance, that is why is needed to have a good control of such parameters since the synthesis of the materials. But it is also fundamental the easy functionalization of the system. All these requirements had to be considered in the design of the biosensor materials described in this chapter.

The main aim of this chapter is the design and synthesis of a material, which we are going to name nanobeads, to be useful in a molecular recognition system. Nanobeads consist of silica spheres of about 150 nm that contain inside maghemite nanoparticles of 5 nm of diameter. Their surface has to be functionalized by a carboxylic acid to allow bioconjugation with several proteins. The nanobeads will be utilized for protein determination in an impedimetric biosensor proposed as part of the ONCNOSIS project within the Programa CENIT Ingenio 2010.

4.2 Synthesis and characterization of superparamagnetic nanobeads

In this section we describe the synthesis of the superparamagnetic nanobeads and their characterization developed according to the requirements of the impedimetric biosensor. We will also describe some of the difficulties that had to be overcome to fit with such requirements.

4.2.1 Synthesis of nanobeads

As we mentioned before, maghemite is a biocompatible iron oxide that coated with silica acquires suitable properties to be functionalized by means of the interaction of chemical functional groups that favour protein or antibody conjugation, depending on the biosystem necessities. Moreover, silica facilitates particle dispersion in biological fluids.

The procedure that we chose to synthesize maghemite nanoparticles coated with silica in aqueous medium is based in the sol-gel method. This synthetic route has the advantage that the nanoparticles are in a biocompatible medium since the first step, as only adjusting the pH and the ionic strength of the .medium. This technique consists in the formation of maghemite nanoparticles by basic hydrolysis in aqueous medium of halogenate precursors of iron, as we describe in chapter 1, and subsequently the coating with silica by different methodologies employing tetraethyl orthosilicate (TEOS) as silica precursor to obtain the beads.

Once the aqueous ferrofluid is obtained the product was filtered and resuspended in 20 ml of water. In this way the ferrofluid is prepared to be coated with silica by the Stöber method [14]. In order to get this, several procedures were carried out in which silica beads with size between 100 and 300 nm and maghemite nanoparticles from 5 to 10 nm in diameter inside silica structure were achieved. In the Stöber method, condensation of a silica precursor was produced in a mixture of ethanol and water, as is shown in the next scheme:

$$Si(OEt)_4 + H_2O + OH^- \rightarrow (OEt)_3Si(OH) + ROH$$

$$(EtO)_3Si(OH) + H_2O \rightarrow SiO_2 \downarrow + 3EtOH$$

In Scheme 4.1, it can be seen a general view of the strategy for the formation of core-shell beads. In a first step, the iron oxide particles were obtained. Afterwards, a layer of silica was formed around the nanoparticle by the Stöber method. In Figure 4.1a the TEM micrograph shows an image of iron oxide nanoparticles in aqueous medium. The shape and size are heterogeneous but for this application this is irrelevant. In Figure 1b the micrograph shows the iron nanoparticles encapsulated in the silica shell.

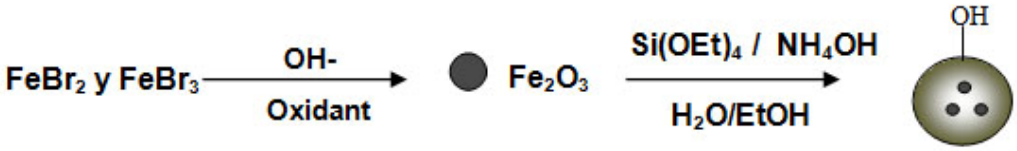

Scheme 4.1 Chemical scheme of nanobeads synthesis.

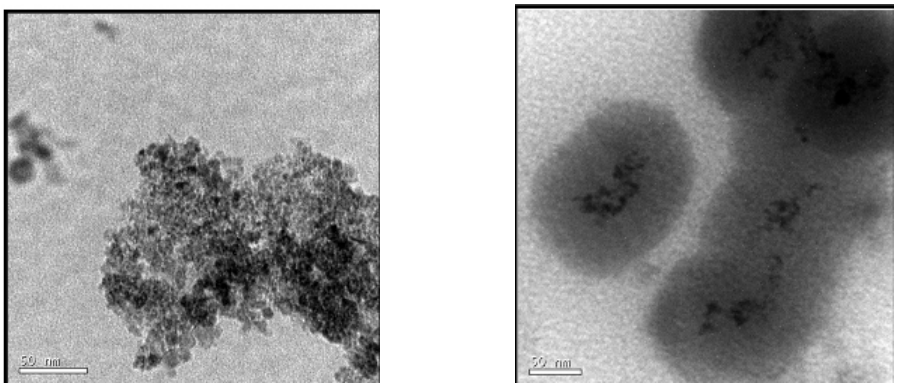

Figure 4.1 a) TEM maghemite NP b) TEM magnetic nanobeads.

Two processes have been studied in order to develop the best methodology to get the maghemite nanoparticles internalized in the silica matrix in aqueous medium for the biosensor. The first one is the method described by Deng et al based in the hydrolysis and condensation of TEOS in isopropanol-water mixture [15]. The second method is the one described by Salgueriño-Maceira performed in an ethanol/water mixture [16].

The first synthetic procedure is based in the Stöber method with some modifications. The coating of magnetite nanoparticles with silica was carried out in basic alcohol/water mixture at room temperature by using magnetic ferrofluids as seeds. First, the magnetic ferrofluid was diluted with water, alcohol and aqueous ammonia. Then, this dispersion was homogenized by ultrasonic vibration in a water bath. Finally, under continuous mechanical stirring, TEOS was slowly added to this dispersion, and after stirring for 4 h, silica was formed on the surface of magnetite nanoparticles through hydrolysis and condensation of TEOS.

In a typical synthesis of the second procedure, a mixture of NH_4OH, H_2O, EtOH, and the previously washed magnetic nanoparticles in water solution was added to an ethanolic solution of TEOS in EtOH while the solution was mechanically stirred. The hydrolysis and condensation of TEOS onto the magnetic nanoparticles was completed in 4 h. The formed nanobeads were centrifuged to eliminate excess reactants and redispersed in pure water.

4.2.2 Characterization

Both procedures permit to obtain silica nanobeads, but we achieve them with different shape and morphology. By means of TEM (Figure 4.2) we can observe an average diameter of 130 nm for the spheres formed by the isopropanolic method, and 80 nm for the ethanolic procedure. It is clear that the ethanolic method permits to achieve more homogeneous nanobeads than the ones obtained by the isopropanolic procedure; however, the ethanolic method also has also drawbacks as we explain below.

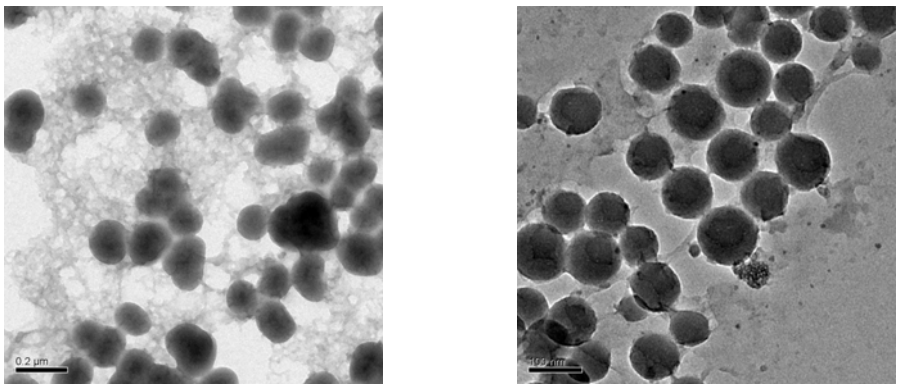

Figure 4.2 a) Isopropanolic method b) Ethanolic method.

We carried out several experiments to probe the reproducibility of both methodologies. The results were positive, but we also found some difficulties related to the sample concentration and the presence of impurities that we can see in TEM micrographs.

The first inconvenient that we tried to solve was sample dilution. We need more concentrate samples in order to perform the bioconjugation experiments. The obtaining of nanobeads is carried out in diluted solutions due to requirements of the synthesis. More concentrated samples can lead to form agglomerated nanobeads in the condensation of TEOS. So it was necessary to study concentration procedures that could provide non-agglomerated nanobeads. We chose centrifugation and evaporation of the solvent as possible methodologies to concentrate the sample.

The first methodology that we used to concentrate the sample was to evaporate the solvent. The ethanol was easily evaporated; however, the results were not as convenient as it can be seen in Figure 4.3: the samples were agglomerated.

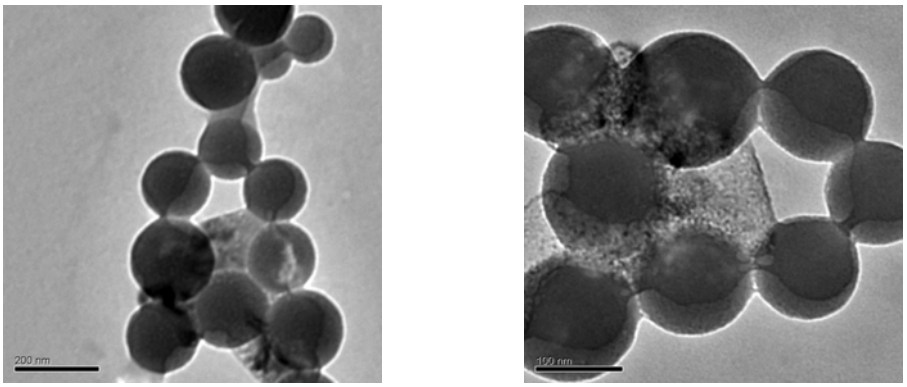

Figure 4.3 Solvent evaporation in ethanolic synthesis. a) Before evaporation, b) After solvent evaporation.

Then, we tried to concentrate the sample by centrifugation. The results can be seen in Figure 4.4 where the beads have lost quality as when we tried to concentrate them by evaporating the solvent. Before centrifuge, the nanobeads have well defined edges and spherical shape, then, after centrifuge the beads agglomerate and lose homogeneity in shape and size.

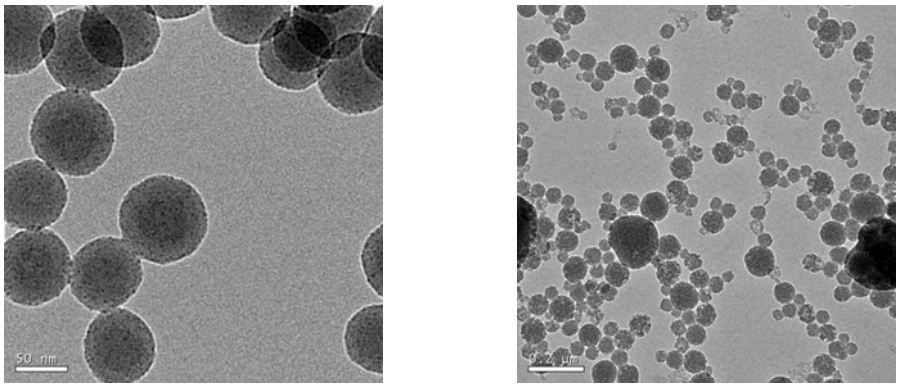

Figure 4.4 Solvent evaporation in ethanolic synthesis. a) Before centrifuge b) after centrifuge.

Moreover, although the ethanol method permits to obtain a major concentration of nanobeads, they are smaller than the obtained by the isopropanolic method. We attempted to grow the beads by employing more silica precursor in a posterior step. The results are shown in Figure 4.5. The nanobeads keep their shape and size but after centrifuge they agglomerate as well.

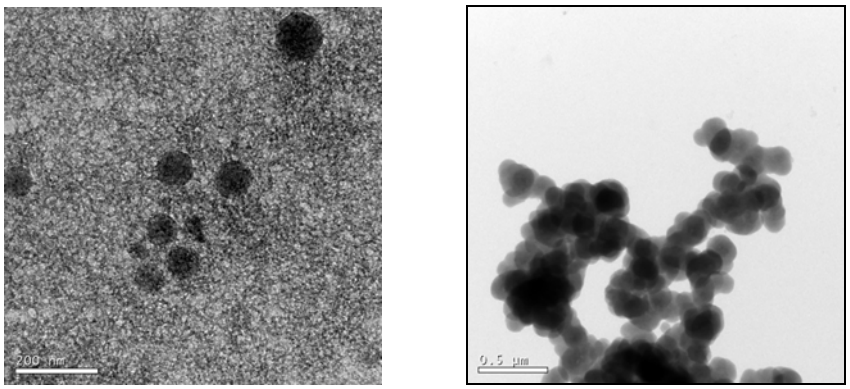

Figure 4.5 Ethanolic synthesis. a) Before centrifuge, b) alter centrifuge.

Analysis of equivalent results of the same concentration study following the isopropanolic synthesis are even more frustrated, as it can be seen in Figure 4.6.

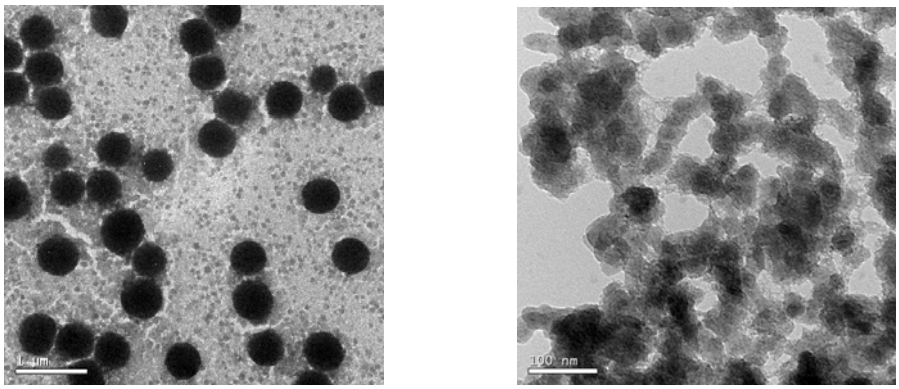

Figure 4.6 Isopropanolic synthesis. a) Before solvent evaporation b) after solvent evaporation.

We also attempted to increase the reaction time. The silica precursor was allowed to react during 24 hours in an isopropanolic suspension of the magnetic nanoparticles. We obtain nanobeads of diameters from 150 to 200 nm. In Figure it 4.7 can be observed the results of a synthesis of 24 hours in isopropanol. When we centrifuge the sample and disperse it in water, the morphology and size of the nanobeads are maintained and they do not seem to agglomerate after elimination of the solvent by evaporation.

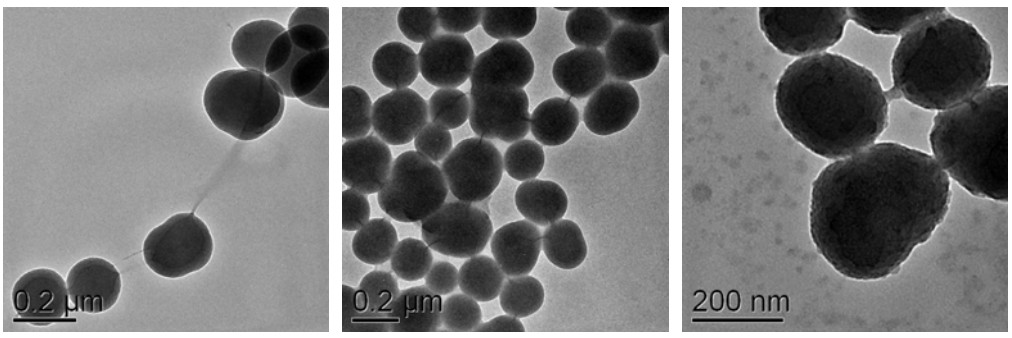

Figure 4.7 Isopropanolic synthesis 24 h. A) Initial sample, b) Centrifugation, c) Solvent evaporation.

Similarly, we carried out the ethanolic synthesis for 24 hours obtaining nanobeads of 100–200 nm with more uniform morphology than the one obtained by the

isopropanolic synthesis. When we centrifuged the sample, the particles conserved their original characteristics. Concentrating the sample by the solvent evaporation method also yielded good results. However, TEM images shown that there were impurities in the sample. When we centrifuge the sample we observe two deposits, one brown coloured on the bottom and another one, white, on the top. It can be due to the presence of maghemite nanoparticles outside the silica beads, instead in TEM pictures it can not be seen any nanoparticle neither, inside or outside, the silica nanobeads. This may be due to the high contrast of the sample in TEM. Thus, it is impossible to distinguish magnetic nanoparticles inside the nanobeads. Taken into account the obtained results, we decide to use the isopropanolic synthetic route instead of the ethanolic one and the centrifugation method to concentrate the sample.

In Figure 4.8 the procedure followed to obtain nanobeads following the ethanolic synthesis and keeping it for 24 hours is shown. As in the short reaction time synthesis, the centrifuged sample presented lower impurities content.

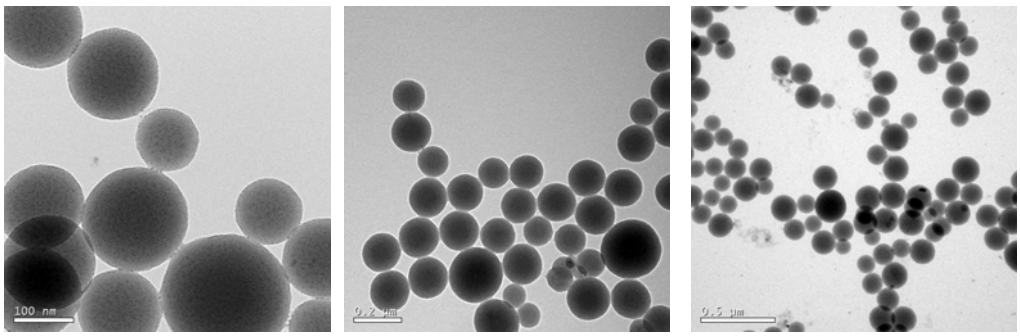

Figure 4.8 Ethanolic synthesis 24 h. a) Initial sample, b) centrifugation, c) solvent evaporation.

3.2.3 Nanobeads functionalization

To functionalize the surface of the silica nanobeads with carboxylic groups we chose carboxyethylsilanetriol. In aqueous/alcoholic media and by means of the action of an alkaly, this alcoxysilane reacts with the silanol groups at the nanobeads surface and condenses leaving the carboxylic group pointing outward. In Figure 4.9 it can be observed how, by means of the hydrolysis of a silane, it is possible to anchor to the

nanobead surface a molecule with a functional carboxylic group that is able to anchor a protein.

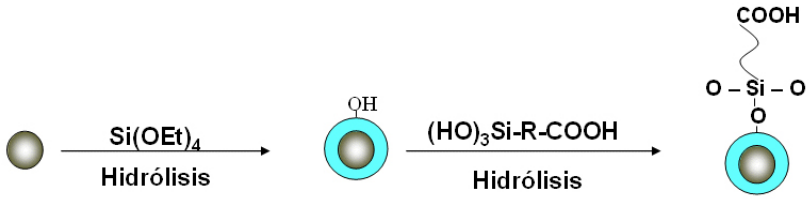

Figure 4.9 Scheme of the silanization of the nanobeads.

Once nanobeads were obtained following either the ethanolic or the isopropanolic routes explained before, the alcoxysilane was added. In both cases 0.07 ml of carboxyethylsilanetriol were added and mixed during 20 hours. After centrifugation, the sample was resuspended in water and washed several times to remove the excess of silane that was not reacted. The TEM micrographs of both preparations can be seen in Figure 4.10 before and after sililation.

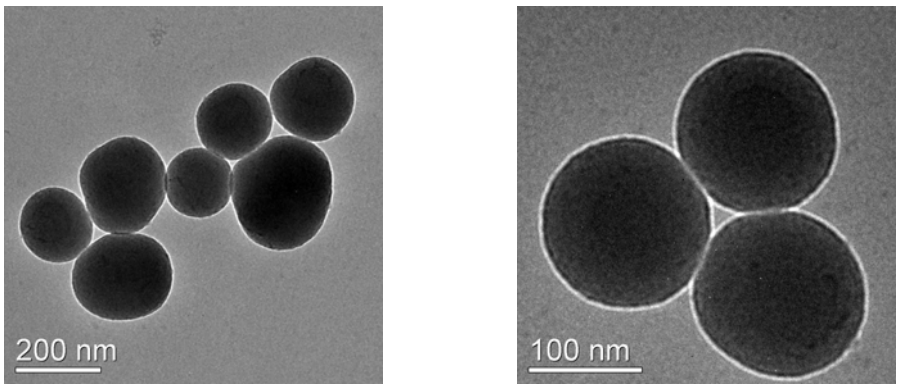

Figure 4.10: isopropanolic procedure. a) Before silanization, b) after silanization.

The morphology of the particles is well kept, however this does not indicate the anchoring of the alcoxysilane. In order to find it out, we compare the IR spectra before and after silanization, as depicted in Figure 4.11.

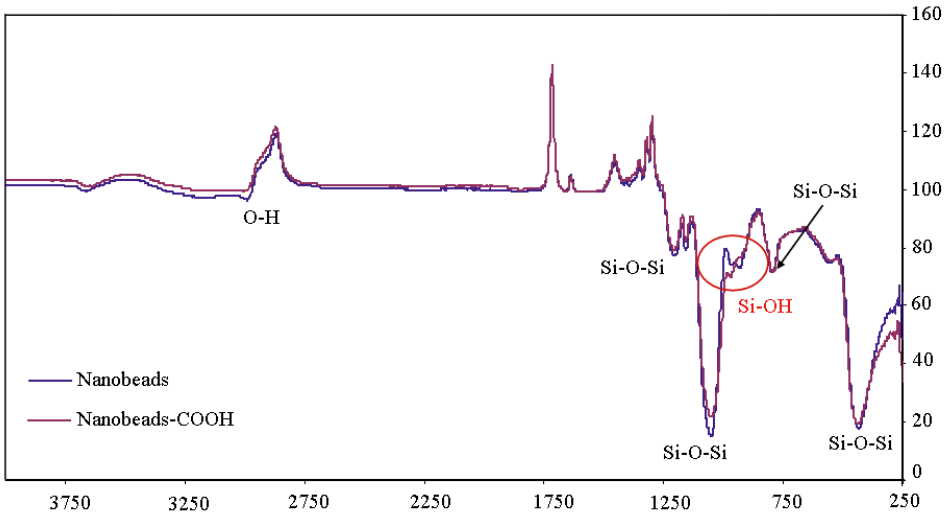

Figure 4.11 IR spectra of functionalized nanobeads (red line) and non-functionalized nanobeads (blue line).

The spectra of both preparations are coincident in almost all the frequencies, except in those where the silanol bonds appear. Silanol groups are only localized on the surface of the silica beads, hence there have been a surface modification. Due to the low concentration of the carboxylic groups their characteristic IR absorptions are not observed.

A study about the degree of functionalization of the nanobeads varying silane concentration was also carried out. With this purpose we perform a battery of experiments changing progressively the silane concentration, from 0.1 to 0.025 g of carboxyethylsilanetriol: A1: 0,1 g, A2: 0,085 g, A3: 0,05 g y A4: 0,025 g. The general tendency is that the silanization degree increases as the concentration of silane is augment. However for low concentrations, the results were more homogeneous, as it can be observed in Figure 4.12.

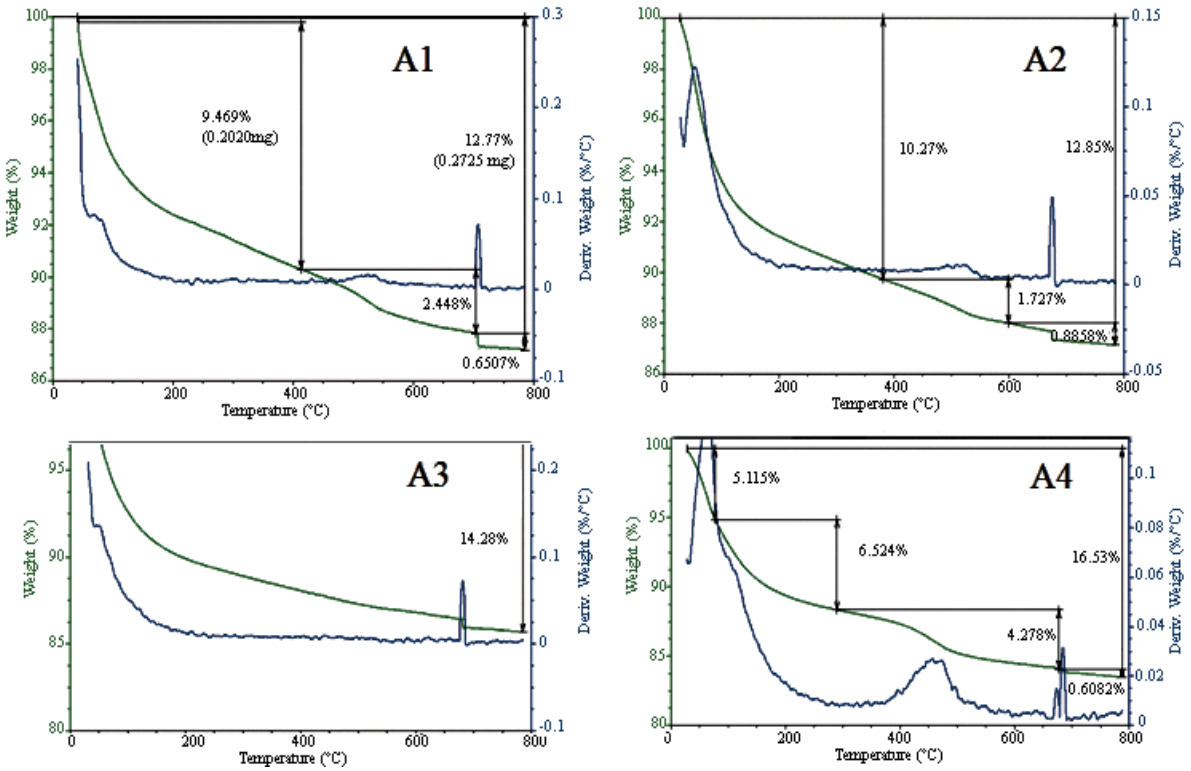

Figure 4.12 TGA of the silanized nanobeads with different quantities of silane.

The TGA technique consists of a study of the variation of weight while the temperature of the sample is increased at inert atmosphere. We can observe the total mass lose corresponding to the silane in the table.

A1:	0,1 g silane	16,53%
A2:	0,085 g silane	14,28%
A3:	0,05 g silane	12,85%
A4:	0,025 g silane	12,77%

4.2.4 Magnetic characterization

Magnetic measurements were performed using a commercial device MPMS-XL from Quantum Design with a SQUID magnetometer. The samples StoAc1 (isopropanolic) and StoAc2 (ethanolic) were washed, centrifuged and dried to obtain light brown powders, for their posterior magnetic characterization. The diamagnetic contributions of the sample holder ($-4.90\cdot10^{-7}$ emu/Oeg $_{capsule}$) and silica ($-4.47\cdot10^{-7}$ emu/Oeg$_{silica}$) were calibrated independently and their contribution was subtracted from the sample experimental data.

The in-phase susceptibility of samples StoAc1 and StoAc2 show evidence of a superparamagnetic blocking at temperatures T_B around 25 K (see Figure 4.13). Notice that T_B does not depend with the synthetic methodology used.

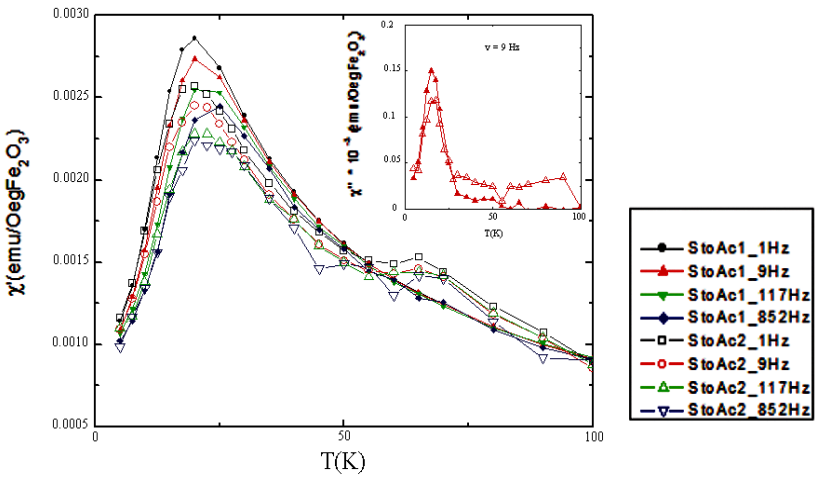

Figure 4.13: In-phase susceptibility at 1Hz, 9 Hz, 117 Hz, 852 Hz shows superparamagnetic relaxation at T_B = 25 K; Inset: out-of-phase susceptibility at 9 Hz show similar blocking temperatures for StoAc1 and StoAc2 samples.

Above T_B magnetic nanoparticles behave as superparamagnets so that magnetization curves should scale with H/T. The magnetization isotherms of StoAc1, shown in Figure 4.14, follow such behaviour, considering the temperature dependence of the magnetic moment displayed in Figure 4.16. However, this is not the case for the

magnetization isotherms of sample StoAc2 (see Figure 4.15). The discrepancy can be accounted for by a diamagnetic component. It may arise from an excess of silica in sample StoAc2 some nanoparticles which were unprotected by silica, become dissolved, leaving a mass contribution of the silica comparable to the contribution of the nanoparticles. Let us mention, at this point, that the silica contribution subtracted from the experimental data was calculated considering the preparation.

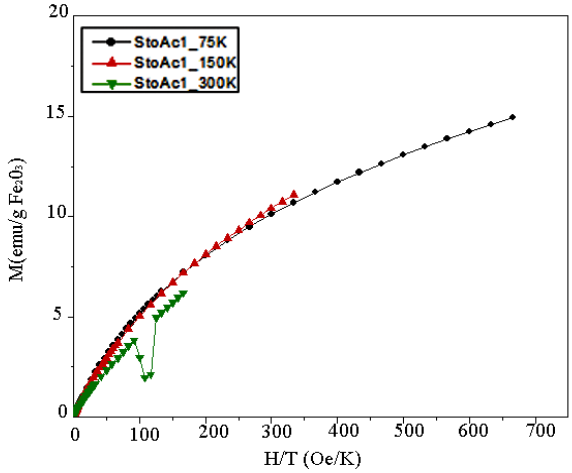

Figure 4.14 Magnetization isotherms of StoAc1 sample show superparamagnetic behaviour.

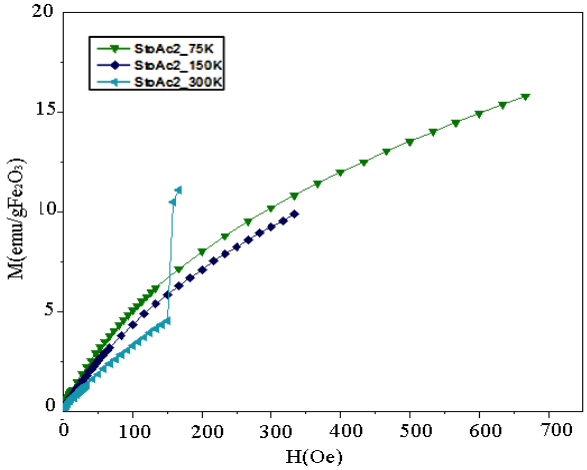

Figure 4.15 Magnetization isotherms of StoAc2 sample do not show superparamagnetic behaviour.

The magnetic moment of the nanoparticles is proportional to $(\chi T)^{1/2}$, where χ is the in-phase susceptibility. Figure 4.16 shows that this quantity is similar for StoAc1 and StoAc2 samples indicating that the nanoparticle magnetic volume of StoAc1 and StoAc2 samples is similar.

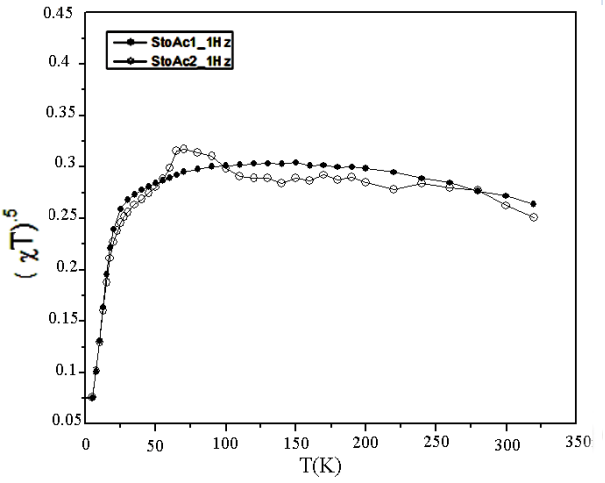

Figure 4.16: $(\chi T)^{1/2}$ of StoAc1 and StoAc2 samples is similar for both samples indicating that they have similar average nanoparticle magnetic volume.

The magnetic volume of the nanoparticles can be determined from the saturation magnetization. We obtain an average diameter of around 5 nm in agreement with the average nanoparticle volume observed in TEM images (Figure 4.17).

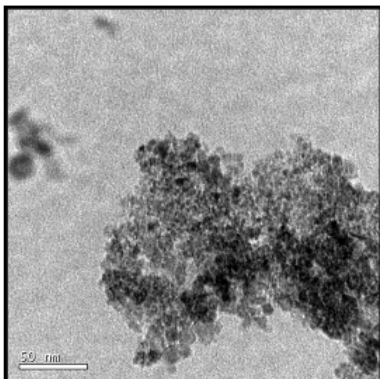

Figure 4.17 TEM micrograph of iron oxide nanoparticles

The blocking temperature T_B, determined as the temperature where the susceptibility is maxima at each measured frequency $f=1/2\pi\tau$ follows the Arrhenius law $\tau=\tau_0 exp(E/k_B T_B)$, as shown in Figure 4.18.

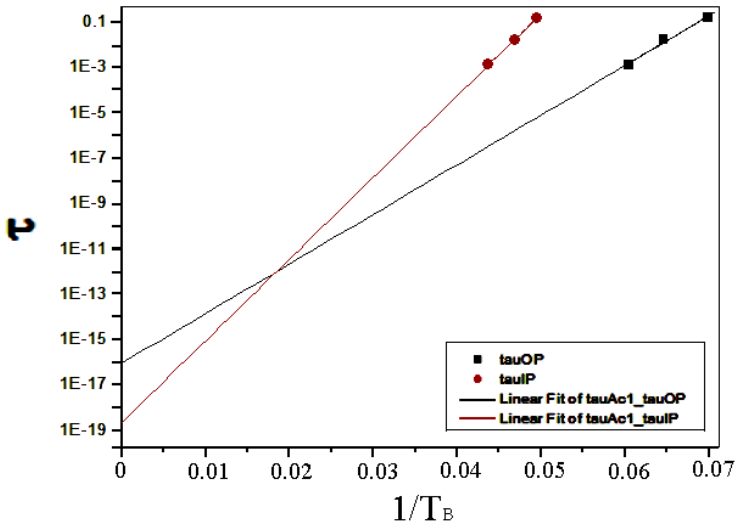

Figure 4.18 Relaxation time obtained from the out-of-phase (OP) and in-phase (IP) susceptibilities.

The magnitude of the relaxation time at $1/T_B \rightarrow 0$ is in agreement with the values reported for systems with presence of magnetic interactions between magnetic nanoparticles. Notice that as the blocking temperatures of both samples, StoAc1 and StoAc2, are coincident the influence of magnetic interactions on both samples is similar, suggesting that the distribution of the nanoparticles inside the nanobeads obtained by both procedures is similar.

Considering the values of the estimated particle size and the magnetic anisotropy of maghemite, $K_{eff} \sim 0.05 \cdot 10^6$ erg/cm^3, the susceptibility should show the superparamagnetic blocking at temperatures $T_B \sim 15$ K, a value which is lower than the experimentally observed (see Figure 4.13) even considering the influence of magnetic interactions. This reveals the existence of a large surface anisotropy.

Summarizing, the samples obtained by both synthetic methodologies provide silica nanobeads embedding magnetic nanoparticles of 5 nm diameter in average. The distribution of the nanoparticles inside the nanobeads obtained by both procedures can be considered similar, as the influence of magnetic interactions is equivalent. In the ethanolic route, some nanoparticles may become unprotected by the silica coating, being dissolved in the solvent, diminishing the ratio mass of nanoparticle/silica nanobead. However, the isopropanolic synthesis provides iron oxide nanoparticles well coated and with superparamagnetic behaviour.

4.2.5 Antibody conjugation

The bioconjugation reaction permits to attach a protein to a nanobead. It is based on the utilization of a crosslinker to favour the covalent bond between the carboxylic group at the surface of the functionalized nanobead and the protein amino group.

A protein consists of a sequence of amino acids. Some of these amino acids, like lysine, have amino groups in its structure that can react with the carboxylic groups of the nanobead forming a covalent bond. The amino group is a positive charge group in physiological conditions, and it is oriented outside the protein structure, thus is a group with easy accessibility for bioconjugation. But the protein-nanobead attachment it is not so easy. Normally the proteins have very amino groups and depending on the groups that interact with the nanobeads the protein can be denaturalized, losing its activity.

The 1-ethyl-3-(3-dimethylaminopropyl) carbodiimide (EDC) is a crosslinker widely used in the bioconjugation of antibodies. As it does not appear in the final bond between the grafting group, in our case the carboxylic acid, and the antibody, it is called zero-length crosslinker. Its efficiency can be increased by employing *N*-hydroxysuccinimida (NHS) or pentafluorophenol (PFP). In Figure 4.19, the chemical structure of these molecules is shown.

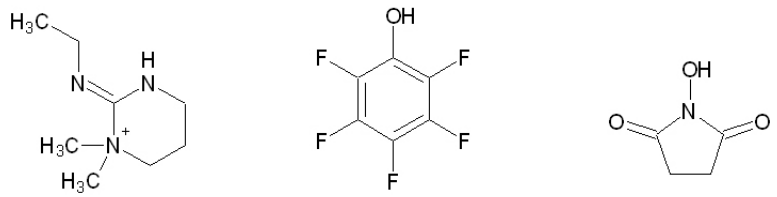

Figure 4.19 Molecular structures of EDC crosslinker and PFP and NHS activators.

In Figure 4.20 it can be seen the reaction scheme of a direct bioconjugation with EDC also employing PFP and NHS as activators to improve yields and decrease side reactions. In a typical reaction the carbodiimide of EDC reacts with the carboxylic group to produce an intermediate, the O-acylisourea. If there is not an accessible amine group able to react, the intermediate hydrolyze and lose its activity while the carboxylic group of the nanobead is regenerated. The use of activators, like PFP or NHS, avoids the undesired hydrolisys reaction thus increasing the efficiency of the bioconjugation reaction. Both, PFP and NHS are used to activate carboxylic acids towards an ester formation, which is more resistant to hydrolysis than O-acylisourea.

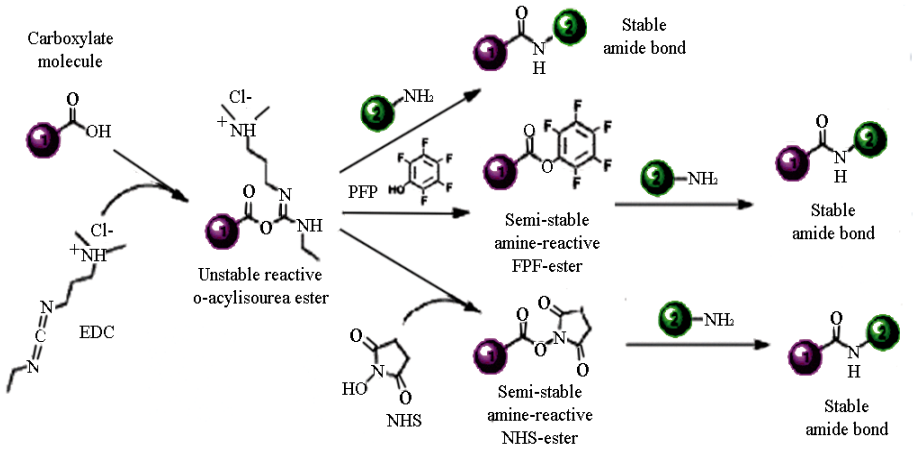

Figure 4.20 Bioconjugation scheme with EDC as croslinker. Ball 1 is the functionalized nanobead and ball 2 represents the protein.

The PFP permits the formation of high reactive esters that are very useful in nucleophilic substitutions. They react with primary and secondary amines to form an amide bond. The PFP esters are more reactive than the NHS esters, and easily handled, but more toxics. This is why NHS is widely used.

Commonly in reactions with EDC it is typically to achieve maximum yields in the 4.5 – 7.5 pH range. However, proteins are pH dependent and it is advisable to carry out the reactions at neutral pH to avoid conformational changes and even denaturalization which would affect its activity. The protein activity centres are very delicate. This is the reason why we carried out all the steps of bioconjugation in a phosphate buffer solution (PBS) at pH 7.2.

In the following we are going to describe step by step the bioconjugation of functionalized nanobeads with superficial carboxylic groups of two different proteins, the carcinoembryonic antigen (CEA) and an antibody bond to a peroxidase, anti-Goat-HRP. The bioconjugation reactions were carried out at the laboratories of Oryzon Genomics, from the Consorcio ONCNOSIS, and supervised by Dra. Cristina Fernandez.

The antibody anti-Goat-HPR is a polyclonal protein bonded to a horseradish peroxidase. This peroxidase is very useful to detect proteins, as we will explain later. A typical antibody consists of several structural units. Each unit consists of two heavy and two light chains. The structural units can form monomers if consists of one unit, dimers of two or pentamers of five. Although the general structure of all antibodies is similar, differences stay in a small region of the protein. This generates the existence of millions of antibodies, each one with a different end. The extremes can be bonded to a different target, and it is known as the antigen. This enormous diversity of antibodies allows the immunogenic system to recognize an equivalent amount of antigens. To produce large quantities of a specific antibody, an antigen is injected to a mammal, like a goat. The isolated blood of these animals has polyclonal antibodies (antibodies bond to the same antigen) in the blood serum. However, for analytical

applications a major specificity is needed. This is the case to detect small molecules and to block or detect very specific markers used in therapeutic applications.

CEA is a protein that is not usually present in the blood of healthy adults, although it presents significant levels in smokers, and in patients that suffer colon carcinoma, gastric carcinoma, lung carcinoma and breast carcinoma. CEA concentration is used as a tumour marker to identify recurrences after a cancer incidence. The CEA blood test is not reliable for diagnosing cancer but is a first indication of a possible recurrence. The level of CEA, in some cancers, can rise even before the precise point of recurrence can be localized by means of other techniques. That is why oncologists recommend a test of CEA levels for early detection of cancer. The antibody anti-CEA is non-specific, i.e. it is only recognized by the CEA antigen.

Reactants

Marker protein anti-CEA

Marker antibody Pab-Goat-HRP

EDC (1-Ethyl-3-(3-dimethylaminopropyl) carbodiimida

PFP (Pentafluorofenol)

EDIPA (Ethyldiisopropylamine)

$NaHCO_3$

Aminoethoxy Ethanol (AEE)

1x PBS (Phosphate buffer solution)

1x PBS is 10mM. (8g of NaCl, 0.2 g KCl, 1.44 g Na_2HPO_4 0.24 g KH_2PO_4 in 800 ml of distilled H_2O. Adjust the pH to 7.4 with HCl. Add H_2O to 1 litre.

Scheme for template 1

Table 1 gives the concentration of nanobeads and proteins we used for the conjugation of antibodies. The samples A398, A337 and A341 were prepared following the isopropanolic method and sililated as described before. In Figure 4.21 it can be observed the morphology and the size of the nanobeads samples used for protein conjugation.

A341 A398 A337

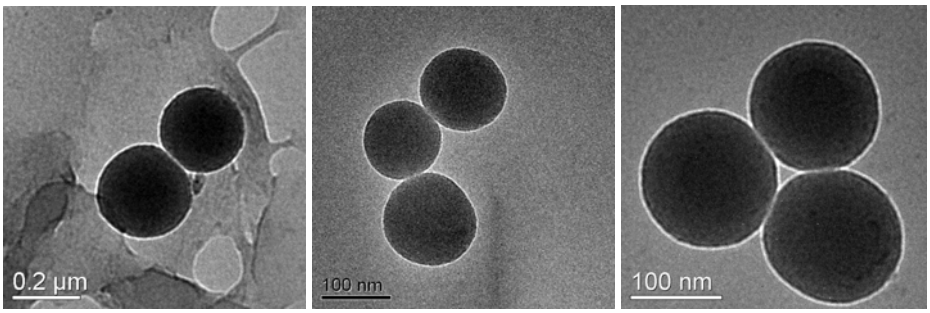

Figure 4.21 TEM of sililated nanobeads.

Table 4.1: Template for assay Nº 1

Sample	Nanobead/Protein	Nanobead	Protein
A	$1{:}10^6$	6000 µl A398A	2 µl anti-CEA
B	$1{:}10^6$	6000 µl A398A x 4	20 µl anti-CEA
C	$1{:}10^5$	3000 µl A398A	1 µl anti-CEA
D1	$1{:}10^5$	500 µl A341	1.25 µl anti-Goat-HRP
D2	$1{:}10^5$	2000 µl A398A	1.25 µl anti-Goat-HRP

Activation of the carboxylic groups

The first step for the conjugation of proteins to the nanobeads consists in the activation of the carboxylic groups at the surface of the nanobeads. For this purpose, we prepared a mixture of 144 µl of EDIPA with 144 mg of PFP in 4 ml of absolute ethanol. Subsequently 152 mg EDC-HCl were added. EDC was used to activate the carboxylic acid, as a metastable intermediate with PFP reacts with the amine of the protein. To remove the excess of PFP we used EDIPA.

On the other hand, the nanobeads were washed. We put 16 ml in eppendorfs of 1.5 ml (1ml ethanol: ml 0.5 ml nanobeads), and we wash them by means of centrifugation (3000xg, 1 minute, room temperature (RT)). The sample A398 is more diluted than A341 so we centrifuged 1.5 ml of sample A398, eliminated the supernatant and added 1.5 ml more. We made five samples like this and another one with 1ml of A398A. With A341 we only made one sample with 500 µl.

The samples A, B and C were incubated with 1 ml of EDC-HCl in the spinning wheel at room temperature during 60 min. In the reactions D1 and D2 we added only 500µL. Then the samples were washed with absolute ethanol (1 ml of ethanol: 1 ml nanobeads) by means of centrifugation (3000xg, 1 minute, RT). We washed three times and resuspend in the same initial volume of 1x PBS.

Conjugation of antibodies

The next step is the conjugation with antibodies. For reactions A and B we mixed two eppendorfs in one. Then we added the quantity of protein indicated in table 1. The mix was incubated in the spinning wheel for 3 hours at room temperature. The excess of antibody was removed by centrifugation (3000xg, 1 minute, 4ºC). The resulting liquid was washed with 1 ml of 1x PBS, for six times, and then proceeded to deactivate the carboxylic groups not bonded to an antibody.

Blocking the carboxylic groups

The non-reacted carboxylate groups were deactivated in a solution of aminoethoxy ethanol (AEE). This solution was prepared dissolving 10 mM in 100 ml of bicarbonate buffer solution at pH 8.3 ($NaHCO_3$ 100 mM: 0.84 g of $NaHCO_3$ in 100 ml of Milli-Q water). Then, 1 ml of nanobeads was resuspended in the $NaHCO_3$-AEE solution. The preparation was mixed in the spinning wheel for 30 min at room temperature. After that, the nanobeads were washed. We resuspend them in 1 ml de 1x PBS and centrifuge (3000xg, 1 minute, 4ºC). Finally the sample was resuspended with its initial volume but in 1x PBS.

Template schemes for assays Nº 2, 3 y 4

The same procedure was employed to carry out the assays that we show at the templates 2, 3 y 4 but with some variations:

In the assay Nº 2 we studied the bond between the marker protein Pab-Goat and the functionalized nanobeads at different concentrations and using EDC combined with NHS as crosslinkers, and without crosslinkers, as we show in Table 2.

Table 4.2: Template of the assay Nº 2

Sample	Nanobeads/Pab-Goat	Crosslinker 1	Crosslinker 2
A	$1:10^5$	EDC	NHS
B	$1:10^6$	EDC	NHS
C	$1:10^5$	–	–
D	$1:10^6$	–	–

The assay Nº 3 consists in studying the effect of crosslinkers (only EDC, or combiner with PFP, or without crosslinkers) in the reaction. The combination of both crosslinkers was analyzed together with the variation of the concentration of immunoglobulin G (IgG). The IgG is one of the five classes of antibodies that are produced by human body. It is the immunoglobulin predominant in physiologic fluids, as blood. This specific protein is synthesized by the organism in response to bacteria, virus and fungus invasion. Is the most abundant immunoglobulin in blood serum, with a concentration between 6–18 mg/ml.

Table 4.3: Template of the assay Nº 3

Sample	Nanobead/IgG	Crosslinker 1	Crosslinker 2
A	$1{:}10^5$	EDC	PFP
B	$1{:}10^6$	EDC	PFP
C	$1{:}10^6$	–	–
D	$1{:}10^6$	EDC	–

The assay Nº 4 combines the study of different proteins CEA and Pab-Goat with combined crosslinkers PFP and EDC.

Table 4.4: Template of the assay Nº 4

Sample	Nanobead/Protein	Protein	Crosslinker 1	Crosslinker 2
A	$1{:}10^5$	CEA	EDC	PFP
B	$1{:}10^6$	CEA	EDC	PFP
C	$1{:}10^5$	CEA	–	–
D	$1{:}10^5$	Pab-Goat	EDC	PFP

4.2.6 ELISA assay

The "Enzyme-Linked Immuno Sorbent Assay" (ELISA) is a biochemical procedure that permits to determine the presence of antigens or antibodies in a sample. The sandwich ELISA is a variant of this technique and is based on the detection of an antigen immobilized in a solid substrate by means of an antibody, the quantity of antigen in the sample is developed by adding a marked antibody to produce a visible signal measurable with a spectrophotometer.

Figure 4.22 shows a scheme of the assay. In a first step a protein is anchored in a polystyrene microtiter plate. Subsequently the walls of the holes of the plate were blocked with a blocking agent to avoid other proteins to interact and bond the surface. Then, the sample (protein conjugated nanobeads) is put in contact in the polystyrene plate with the adsorbed proteins. Weak bonds, such as hydrogen bridges, van der Waals forces and electrostatic and hydrophobic interactions stabilized the interaction between antigen and antibody, altogether forming a stable bond. The next step consists of attaching a detection antibody to the nanobead. The quantity of marked antibodies can be detected by means of a marked antibody, this is called direct ELISA). But the

antibody concentration can also be detected by employing a primary antibody and a secondary one marked, that is able to interact with the primary antibody, this is the indirect ELISA. The second method permits signal amplification, as more detection antibodies can be anchored to the primary one. The signal is measured by a spectrophotometer. The peroxidase (in our case HPR) of the secondary antibody reacts with 3, 3´, 5, 5´-tetramethylbenzidine (TMB), to form a blue compound. The TMB is a chromophore that in its oxidized form is blue coloured. This occurs when oxygen radicals are formed by the hydrolysis of the hydrogen peroxide from the HPR. The colour changes when the reaction stops by means of the addition of phosphoric acid or sulphuric acid producing a yellow colour measurable by a spectrophotometer at 460 nm. The TMB is a widely used substrate in ELISA assays because it is more sensitive and faster than other substrates.

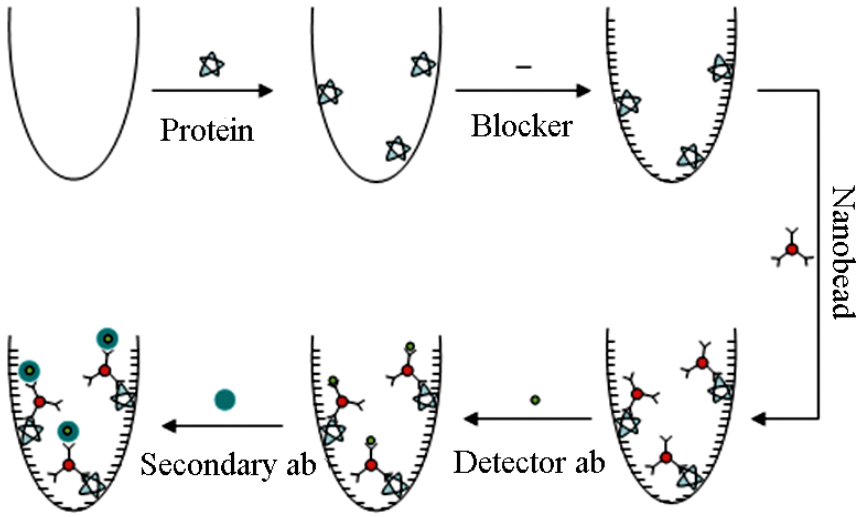

Figure 4.22 Scheme of a ELISA assay.

Experimental

0. Reactants:

1x PBS (Phosphate buffer solution)

CEA (carcinoembryonic antigen)

Anti-CEA

TMB (3,3´, 5, 5´-Tetramethylbenzidine)

H_3PO_4 2N

BSA 10% (Bovine serum albumin)

Capture antibody: Donkey anti-Rabbit

Secondary antibody: Pab-Goat-HRP and Anti-Mouse-HRP

1. ELISA for Template Nº1.

Table 5 shows the disposition of the samples in the holes of the plate prepared for the ELISA assay. Lines B and F show four dilutions of the used proteins, anti-CEA and Pab-Goat-HRP, acting as positive controls. There is needed unless four 1x PBS blanks as negative controls, that are distributed in the holes of the plate. We use them to assign the zero concentration signal.

Table 4.5: Disposition of the simples in the ELISA plate

	1	**2**	**3**	**4**	**5**	**6**
A	Reac. A	Reac. B	Reac. C	PBS	PBS	
B	1:100	1:10E4	1:10E6	1:10E12		
C	Reac. A	Reac. B	Reac. C	Reac. D1	Reac. D2	PBS
D	Reac. D1	Reac. D1	Reac. D2	Reac. D2	PBS	PBS
E	Reac. A	Reac. B	Reac. C	Reac. D		
F	1:100	1:10E4	1:10E6	1:10E12		

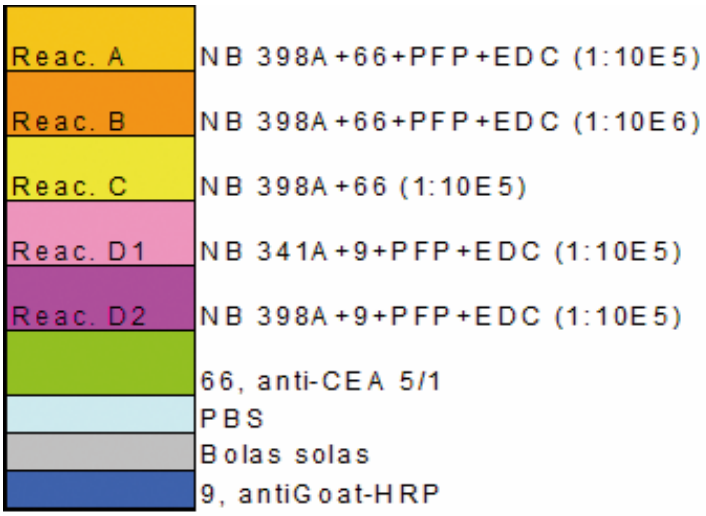

1. ELISA plate sensibilization.

In order to study the protein adhesion to ELISA plate, we fill the holes in this way: (1) cover the holes 1 A – 6 A and 1 B – 6 B con 100 µl of CEA 2 µl/ml in PBS, (2) cover the holes 1 C – 6 C with PBS, and (3) cover the holes 1 D – 6 D, 1 E – 6 E y 1 F – 6 F with 100 µl of Donkey antiRabbit 2 µl/ml in PBS. Then, we seal the plate with adhesive tape and incubate overnight at 4ºC. Afterwards, we wash the plate three times with PBS 0.1 % washing.

2. Blocking of the plate.

The next step is to block the plate. For this propose we add to each hole 200 µl of BSA at 1% in PBS and incubate during two hours at room temperature. Later, we wash three times the plate with washing solution.

3. Sample addition

Subsequently, we add 100 µl of sample in the corresponding holes. Then, we seal the plate with adhesive tape, and we leave it incubating for 1.5 hours at room temperature. Finally, we wash six times.

4. Detection antibody.

At this stage, we incubate the whole plate with 100 µl of secondary antibody in each hole, (anti-CEA diluted in BSA 1%) for 1 hour at room temperature. Then, we wash the plate six times.

5. Secondary antibody:

In order to increase the signal, we incubate the holes 1 A – 6 A, 1 B – 6 B and 1 C – 6 C with a secondary antibody bond to a peroxidase (100 µl of anti-Mouse-HRP (1:25000))

6. Detection

Finally, we add 50 µl of TMB by hole (2.5 mg/250 µL of DMSO; to 25 ml with sodium citrate buffer 0.1M pH 6; add 5 µL of hydrogen peroxide 30%), and then, we leave it to react for 5 minutes. The colour of the holes turns blue. In order to stop the reaction, we add 25 µl of H_3PO_4 2N. The colour turns to yellow. The results are stable for 1 hour, so it is needed to measure immediately. Eventually, we measure at 450 nm. The results are shown in Table 4.6.

Table 4.6: Spectrophotometric signal of the plate holes

	1	**2**	**3**	**4**	**5**	**6**
A	0,302	0,44	0,252	0,191	0,194	0,163
B	0,236	0,165	0,16	0,157	0,03	0,041
C	0,157	0,176	0,156	0,233	0,156	0,142
D	2,615	2,737	2,909	2,758	0,138	0,136
E	2,466	3,505	1,186	2,235	0,057	0,082
F	3,282	2,248	0,287	0,15	0,037	0,049

3. Results

- Template 1

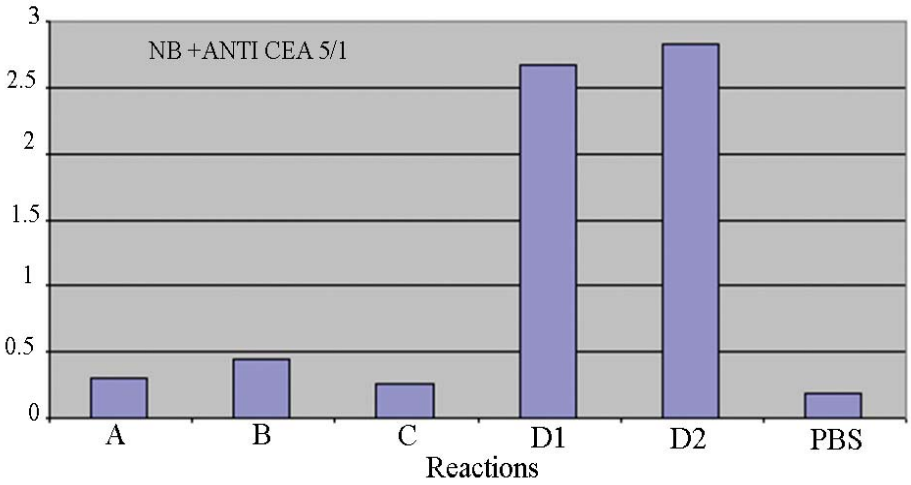

Graphic 4.1 Assay 1.

As we have mentioned before, CEA protein is used as a biomarker to detect gastric and other tumours. However, due to its poor specificity and sensibility cannot be the unique parameter for the diagnosis. The detection of high concentration of this protein in blood does not imply the presence of cancer, but is a first indicator. Reaction C corresponds to non-activated nanobeads (without EDC and PFP). The signal is similar to the obtained for A (with EDC and PFP and a concentration of $1{:}10^5$), but reaction A produces more signal, and B, with more concentration of conjugated antibody ($1{:}10^5$), produces even more signal. Hence from Graphic 4.1 we can conclude that a certain amount of nanobeads have been attached to the plate. Reaction D generates more signal because it corresponds to another antibody, the anti-Goat-HRP. Nevertheless, the relatively low signal of CEA should not be taken as a drawback. The human body has CEA at low concentrations and it can saturate the detector if it is very compatible with the substrate. So a low compatibility is better in this case.

- Template 2

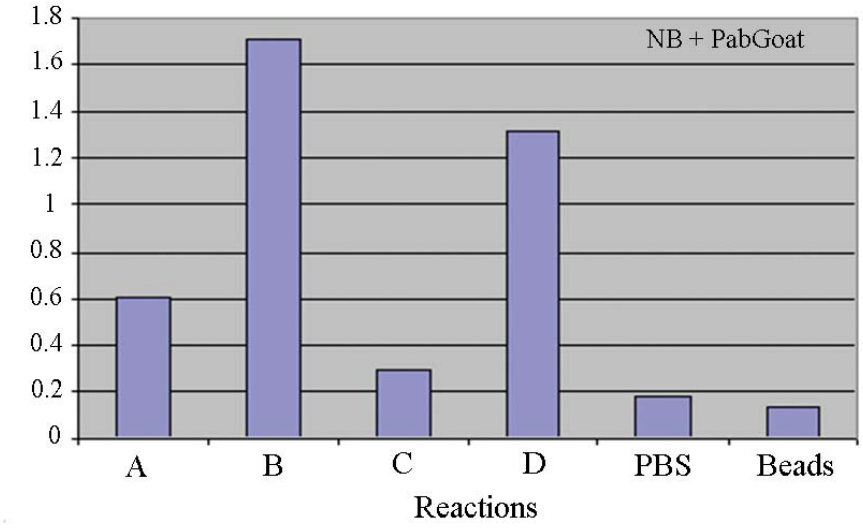

Graphic 4.2 Assay 2.

Protein Pab-Goat is widely used in protein studies due to its low specificity. As it is not able to interact with CEA, we chose Donkey anti-Rabbit as a capture antibody of Pab-Goat. In Graphic 4.2 it is observed that the signal was increased with respect to the concentration of Pab-Goat, in reaction A ($1:10^5$) with respect to B ($1:10^6$) as to C ($1:10^5$) respects to D ($1:10^6$). This is a good indication due to that evidences that the detection method is really rapid. But it is not a good signal that nanobeads without activation by a combination of crosslinkers (EDC and NHS), reactions C and D, are given a high signal, and that at high concentration of Pab-Goat (D) was rather significant. That shows that it is possible that a non-specific absorption between proteins and the surface of the nanobeads exists, due to electrostatic interactions.

- Template 3

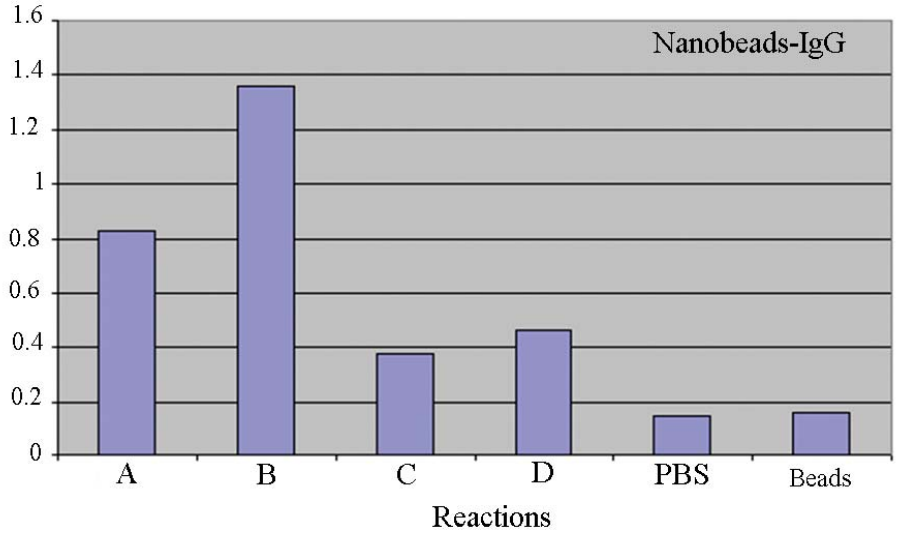

Graphic 4.3: Assay 3.

The immunoglobulin G (IgG) is one of the most widely used protein in biological studies due to it is easy to be obtained and cheap. The capture antibody that we use for this polyclonal protein is Pab-Goat. In Graphic 4.3 can be seen the behaviour of the IgG when it is conjugated to the nanobead and interacts with Pab-Goat that is immobilized above the ELISA plate. Reaction C represents nanobeads without functionalization. The signal is small, but it is bigger than nanobeads alone. As we compare it with the signal obtained for PBS, the nanobeads seem not to interact with the plate. These results made us suspect that also for this protein can exist weak interactions between nanobeads and IgG. With EDC, signal D, the signal is slightly increased revealing the small efficiency that the crosslinker has by itself (we have to remind that the optimum pH for EDC is 4.5 and we are at pH 7.2). However, as it has been demonstrated in other bioconjugation reactions, the combination EDC and PFP improves the yield of the reaction, as it can be seen in reaction B. Reaction A was performed with EDC and PFP, too, but the protein concentration was lower that in reaction B, so its signal is in accordance with B signal. C is a non-activated reaction,

so its signal is the lowest. And D signal is also smaller than A because it is not completely activated.

- Template 4

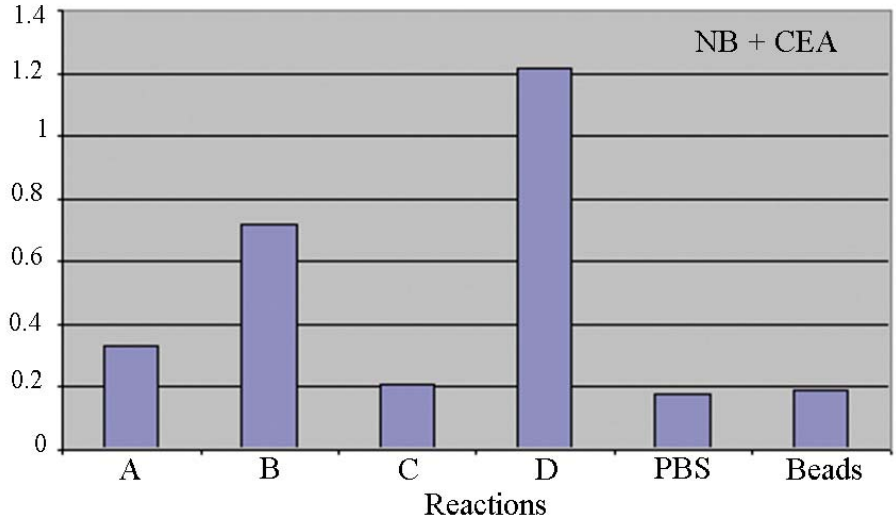

Graphic 4.4 Assay 4.

In this study we used the interaction between CEA and anti-CEA. The Graphic number 4.4 shows the line of action of the bioconjugated nanobeads with CEA, without activation (without EDC and PFP) reaction C ($1{:}10^5$), and activated with EDC and PFP, reactions A ($1{:}10^5$) and B ($1{:}10^6$) respectively. The signal of the reaction C in comparison with the signal of nanobeads without functionalization is similar and demonstrates that there are weak non-specific interactions. The signal of sample A shows that there is an increment due to the activation and the signal B indicates that when increasing CEA concentration the signal increases. It will be interesting to perform a kinetic study for a CEA concentration of $1{:}10^5$, for example, by varying the incubation time, in order to study the speed at which these interactions are established, for both samples the activated sample (A) and the non-activated one (b). Signal D corresponds to the activated nanobeads in contact with Pab-Goat ($1{:}10^5$). If we compare this signal with the obtained for CEA ($1{:}10^5$) activated with EDC and PFP

(signal A), it can be observed that the nanobeads functionalized with Pab-Goat show more affinity to anti-CEA.

4.3 Description of the biosensor

The main aim of the implantable biosensor named Oncnosense proposed in the frame of the project ONCNOSIS, is the detection of a variety of specific proteins in blood, particularly the quantification of the temporal variation of their concentration. In order to accomplish that purpose, a prototype that works in continuous is proposed. The proteins of interest for the biosensor are biological markers that are generated in four types of cancer: lung, ovaries, colon carcinoma and melanoma. The development of the biosensor and its components corresponds to other groups implicated in Oncnosis, where our responsibility was the design, preparation and supply of biofunctionalized nanobeads. However, due to the close relationship between the features of the nanobeads and the sensibility of the biosensor, we will briefly describe it here. We will also present the results of impedance measurements obtained with our samples.

Figure 4.23 shows a scheme of the implantation of the biosensor in a patient. The device is totality internalized and is in permanent contact with the bloodstream. In this way, when a target protein appears in the flowing blood, it will be detected immediately by the molecular recognition device and a signal will be sent to a reception system from the biosensor by means of radiofrequencies, indicating to the external receptor the likely presence of specific tumour cells. This will permit the doctors to know since a very early stage whether the cancer has been reproduced without the necessity of a periodic monitoring of the patient (analysis each six months, one year…) and allow them to act since the first moment before the cancer spreads and a drastic solution has to be taken. Therefore, the implantable biosensor will be indicated to patients that have suffered cancer before and they have high or middle possibilities of recurrence.

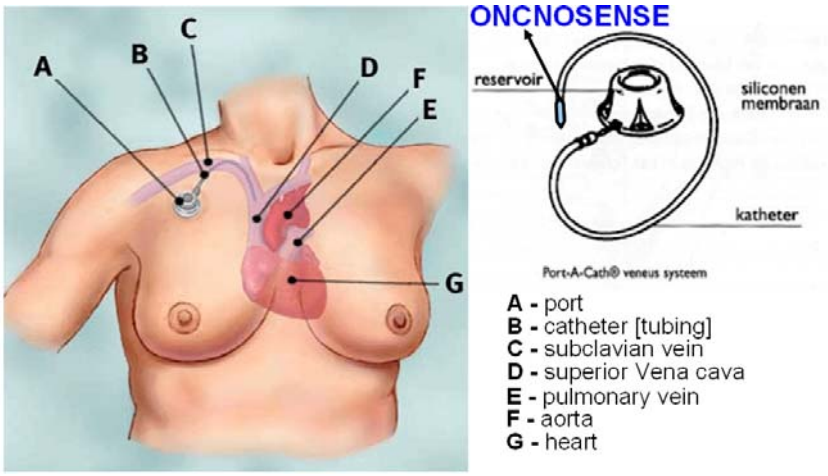

Figure 4.23 Biosensor implantation.

The Oncnosense system is formed by a reservoir and a catheter. The molecular recognition device and the radiofrequency transmitter are integrated in the reservoir of the system. While the catheter contains the microfluidic system that permits the separation of the plasma from the blood. The microfluidic system, therefore, enables the entrance of the plasma with the proteins to be analyzed in the molecular recognition device. In Figure 4.24 it can be seen a scheme of these components.

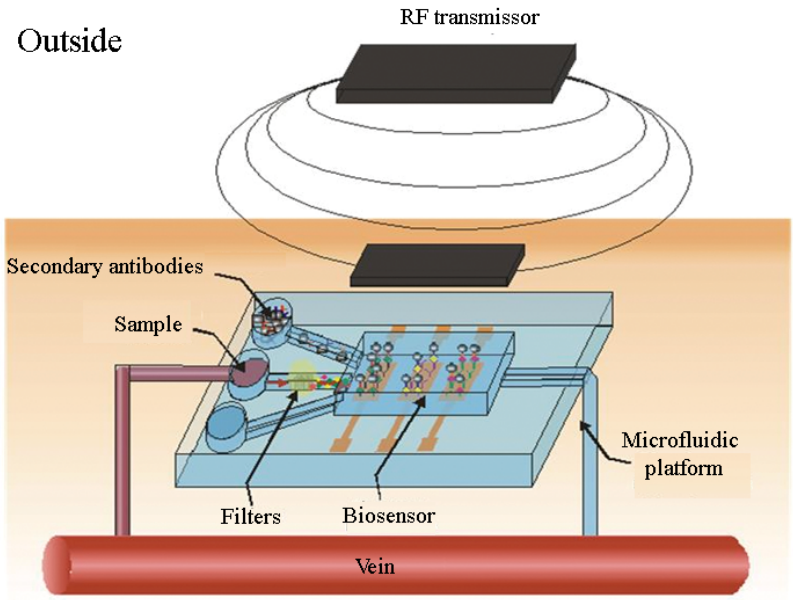

Figure 4.24 Biosensor components.

The molecular recognition device is based on the measurement of the impedance signal produced by the interaction of a system that we call nanobead with the electrode of a capacitor. In order to transform molecular interactions to measurable parameters, we will use nanobeads which dielectric and superparamegnetic nature will permit to detect significant changes in the impedance signal of the capacitor when they are modified by attachment of molecules to their surface. This nanobead system has many advantages in terms of durability and stability with time as compared to other sensing systems [17, 18]. In addition, the nanobeads enhance the amplification of the signal as they interact simultaneously with the electric fields (capacitive effect) and the magnetic fields (inductive effect) of the capacitor. Hence, the combination of both effects (dielectric and superparamagnetic) potentiates the detection of minor alterations in the nanobead surface by means of electrochemical impedance spectroscopy.

The nanobeads are made by the combination of a superparamagnetic material as iron oxide nanoparticles in the core of the system, and a dielectric material as silica,

that acts as a shell protecting the nanoparticles and forming a nanostructure with a spherical morphology. Both materials have the property of being biocompatible. The design and preparation of the nanobeads has been described in the first sections of this chapter.

Next, we will describe in detail the principal aspects of the biosensor that are directly related with the role played by the nanobead system in the molecular recognition device.

4.3.1 Molecular recognition device

As we mentioned before, the main objective of the molecular recognition device is to detect the proteins that are over-expressed in four types of cancer: lung, ovary, colon and melanoma. The detection of these analytes was performed by means of the interactions that are established between the nanobead core-shell system and the capacitor electrode. In Figure 4.26 we show the different components of the molecular recognition device. First of all, we have the nanobead system, designed according to the requirements mentioned before. The iron oxide nanoparticles contribute with their superparamagnetic property to the nanobead system as they decrease the impedance signal produced in the capacitor as they interact with the electrode. The encapsulation with silica, provides stability to the system but also, avoids particle agglomeration, and provides a mass increase with a positive influence in the signal as well. A most important advantage of silica stays in its surface, as the presence of silanol groups permits a simple functionalization of the nanobead with a carboxylic acid thus allowing its bioconjugation with a protein, e.g., a specific antibody of the cancer that we want to detect.

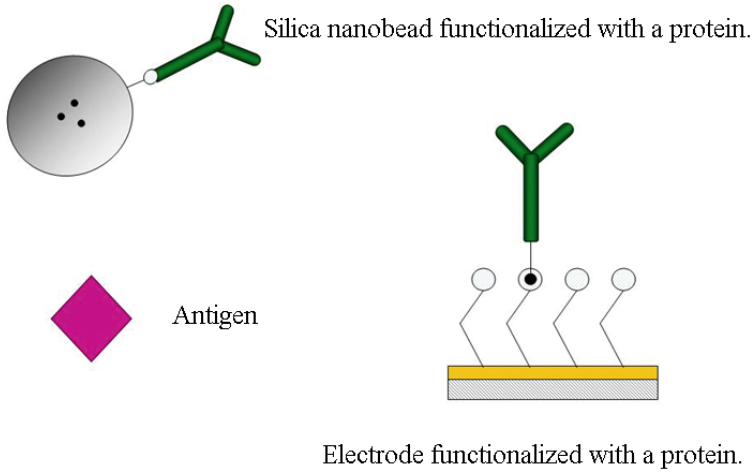

Figure 4.26: Components of the molecular recognition device.

There are several options for the functionalization of the electrode as it can be seen in Figure 4.27. The electrode consists of a silica oxide substrate coated with a gold layer. To anchor an antibody to this surface is necessary to coat the gold surface with a connective molecule such as an alkyl thiol carboxilate molecule. As it is well known, there is a strong covalent interaction between the thiol functional groups and gold surfaces. Then, when the bond is formed, the carboxylic group of the molecule will be orientated towards the external part of the surface and it can be able to interact with an antibody. Another methodology to functionalize the electrode is to coat this material with a biotynilated antibody. The thiol group can be bounded to the gold layer leaving the biotin in a good disposition to interact with other molecules. Subsequently a neutravidine is added. The avidine is a glucoprotein that presents in its surface hydrophobic regions where the biotine can be easily bonded. Once we obtain this union, the system can be exposed to the protein in which we are interested, but it has to be biotinylated to interact with the neutravidine.

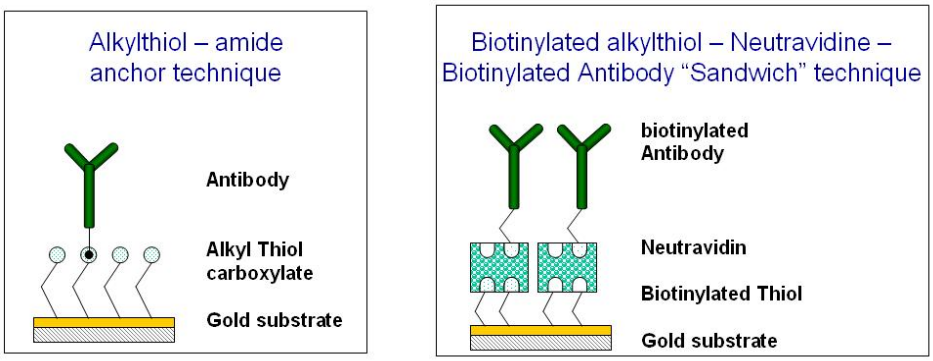

Figure 4.27 Methodologies for the functionalization of the capacitor.

In Figure 4.28 a photograph of the substrate coated with a layer of gold is shown. The electrode on the left has been coated, while the one on the right shows a clean surface just before coating.

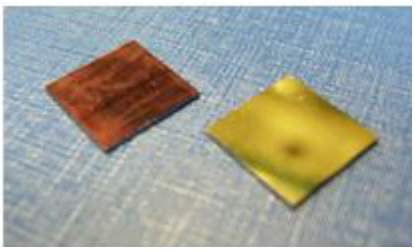

Figure 4.28: Silica substrate before and after coating with gold.

The technique used for the electrode functionalization is the micro contact printing (μ-CP), as it can be seen in Figure 4.29 where we illustrate the steps followed in this technique. In a first step a polymeric template made of polymethylsiloxane (PDMS) is fabricated. Subsequently, it is immersed in a solution containing the reactants and put in contact with the electrode. Then the template is taken off leaving in the electrode surface the adequate reactants fixed.

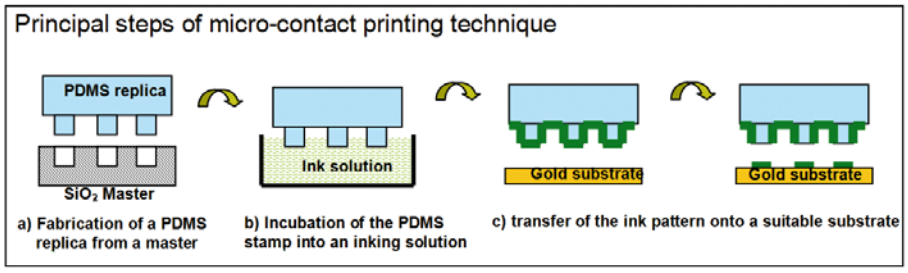

Figure 4.29 Micro-contact printing technique.

Hence, we have a system named nanobead that consist of iron oxide superparamagnetic nanoparticles encapsulated in silica and biofunctionalized with an antibody, and at the other side, a capacitor electrode that is functionalized by the same antibody. In order to establish an interaction between the nanobead and the electrode an antigen is needed, this antigen has to be able to interact with both systems. Figure 4.30 shows a scheme of the action of the antigen in contact with the different parts of the molecular recognition system. In a first step the antigen forms a stable bond with the nanobead.

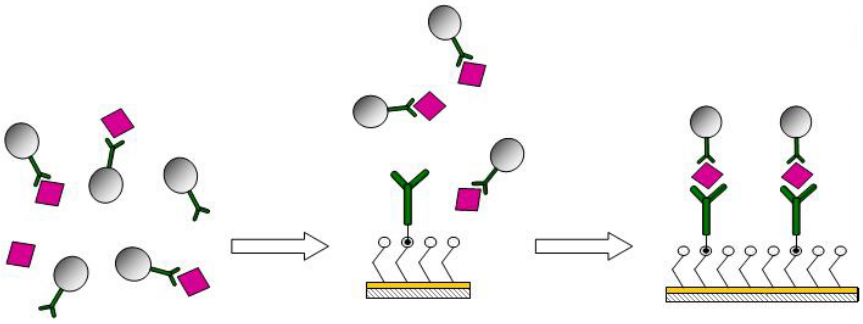

Figure 4.30: Sandwich interaction between nanobeads and the electrode.

Subsequently, when the nanobeads suspension is put in contact with the electrode, the antigen bonded to the nanobead can interact by means of a covalent or an electrostatic bond with an antibody in the capacitor electrode. This kind of bond between the antigen and the antibodies is called sandwich union. The change of mass in the electrode, the influence of the superparamagnetic nanoparticles, and the silica as

a dielectric, lead to a significant, and quantifiable, change in the capacitor electrode impedance.

A general scheme of a capacitor designed for the molecular recognition system given in Figure 4.31. Three gold electrodes were deposited on a silica substrate. One of them will act as reference electrode, another one as contra-electrode and the third as the analysis electrode, which will be functionalized with the corresponding proteins and will be able to interact with the analyte present in the plasma.

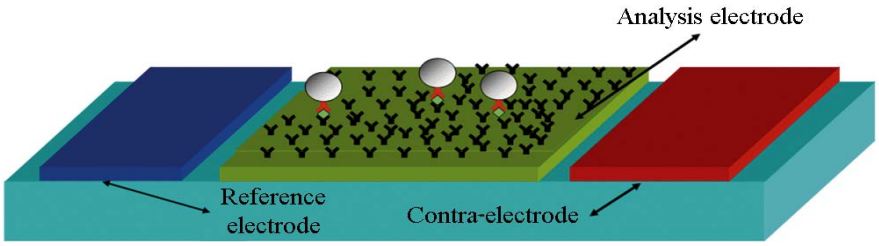

Figure 4.31 Molecular recognition system.

One of the advantages of the Oncnosense biosensor is that it can be potentially used to perform the simultaneous detection of several analytes. For this purpose a chamber is specially designed, where several biosensors are included and where the plasma is introduced. Each biosensor is functionalized with a protein over-expressed in each type of cancer (melanoma, ovary, lung and colon), in this way each biosensor individually will transmit its own signal. In Figure 4.32 it can be observed how 4 biosensors where integrated inside the same chamber.

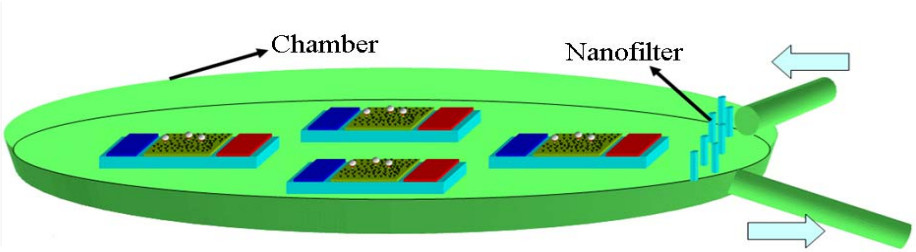

Figure 4.32 Chamber with four molecular recognition devices.

4.4 Impedance measurements and results.

4.4.1 Introduction

The electrochemical impedance spectroscopy (EIS) is based on the application of a low alternating current to an electrode in corrosion systems. Corrosion is an electrochemical process that involves molecules and ions. This method can be used in biological applications as biomolecules are able to interact with the electrode and change the impedance signal.

Often, the results obtained are analyzed using combinations of electrical circuit elements as capacitors, resistors and inductors. The analogous circuit components provide a way of modelling and allow the understanding of the corrosion process, see Figure 4.34, but they are not components of the corrosion process itself. We can observe how the reduction of the compound described in Figure 4.34a can be related to circuit described in Figure 4.34b. The response measured in current at different frequencies, it is named impedance spectra and the data obtained by EIS can be expressed graphically in a Nyquist plot (Figure 4.35).

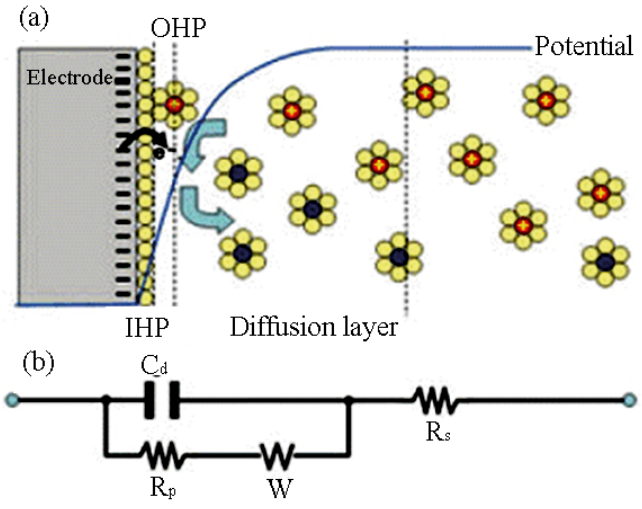

Figure 4.34 a) Scheme of the interface of the system b) Electronic components.

The nature of the interface, i.e. the solution in the proximity of the electrode, can influence impedance measurements in relation of its composition and the type of interactions that can be established with the electrode, see Figure 4.34. The Nyquist plot, also called Cole-Cole plot, are the most common way to represent the data of impedance spectra, it is also called graphic in complex plane due to the real component (Z´) is represented versus the imaginary component (Z´´) of the impedance, as it can be observed in Figure 4.35.

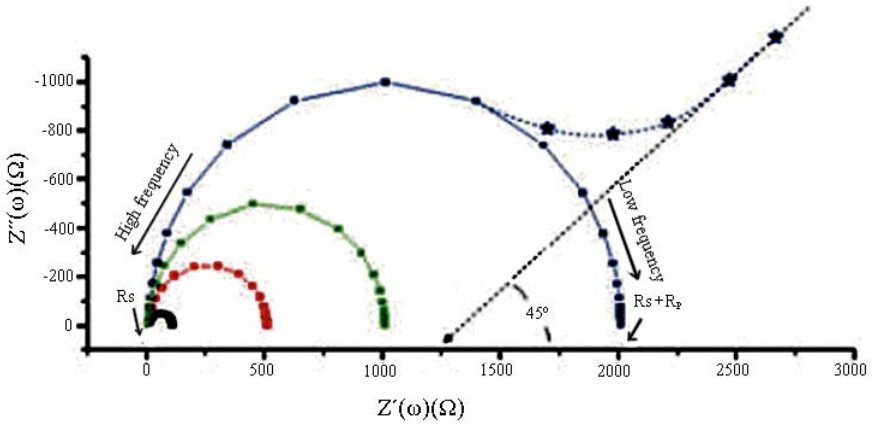

Figure 4.35 Impedance spectra (Nyquist).

The impedance immunosensors arise, among other reasons, as an alternative to ELISA assays for the determination of proteins. They present many important advantages, for example, they are cheap to produce, they can be easily miniaturized, can be integrated in a multianalyte diagnosis system, they posses a low detection limit, and they can be utilized in implantable systems. In the last years, this kind of sensors has raised much interest in biomedical applications. Several types of electrodes have been studied as the gold plates functionalized with a monolayer of thiols, metallic oxides coated with silanes, polymeric coated electrodes that are able to interact with biomolecules and covalent interactions between non-conducting films bonding covalently to biomolecules [19–22]. But also have been proposed other impedance immunosensors based on, for example, the electrodeposition of nanometric hydroxiapatite and magnetic nanobeads, among others [23, 24]. However, it is

necessary to study deeply the immunosensors, due to it is of great interest to improve characteristics as reproducibility, stability, or optimize the interactions between analyte and electrode, because the real samples complicate the process.

4.4.2 Impedance measurements

The impedance measurements that we describe here have been performed with our functionalized nanobeads samples, and have been carried out under the supervision of Dr. Christian Sporer in the Laboratory of Nanobioengineery from the Instituto de Bioingeniería de Cataluña (IBEC), directed by Prof. Josep Samitier.

The first step to obtain impedance measurements is to functionalize an electrode with the antibodies. In order to get this, we use commercial electrodes, and we functionalize them. Figure 4.36 depicts the general characteristics of the sensors we used. To functionalize the capacitor electrode it is essential to keep the work plate in contact with the reactants in a continuous way, avoiding solvent evaporation and the contact with the reference electrode.

Physical Parameters

Weight	Dimensions		
	Length	Width	Thickness
0.4 gms	25.40 mm	7.26 mm	0.63 mm

A = 4,00 ± 0,05 mm
D = 1,00 ± 0,05 mm

Electrode Materials

Electrode materials are defined by:

AC1.W*.R* (*)

The asterisk is replaced by the appropriate number or letter.

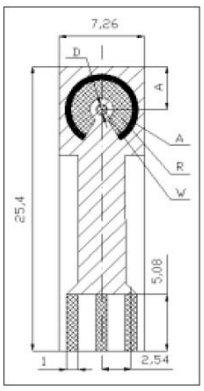

Figure 4.36 Electrode properties.

The way to obtain the electrode is to use a polymeric template, as shown in Figure 4.37. The reactants are dispersed in a solution that can diffuse through a capillary and the stamp to the desired area.

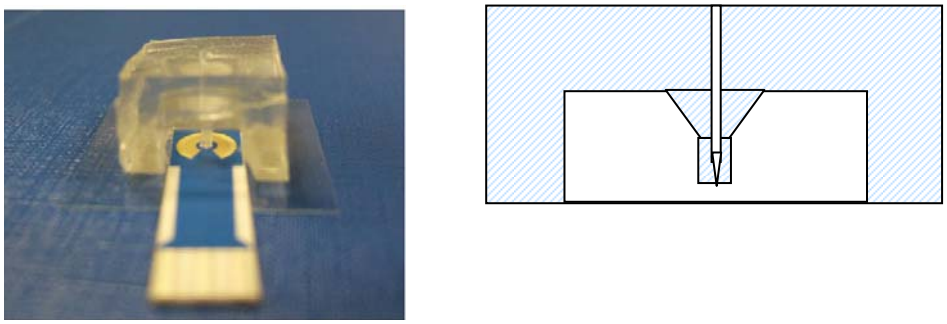

Figure 4.37 Capillary system and stamp above the electrode.

Impedance measurements have been performed following the methodology described before: 1) the electrode was treated with an alkyl thiol carboxylate, subsequently, the carboxylic groups were activated, and CEA was used as a capture antibody; finally the deactivation was carried out by means of AEE, and 2) the electrode was treated with alkyl thiol biotinylated molecule, then it was treated with neutravidine and mab-CEA biotinylated as capture antibody.

Series 1

In a first study we analyzed by means of impedance measurements the interaction between two proteins: Donkey anti-Rabbit and anti-Goat. One was attached to the electrode surface and the other one was dispersed in PBS. We choose this system first because the interactions are more powerful than the ones established between CEA and anti-CEA. The subsequent set of measurements was performed above a functionalized electrode with alkyl thiol carboxylate. Then the electrode was treated with Donkey anti-Rabbit to attach the protein to the electrode. In Figure 4.38 we can observe the results obtained for the electrode functionalization by means of atomic force microscopy (AFM). We can remark how the volume is increased by several

nanometers when the alkyl thiol carboxylate functionalized electrode is put in contact with the Donkey anti-Rabbit solution.

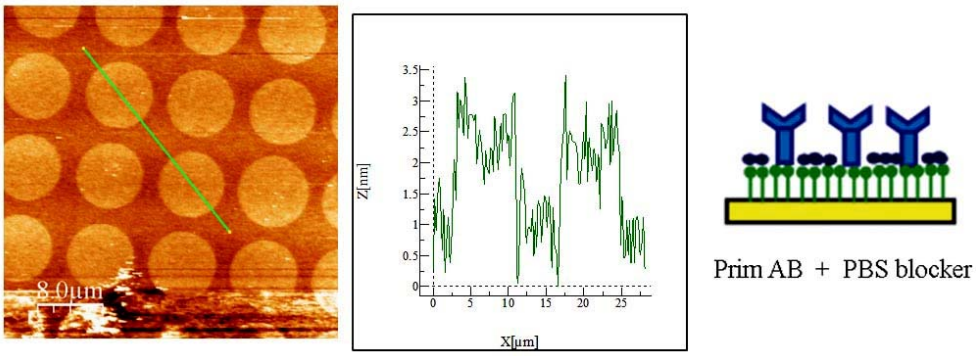

Figure 4.38 AFM of the electrode: gold/alkythiol-carboxylate/Anti-Rabbit

In Figure 4.39 the signals obtained for two suspensions of protein, one 10^{-8} M and the other 10^{-7} M of antibody anti-Goat can be observed. As it can be seen the signal are quite good in comparison with the signal obtained for a blank solution consisting in PBS. Although the detection limit is very low the saturation of the electrode arises somewhat faster than convenient. This depends on the degree of interactions that the proteins have with the substrate which in the specific case of anti-Goat and Donkey anti-Rabbit it is really high.

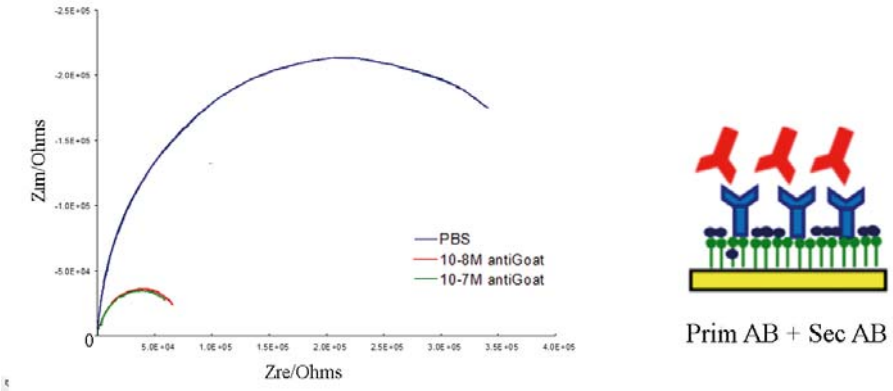

Figure 4.39: Impedance spectrum with two anti-Goat solutions.

In a first approximation with nanobeads, the measure of non-functionalized nanobeads was first carried out in a sample of 11 mg/ml and its dilution in PBS at 1:10 and 1:100, as shown in Figure 4.40. The signal decreases as the nanobead concentration increases. The small change that we can observe can be due to non-specific adsorption of some nanobeads at the electrode surface.

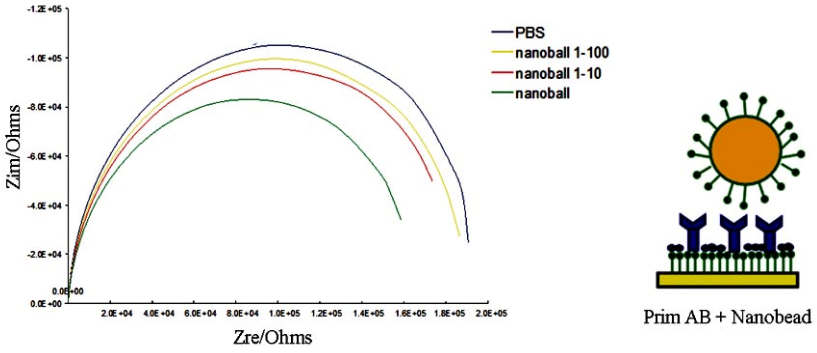

Figure 4.40: Impedance spectrum of nanobeads without functionalization and without secondary antibody.

Then, the measurements of a sample consisting of nanobeads with secondary antibody (anti-Goat) were performed. The sample was prepared in a proportion $1:10^6$ but without EDC (the protein is not covalently bonded to the nanobead), and its dilutions in PBS 1:10 and 1:100. Figure 4.41 shows how the signal considerably diminishes, probably due to interactions between free anti-Goat and Donkey anti-Rabbit.

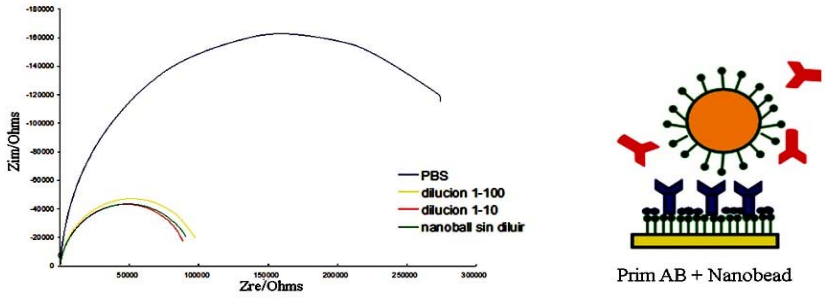

Figure 4.41 Impedance spectrum of non-activated nanobeads with secondary antibody.

Figure 4.42 shows AFM results obtained for the electrode in contact with non-activated nanobeads and secondary antibody, after washing. It can be clearly seen that the nanobeads were not attached to the electrode. This is in accordance with the supposition that the interactions between the nanobeads and the electrode were weak otherwise we should see by this methodology the nanobeads anchored to the electrode surface. However an increment of volume is observed as shows Figure 4.42. A possible explanation is that the signal can be produced by the secondary antibody that directly interacts with the functionalized electrode and not from the nanobeads.

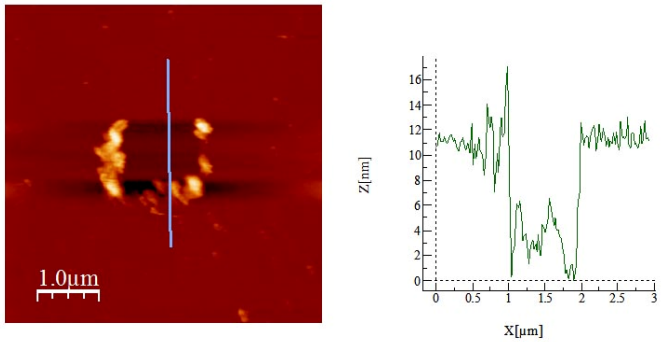

Figure 4.42 AFM of the electrode: gold/ alkyl thiol carboxylate/ Anti-Rabbit/nanobeads-anti-Goat without EDC.

The last assay of this set of experiments with anti-Goat and Donkey anti-Rabbit, corresponds to functionalized nanobeads (with EDC and PFP) in a proportion $1:10^6$ in contact with an electrode functionalized with Donkey anti-Rabbit and its dilution in PBS in a 1:100 ratio. Figure 4.43 shows the signal produced by the concentrated and diluted suspensions. In the case of the diluted sample no variation compared to PBS is observed. For the concentrate sample it can be seen a light variation.

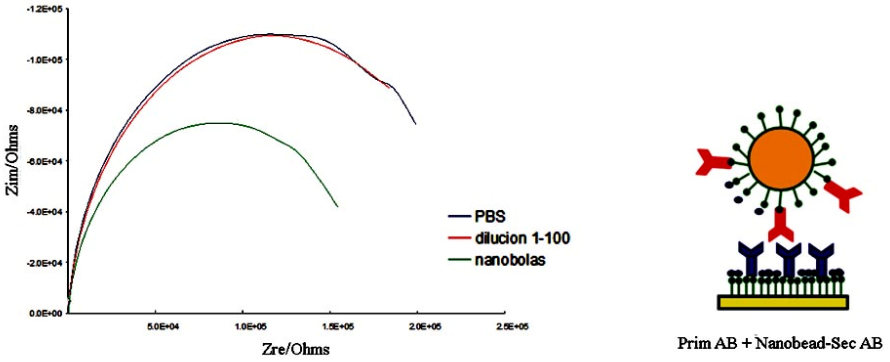

Figure 4.43 Impedance spectrum of activated nanobeads with anti-Goat.

If the nanobeads were covalently bonded to the secondary antibody and then bonded to the electrode antibody, we should notice a large change in the impedance signal with respect to PBS signal, however such change is not observed. To ensure whether the union is produced, an AFM study of the washed electrode was carried out. Figure 4.44 shows that there are not nanobeads above the functionalized surface with anti-Rabbit, thus corroborating the data obtained from the impedance spectrum. We can conclude that the union between the proteins was not satisfactorily established. It is possible that interactions between both proteins are not strong enough to resist the washing. But also can be due to problems in the interactions between anti-Goat (from the nanobead) and Donkey anti-Rabbit (from the electrode), because the active centres of this kind of proteins are very delicate. The signal obtained for this assay is similar to the obtained for nanobeads without anti-Goat, so we can assert that the nanobead do not interact with the electrode but neither with anti-Goat.

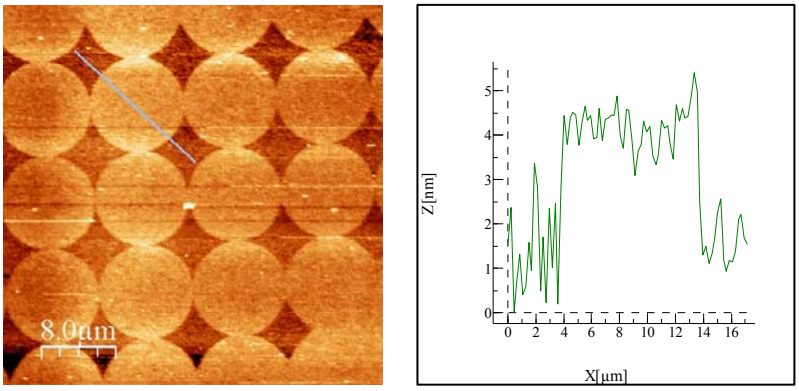

Figure 4.44 AFM of the electrode gold/alkylthiol carboxylate/ Anti-Rabbit/anti-Goat-nanobeads.

Finally we want to remark that nanobeads were only observed above non-washed electrodes as shown in Figure 4.45.

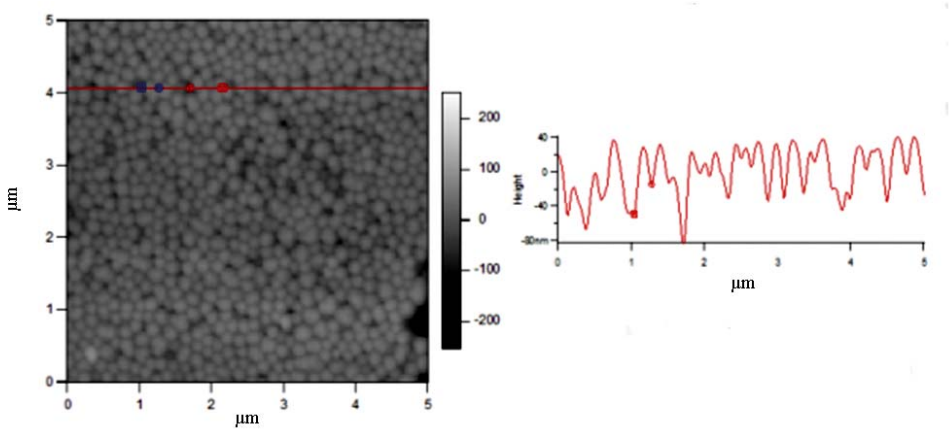

Figure 4.45 Nanobeads without functionalization directly avobe a gold electrode.

The AFM technique permits us to observe every step of the functionalization process, and results indicate that the antibodies attach to the electrode surface but not to the nanobeads, except in non-washed plates.

Series 2

Next, we are going to study another system that consists of the interaction CEA and anti-CEA with a functionalized electrode composed of an alkyl thiol carboxilate. The measures corresponding to Figure 4.46 are from an alkyl thiol functionalized electrode. It can be observed that as CEA concentration increases the impedance signal decreases due to CEA interactions with the electrode surface.

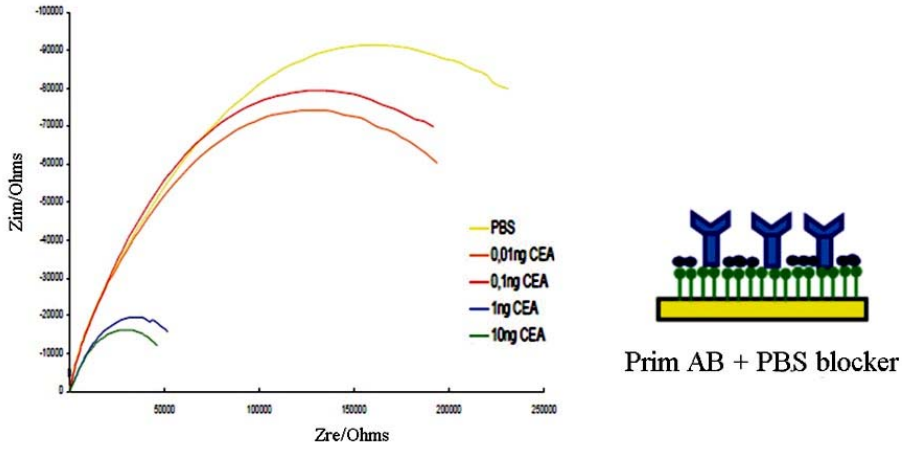

Figure 4.46 Variation of the impedance signal of alkylthiol functionalized electrode.

Next, we functionalize an alkyl thiol carboxylate electrode with anti-CEA in PBS, and then place it in contact with several solutions of CEA at different concentrations in PBS: 1, 2, 10, 20, y 40 ng/ml. Figure 4.47 shows the variation of the impedance signal of the samples in comparison with the PBS signal without CEA, considered the blank. For the measurements, a potential of 500 mV, an amplitude ac of 100 mV, and a range of frequency from 100 to 500 mHz were used.

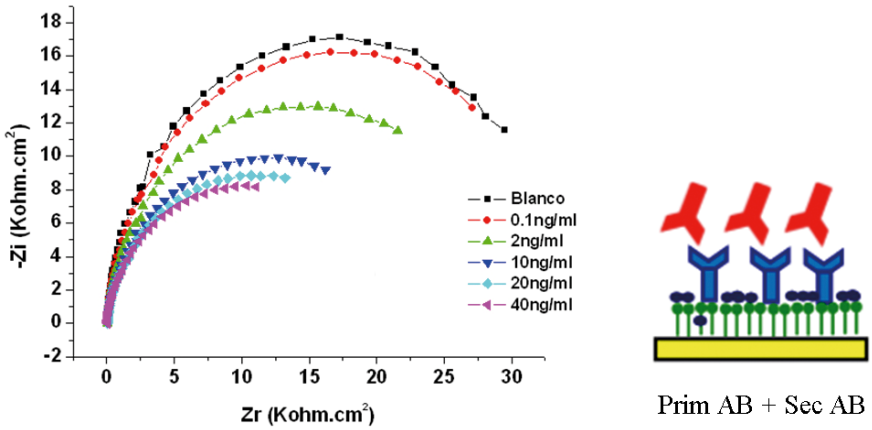

Figure 4.47 effect of CEA concentration in an electrode modified with anti-CEA.

It can be observed that the signal variation is quite small. In order to further characterize the µ-CP functionalized electrode we carried out AFM and Time-of-Flight Secondary Ion Mass Spectrometry (ToF-SIMS) experiments. Figure 4.48 shows the electrode characterized by AFM and ToF-SIMS. The circles in the AFM picture are where the anti-CEA is deposited; the rest of the electrode surface is the alkyl-thiol. In Figure 4.49 we show a 3-D image of the protein deposits by means of µ-CP.

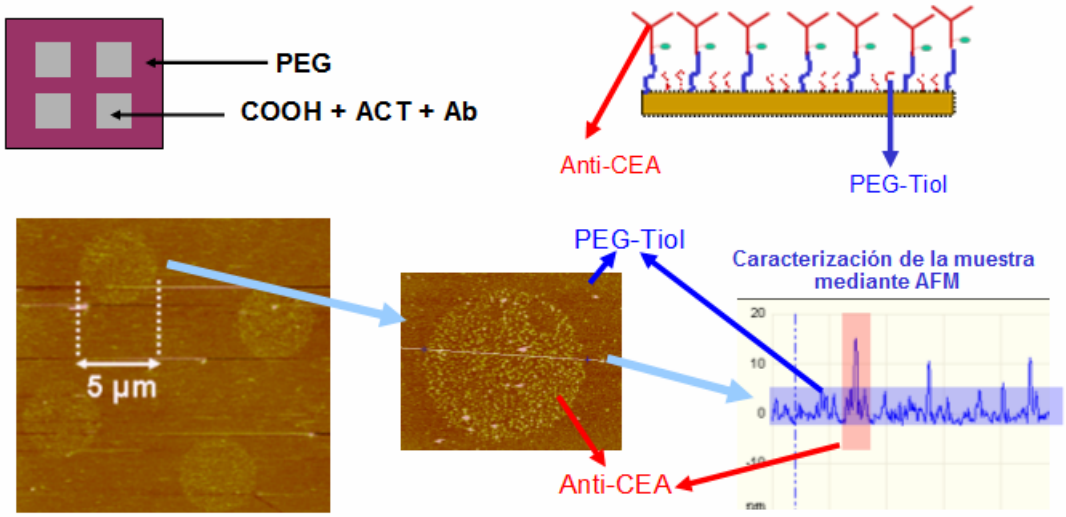

Figure 4.48 Analysis of the functionalized electrode by means of TOF-SIMS.

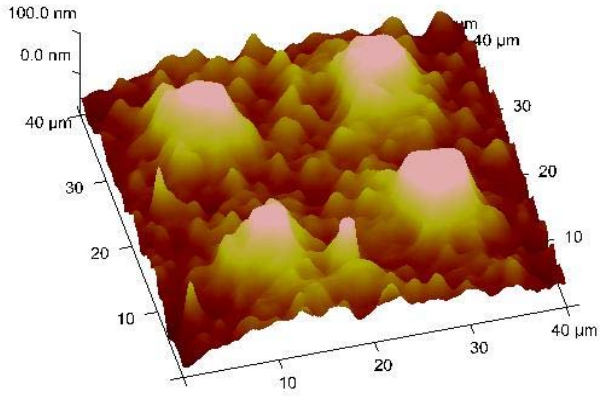

Figure 4.49 AFM characterization.

As in the previous series the interaction of antibody and antigen was not identified positively. It seems to be a problem related to the interaction of both proteins in their respective systems.

4.4.3 Electrode functionalization

In order to verify the electrode functionalization, three functionalized electrodes were characterized by means of cyclic voltametry (CV). CV is generally used to study the electrochemical properties of an analyte in solution. In our case, we will use ferrocianate to study its interaction with the electrode. The three functionalized electrodes analyzed were treated differently: the first one is an electrode treated with thiol acid, then activated with EDC and PFP, subsequently with CEA and finally deactivated with AEE; the second one is an electrode treated with 2 x alkyl thiol biotinylated, then neutravidine and finally CEA biotinylated, and the third one an electrode treated with 3 x alkyl thiol biotinylated, then neutravidine and finally CEA biotinylated. The alkyl thiol functionalized electrode CV signal shows an interaction between ferrocianate and the electrode. It can be due to that CEA was not covering the whole electrode surface. The second and the third experiments reveal better results

with ferrocianate. The best results are the obtained for the third electrode as it can be seen in Figure 4.50. The interaction of ferrocianate with the electrode is lower than in the alkyl thiol carboxilate electrode. It is due to that the alkyl thiol biotinylated electrode is coated very well with CEA.

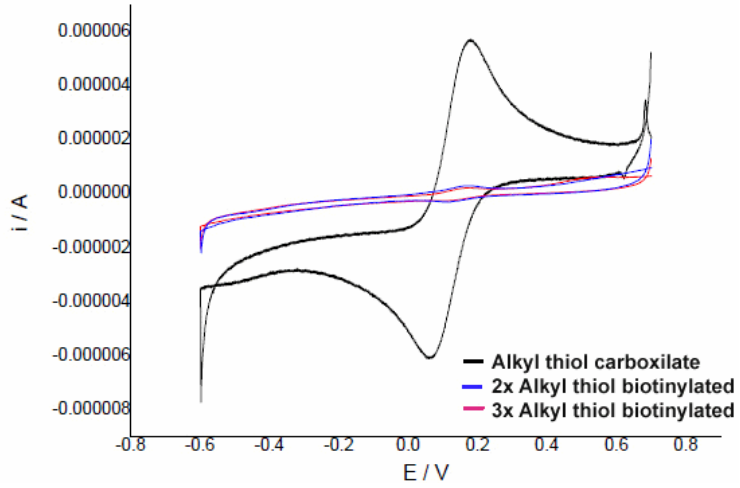

Figure 4.50: Electrode CV characterization.

4.5 Conclusions

- Several synthetic routs for the preparation of superparamagnetic and dielectric core-shell nanoparticles have been studied.

- The isopropanolic procedure has provided particles with better characteristics to be used in the molecular recognition device.

- Magnetic studies have proved that the iron oxide nanoparticles that are protected by silica behave as superparamagnets.

- The silanization of nanobeads was carried out by means of carboxyethylsilanetriol. This permit the nanobead to interact with biological molecules through the carboxylic acid.

- The nanobeads were bioconjugated with anti-CEA, anti-Goat-HRP, Pab-Goat and IgG.

- ELISA assays were performed to determine the union between the nanobeads and the proteins. We can conclude that:

  - PFP is an activator better than NHS.

  - As the concentration of antibody with respect to the nanobeads concentration is raised the adhesion increases.

  - The nanobeads biocojugated with EDC and PFP give more intense signals than the non-activated reactions.

  - The presence of a signal in samples without activation indicates the presence of non-specific interactions, mainly electrostatic interactions.

  - Pab-Goat is the most interacting protein, then IgG and the last CEA.

- From impedance measurements:

- The interaction between the functionalized electrodes by means of alkyl thiol carboxylated with Donkey anti-Rabbit it is good enough.

- The interaction between the electrode functionalized by means of alkyl thiol carboxylated with Donkey anti-Rabbit and anti-Goat is good enough.

- The interaction between the electrode functionalized by means of alkyl thiol carboxylated with Donkey anti-Rabbit and the system nanobead-anti-Goat is not observed.

- The interaction between the electrode functionalized by means of alkyl thiol carboxylated with anti-CEA and CEA is not very good.

- The union between primary antibody CEA and the electrode functionalized by means of alkyl thiol biotinilated is better than the primary antibody CEA and the electrode functionalized by means of alkyl thiol carboxylated.

4.6 Bibliography

[1] Q. A. Pankhurst, J. Connolly, S. K. Jones and J. Dobson. Applications of magnetic nanoparticles in biomedicine. *Journal of Physics D*, 36:167–181, 2003.

[2] S. A. Grant, C. Weilbaecher and D. Lichlyter. Development of a protease biosensor utilizing silica nanobeads. *Sensors and Actuators B*, 121:482–489, 2007.

[3] Y. J. Fan, H. J. Sheen, C. J. Hsu, C. P. Liu, S. Lin and K. C. Wu. A quantitative immunosensing technique based on the measurement of nanobeads' Brownian motion. *Biosensors and Bioelectronics*, 25:688–694, 2009.

[4] A. Goodey, J. J. Lavigne, S. M. Savoyet, M. D. Rodriguez, T. Curey, A. Tsao et al. Development of multianalyte sensor arrays composed of chemically derivatized polymeric microspheres localized in micromachined cavities *J. Am. Chem. Soc*., 123:2559–2570, 2001.

[5] Z. Zhang, Y. Liu, Y. P. Yang and Q. Y. Jin. Micromagnetic simulation for nanobeads detection using planar Hall sensors. *IEEE Transactions on Magnetics*, 41:3625–3627, 2005.

[6] N. T. Thanh, K. W. Kim, C. O. Kim, K. H. Shin and C. G. Kim. Microbeads detection using Planar Hall effect in spin-valve structure. *Journal of Magnetism and Magnetic Materials*, 316:238–241, 2007.

[7] S. Ghionea, P. Dhagat and A. Jander. Ferromagnetic resonance for magnetic microbead sensors. *IEEE Sensors Journal*, 8:896–902, 2008.

[8] J. D. Qui, H. P. Peng, R. P. Liang, X. H. Xia. Facile preparation of magnetic core–shell Fe_3O_4@Au nanoparticle/myoglobin biofilm for direct electrochemistry. *Biosensors and Bioelectronics*, 25:1447–1453, 2010.

[9] S. Patris, C. De Vriese, F. Prohoroff, E. Burgoa, J. Arcos and J. M. Kauffmann. Anti-Clostridium tetani antibody determination in serum samples by amperometric immunosensing. *Electroanalysis*, 22:41–48, 2010.

[10] L. H. Mak, M. Knoll, N. Dankbar, C. Sundermeier and A. Gorschulter. Electro-magnetic biosensor for binding force measurements on ligand–receptor complexes. *Sensors and Actuators B*, 114:132–140, 2006.

[11] J. H. Jang and H. B. Lim. Characterization and analytical application of surfacemodified magnetic nanoparticles. *Microchemical Journal*, 94:148–158, 2010.

[12] M. Souiri, I. Gammoudi, H. Ben Ouada, H, L. Mora, T. Jouenne, N. Jaffrezic-Renault, C. Dejous, A. Othmane and A. C. Duncan. Escherichia coli-functionalized magnetic nanobeads as an ultrasensitive biosensor for heavy metals. *Proceedings of the Eurosensors XXIII Conference*, 1:1027–1030, 2009.

[13] F. Wang, W. B. Tan, Y. Zhang, X. Fan and M. Wang. Luminescent nanomaterials for biological labelling. *Nanotechnology*, 17:R1–R13, 2006.

[14] W. Stöber, A. Fink and E. Bohn. Controlled growth of monodisperse silica spheres in micron size range. *Journal of Colloid and Interface Science*, 26:62–69, 1968.

[15] Y. H. Deng, C. C. Wang, J. H. Hu, W. L. Yang and S. K. Fu. Investigation of formation of silica-coated magnetite nanoparticles via sol-gel approach. *Coll. & Surf. A*, 262:87–93, 2005.

[16] V. Salgueirino-Maceira, M. A. Correa-Duarte, M. Farle, A. Lopez-Quintela, K. Sieradzki and R. Diaz. Bifunctional gold-coated magnetic silica spheres. *Chemistry of Materials*, 18:2701–2706, 2006.

[17] A. Pandey, A. Prasad, J. Moscatello and Y. K. Yap. Glucose Biosensors Based on Vertically-Aligned Multi-walled Carbon Nanotubes. Mater. *Res. Soc. Symp. Proc*., 1204:K13–05, 2010.

[18] P. T. Kissinger. Biosensors – A perspective. *Biosensors and Electronics*, 20:2512–2516, 2005.

[19] M. D. Porter, T. B. Bright, D. L. Allara and C. E. D. Chidsey. Spontaneously organized molecular assemblies. Structural characterization of n-alkyl thiol monolayers on gold by optical ellipsometry, infrared spectroscopy, and electrochemistry. *J. Am. Chem. Soc*., 109:3559-3568, 1987.

[20] E. Souteyrand, J. R. Martin and C. Martelet. Direct-detection of biomolecules by electrochemical impedance measurements. *Sensors and actuators B – Chemical*, 20:63–69, 1994.

[21] J. H. O. Owino, A. Ignaszak, A. Al-Ahmed, P. G. L. Baker, H. Alemu, J. C. Ngila and E. I. Iwuoha. Modelling of the impedimetric responses of an aflatoxin B-1 immunosensor prepared on an electrosynthetic polyaniline platform. *Analytical and Bioanalytical Chemistry*, 388:1069–1074, 2007.

[22] O. Ouerghi, A. Touhami, N. Jaffrezic-Renault,C. Martelet, H. Ben Ouada and S. Cosnier. Impedimetric immunosensor using avidin-biotin for antibody immobilization. *Bioelectrochemistry,* 56:131–133, 2002.

[23] L. Yang, W. Z. Wei, X- H. Gao, J. Xia and H. Tao. A new antibody immobilization strategy based on electrodeposition of nanometer-sized hydroxyapatite for label-free capacitive immunosensor. *Talanta*, 68:40–46, 2005.

[24] H. Ben Fredj, S. Helali, C. Esseghaier, L. Vonna, L. Vidal and A. Abdelghani. Labeled magnetic nanoparticles assembly on polypyrrole film for biosensor applications. *Talanta,* 75:740–747, 2008.

Chapter 5

MNPs encapsulated in a polymer for drug delivery

5.1 Introduction

The idea of using magnetic nanoparticles for drug delivery, where therapeutic agents are encapsulated or attached to magnetic nanoparticles, was proposed by Widder and Senyei in 1978 [1,2]. These particles may have magnetic cores protected with a stabilizing material like polymers or other kind of coatings that can be functionalized. They may also consist of porous polymers that contain magnetic nanoparticles precipitated within the pores [3-5]. Advantages of the use of these complex materials are conjugation with biological ligands and also the possibility to increase the circulation time of magnetic nanoparticles in the blood stream [6]. Moreover, it is of high interest to find a system that permits controlled drug release. In our case the approach that can allow this, is to control the swelling of the system with an external factor, like temperature, ionic strength, or pH. The heating capacity of MNPs can be used for this propose, because it can increase the polymer internal mobility inducing drug release as shown in Figure 5.1. We demonstrate in chapter 2 that the sample A0 can generate heat when an alternating field is applied.

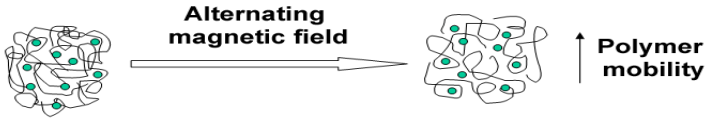

Figure 5.1 An alternating magnetic field induce magnetic nanoparticles to generate heat that can improve the polymer chains mobility facilitating drug delivery.

As a polymeric coating to render magnetic nanoparticles stable in aqueous medium and protect them from aggregation, we have considered poly(4-vinyl pyridine) because the behaviour of solid composites of maghemite nanoparticles in this polymer have been extensively studied in the group [7–10]. In addition, a number of studies have been conducted, mainly from Dupin and co-workers, where they have been demonstrated that microgels made of crosslinked poly(2-vinyl pyridine) (P2VP) showed pH sensitivity and volumetric swelling ratios up to 3 orders of magnitude with mean diameters ranging from 280 to 1010 nm [11–14]. They synthesized the polymer P4VP hydrogel spheres by using monomer polymerization or crosslinking but to the best of our knowledge no work has been introduced up to date in which the fabrication consists on nanoprecipitation. We also want to mention the work of Ren et al. [15], they have shown that copolymers of P4VP-g-PEO of different lengths react very sensitively to temperature, pH and ionic strength. As a result, a magnetic multi-responsive system can be build consisting in a number of components that are: magnetic nanoparticles, a protective coating and a biomolecule that implies the therapeutic effect

Not much work has been carried out concerning to the encapsulation of magnetic nanoparticles for remote heating and controlled local temperature increase in combination with drug encapsulation in order to induce a controlled local release. Here we propose a functional system that is able to combine its thermic effect and pH and ionic strength response in order to facilitate drug delivery. Our system is composed of magnetic iron oxide nanoparticles core and a P4VP coating polymer. The coating polymer enables the system to have an active response to changes in the system environment, like modifications in the pH or ionic strength of the medium, as depicted in Figure 5.2. This change in the polymer structure permits to deliver any drug in a controlled manner.

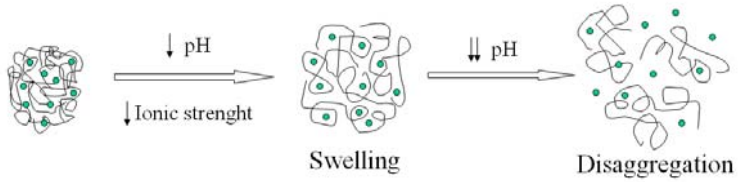

Figure 5.2: As the pH or the ionic strength decreases, the polymer sphere swells

Since our aim is to develop a multifunctional system for drug delivery, we need the magnetic and monodisperse iron oxide nanoparticles, a pH responsive polymer and an active drug. In the following we will introduce the design of such system, its synthesis and characterization.

5.2 Experimental

5.2.1 Materials

1, 2 Dichlorobencene (DCB) (99%) was supplied by Panreac. Oleic acid (pure) was purchased from Fluka and iron pentacarbonyl (pure), surfactant polyvinyl alcohol (PVA) (87–89%, hydrolyzed and average M_w 13000–23000), trimethylamine N-oxide dehydrate, Copper dichloride $CuCl_2$ (99.999%), methyl 2- chloropropionate (MCP) (97%) acetic acid, morpholino ethanesulfonic acid monohydrate (MES) were all products of Sigma Aldrich. Ethanol absolute (reagent grade), dichloromethane (DCM) (extra-pure) and methanol (min 99.8%) were purchased from Scharlau. These solvents and reactants were used as received without further purification. 4-vinyl pyridine (4VP) (Aldrich, 95%) was distilled under vacuum and stored at -5℃. Copper chloride (CuCl) was purified by stirring with acetic acid for several hours, then filtered, washed with acetic acid, ethanol and diethyl ether, successively, and stored under vacuum. Tris [(2-pyridyl) methyl] amine (TPMA) was prepared following literature procedures [16].

5.2.2 Synthesis of poly(4-vinyl pyridine)

We use Atomic Transfer Radical Polymerization (ATRP), discovered by Matyjaszewski´s group in 1995 [17], as polymer synthesis route to obtain polymers with narrow molecular weight dispersion with established average chain lengths. The uniform polymer chain growth was carried out using a transition metal based catalyst. This catalyst provides a balance between active polymer and an inactive form of the polymer, known as the dormant form. Since the dormant state of the polymer is preferred in this equilibrium, side reactions are suppressed. This equilibrium lowers the concentration of propagating radicals, suppressing unintentional termination and permitting the control of molecular weight. ATRP reactions are very robust and they tolerate many functional groups like allyl, amino, epoxy, hydroxy and vinyl groups present in either the monomer or the initiator as shown in Figure 5.3. These methods present other advantages, such as easy preparation, and commercial availability and low cost reactants.

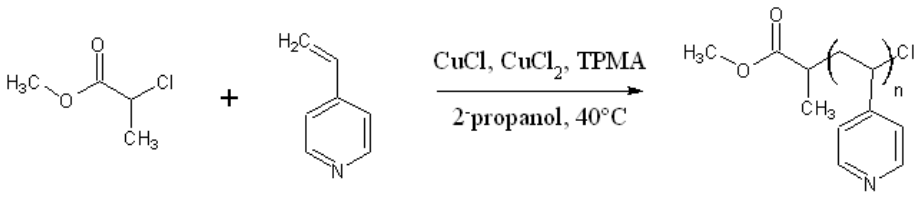

Figure 5.3 Synthesis of P4VP by ATRP.

The propagation rate of the reaction is unique for each individual monomer. Monomers that are typically used in ATRP are molecules with substituents that can stabilize the propagating radicals. Therefore, it is important that the other components of the polymerization (initiator, catalysts, ligands and solvents) are optimized in order to get a higher concentration of the dormant species to be greater than that of propagating radicals so the reaction does not slows down or stops.

Monomer 4VP and polymer P4VP can form complexes with a copper centre without effective catalyst activity in ATRP [18]. In addition, due to the nucleophilic character of the pyridine ring, monomer and polymer can react with the active

polymer chain end "killing" the living nature of the polymerization and leading to branching [19]. To overcome the polymerization of this monomer authors make use of multidentate stronger binding ligands (TPMA, Me6-tren or Me6-[14]ane-N4) with a high complexation constant with the copper centre. Furthermore polymerization is carried out in protic solvents as 2-propanol to reduce polymer contamination by the catalyst. In a similar way authors describe the advantages of chlorine based initiating and catalytic systems over bromine ones. Chlorine based compounds minimizes side reactions as nucleophilic substitution or elimination reactions. Moreover, the initial addition of a certain percentage of a deactivator like a $CuCl_2$ complex resulted in an excellent control over the polymerization [19,20].

In a typical synthesis a 50 ml Schlenk flask with a magnetic stir bar was charged with 51.41 mg of CuCl, 29.90 mg of $CuCl_2$ and 215.20 mg of TPMA. The flask was degassed by three vacuum-argon cycles, and 6 ml of 2-propanol previously deoxygenated by passing argon during 30 minutes were introduced using a syringe. After stirring, 6 ml of deoxigenated monomer 4VP was added under argon atmosphere. Immediately, the mixture was frozen in liquid nitrogen and degassed by 3 freeze-pump cycles. The flask was immersed in an oil bath thermostated at 40^oC. After 10 minutes 0.0825 ml of deoxygenated methyl 2-chloroproprionate were introduced into the flask using a syringe purged with argon. After 7 h of reaction, the flask was open to the atmosphere and the mixture was cooled to room temperature. The homogeneous dark green solution was then diluted with a small amount of 2-propanol and poured into a large amount of cold diethyl ether. The green precipitated polymer was dissolved in dichloromethane, 2 g of Dowex R°50WX2-100 ion-exchange resin were added and the mixture was stirred for 90 minutes at room temperature. After stirring, the mixture was filtered to remove the resin beads. The obtained polymer solution was washed with water until a colourless aqueous phase was observed, and then dried over anhydrous magnesium sulphate and concentrated under vacuum. The polymer was dissolved in a small amount of dichloromethane and poured into a large volume of cold diethyl ether. Finally, the purified polymer, precipitated as a white

powder and was collected by filtration and dried under vacuum at 50ºC for three days. Yield: 2.32 g (39%).

5.2.3 Preparation of blank P4VP nanospheres

The P4VP nanospheres were prepared by a modified nanoprecipitation technique. This method involves the precipitation of the polymer from an organic solution in which is obtained by the diffusion of the organic solvent in the aqueous medium in the presence of a surfactant.

First, 50 mg of P4VP were dissolved in a solution of 1 ml of DCM with 1 ml of methanol. This organic solution was then poured under magnetic stirring into a polar phase consisting of 16 ml ethanol:water in proportion (1:3) and PVA for 20 min at 800 rpm. PVA was used as stabilizing and emulsifying agent. Different concentrations of surfactant PVA (0%, 0.1%, 0.4% and 1%) were used in order to study its influence on the spheres properties.

With the aim of finding out the influence of ionic strength on the swelling of the particles, we dispersed a P4VP suspension of nanospheres synthesized with 1% of PVA (pH 6.8) in 10 mM and 100 mM NaCl respectively and measure their size as a function of time.

5.2.4 Preparation of oleic acid coated magnetic nanoparticles

The synthesis of highly crystalline and monodisperse maghemite nanoparticles was carried out in organic medium by the Hyeon method [21] and it is described in chapter 2.

5.2.5 Encapsulation of oleic acid coated magnetic nanoparticles into P4VP spheres

Magnetic iron oxide nanoparticles have been encapsulated in P4VP spheres by a simple nanoprecipitation process. The encapsulation method involved the formation of an oil-in-water emulsion consisting of an organic phase including the polymer and the

magnetic nanoparticles and an aqueous phase containing the surfactant. A typical encapsulation is described as follows. The aqueous phase was prepared dissolving 15 mg de PVA in 12 ml of hot Milli-Q water. When the solution was cooled, 4 ml of ethanol were added and the mix was poured into a beaker. The organic phase was prepared dispersing one drop of magnetic ferrofluid in 1 ml of DCM, then 1 ml of methanol was added and 50 mg of PVP was dissolved. The organic phase was then added into the aqueous one under magnetic stirring at 800 rpm for 20 min.

In order to study the influence of EtOH:H_2O proportion in the formation of spheres, three different samples were prepared varying the proportion (1:1, 1:3 and 3:1). Some experiments were also carried out varying PVA concentration (0 mg, 15 mg, 30 mg, 45 mg and 100 mg) and modifying P4VP concentration (25 mg, 50 mg, 75 mg and 100 mg) without PVA and finally the behaviour of the system was studied by changing the magnetic charge (1 drop, 2 drops of ferrofluid).

5.2.6 Buffer synthesis

Buffer was adjusted using acetic acid or MES from pH 4 to 7 using appropriate amounts of NaOH or HCl to a concentration of 10 or 100 mM.

5.3 Results and discussion

5.3.1 Poly(4-vinyl pyridine)

In order to characterize the synthesized P4VP, the polymerization degree (DP: 45) and number-average molecular weight (M_n: 4854 Da) of the polymer were determined by ^{1}H-NMR ($CDCl_3$). The 1H NMR spectrum (see Figure 5.4) was fully consistent with the chemical structure and confirmed the purity of the final compound.

Molecular weight distribution (M_w/M_n) of the polymer was evaluated by gel permeation chromatography (GPC) performed on a Waters 2695 autosampler equipped with a Waters 2420 ELSD detector on two in line Phenogel 5 μm Linear/

mixed (2) (7.8x300 mm) columns with a mixture of tetrahydrofuran /(methanol/ ethanol amine (99/1)) (70/30) as eluent at a flow rate of 1ml/min at 35ºC.

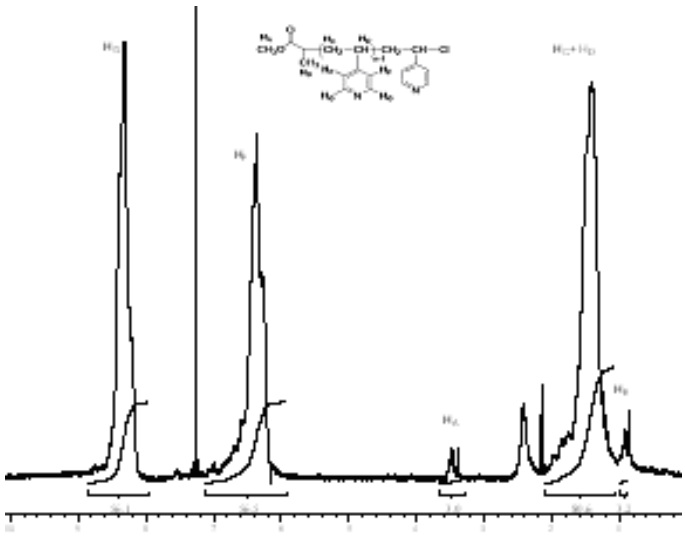

Figure 5.4 ^{1}H NMR spectrum of P4VP prepared by ATRP of 4VP at 40ºC with molar ratio 4VP/MCP/CuCl/CuCl2/TPMA 75/1/0.7/0.3/1.

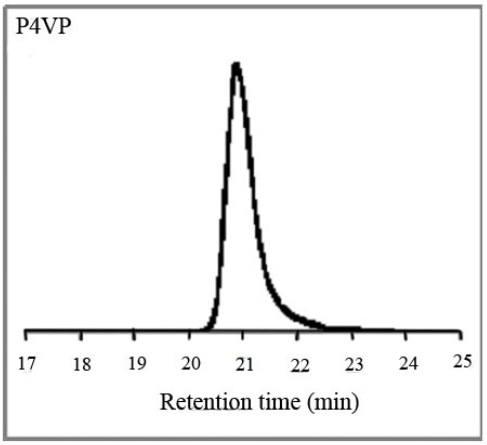

Figure 5.5 GPC trace of P4VP (light scattering detection) synthesized by ATRP.

The GPC measurements (see Figure 5.5) showed a narrow molecular weight distribution for the polymer with a polydispersity index of 1.17. Molecular weight of the polymer was calculated from NMR signals, using the following equations:

$$M_{n,NMR} = M_{4VP}DP + M_{In}$$

$$DP = \frac{3I_{aryl}}{4I_{met}}$$

Where M_{In} corresponds to the molecular weight of the initiator (M_{In} = 122.55), M_{4VP} is the molecular weight of the monomer (M_{4VP} = 105.14) and DP represents to the degree of polymerisation of the polymer. I_{aryl} denotes the integration of peaks of aryl hydrogens (HF+HG, see inset in figure 1) from 6.19 to 8.58 ppm and I_{met} that of the hydrogens of the methoxy group in the polymer chain end (H*A*) from 3.35–3.58 ppm. From the NMR spectrum the calculated DP was 45 and $M_{n;\,NMR}$ = 4854 Da.

5.3.2 Blank P4VP nanospheres

Figure 5.6a shows a SEM micrograph of the polymer spheres with a content of 1% in PVA. It can be observed that the particles have a spherical regular shape with sizes ranging from 200 to 300 nm and no aggregation can be observed. The size of the as-prepared P4VP spheres was also estimated by dynamic light scattering (Figure 1.6b) with an average mean-size of 230 nm. The spheres size is ranging between 150 nm to 450 nm and it can be considered that this is in concordance with SEM data, although SEM diameter is a little bit smaller than the diameter observed by means of DLS.

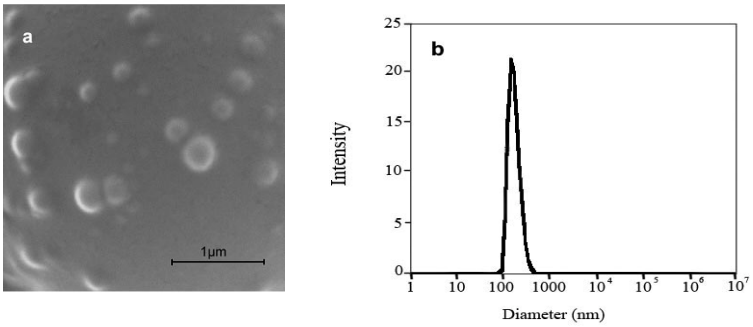

Figure 5.6 a) SEM micrograph of 1% PVA polymer spheres b) DLS of 1% PVA polymer spheres.

The smaller diameter of the spheres measured by SEM with respect to DLS can be explained because dynamic light scattering measures the hydrodynamic diameter, resulting in an increase of the measured diameter.

5.3.2.1 Effect of surfactant concentration

The mean particle size of the nanospheres as a function of PVA concentration in the external aqueous phase was analyzed (Figure 5.7). In this study the mean sphere size was determined by means of DLS. Different concentration of surfactant PVA (0 %, 0.1 %, 0.4 %, 1 %) (w/v) were used in order to analyze the dependence of the nanospheres properties. A number of previous reports demonstrated that by increasing the PVA concentration in the external aqueous phase the size of the nanospheres decreases. In our case, the mean nanosphere size decreased from 440 to 210 nm with an increase in the PVA concentration in the external aqueous phase from 0% to 1% w/v. The bars in the graphic indicate the peak width of DLS measurements this can be considered as the polydispersity estimation. So, as it can be observed the polydispersity was found to increase as the surfactant content decreases, resulting in higher errors. That is in good agreement with previous reports on other polymeric hydrogels like in PLGA micro- and nanospheres [22], showing a decrease of the nanospheres size when increasing the PVA concentration in the external aqueous phase. Such general effect is probably due to the increasing viscosity of the solution upon addition of PVA. The viscosity of the solution increases with increasing PVA concentrations, and this could result in the formation of a stable emulsion with smaller and uniform droplet size, leading to the generation of smaller sized nanospheres with lower polydispersity.

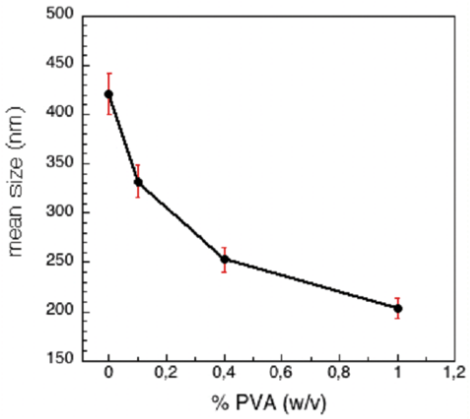

Figure 5.7 Effect of PVA concentration in the spheres size.

5.3.2.2 Stability and swelling kinetics

The major factors that influence the degree of swelling of ionic polymers include the properties of the polymer (charge concentration, pKa of the ionizable group, degree of ionization, crosslinking density and hydrophobicity), and properties of the swelling medium (pH, temperature, ionic strength, counterions in solution and their valence).

With respect to the equilibration time, it has to be stressed that the kinetics of the volume change of gels is not fully understood. For a long time it was assumed that the swelling of a gel was determined by the diffusion of water molecules into a polymer network and that the swelling was fast for very porous networks, facilitating the diffusion of water molecules into it, and slow for dense networks. Now it is generally believed that the swelling process is determined by the diffusion of the polymer network, which has been shown both experimentally and theoretically [23].

In addition to other major factors that influence the swelling of hydrogels, the nature of the buffering species has also been reported to affect the polymer swelling kinetics. For example, swelling in solutions buffered by weak organic acids like acetic acid and MES (used in our experiments) was found to reach equilibrium within a few hours, whereas in unbuffered media it took weeks or months [24].

The fabricated spheres at pH 6.8 were observed to be very stable in water at room temperature during several months and their size remained unchanged over this time (Table 5.1).

Table 5.1: P4VP spheres diameter and polydispersity index values measured as a function of time

Time (months)	Diameter (nm)	PdI
0	230	0.139
2	240	0.194
4	240	0.121

5.3.3 Oleic acid coated magnetic nanoparticles

The iron oxide MNPs are characterized in chapter 2.

5.3.4 Magnetic P4VP spheres

To obtain a multi-responsive system, iron oxide magnetic nanoparticles with a mean size of 6 nm were encapsulated in P4VP polymer spheres by the nanoprecipitation method as described in the experimental section. Figure 5.8a shows a TEM micrograph of the sample as prepared without further purification, the spheres range in size between 1 and 3 μm. It can be observed from the images that the concentration of nanoparticles inside the spheres is higher than outside in the samples without purification, so the particle internalization is considered good. The inset of Figure 5.8 presents the electron diffraction (ED) pattern of a selected area inside a sphere. All the rings in the pattern are clearly defined, which reveals is the presence of a nanocrystalline material inside the sphere.

Some studies were performed in order to analyze the influence of some parameters in the particle formation. We can conclude that the proportion of

EtOH:H_2O in the aqueous phase does not affect the particle size. In the absence of PVA the particle diameter increased, however, in the presence of PVA in amounts varying from 15 mg to 100 mg no significant changes were observed. The same occurred when we fixed the PVA concentration and changed the amount of P4VP from 25 mg to 100 mg.

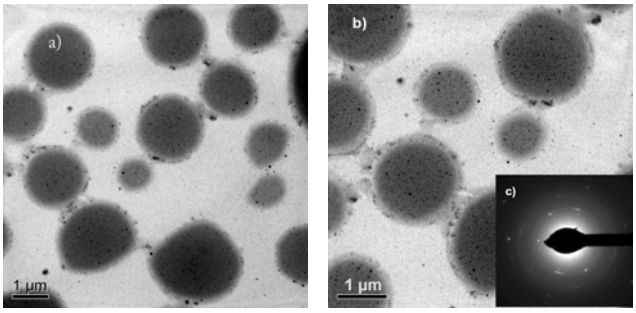

Figure 5.8 a) TEM micrograph of iron oxide nanoparticles inside of polymer spheres b) TEM and ED.

However, if we change the magnetic nanoparticle loading, a variation in particle size can be observed. If we compare two samples prepared in the same way, and using the same amount of reactants, but with one and two drops of iron oxide DCB solution respectively, the size changes as it can be seen in Figure 5.9. The sample with only one drop, with an average diameter of 710 nm, is higher in size than the two drops sample, with an average diameter of 240 nm. TEM micrographs of both samples are shown in Figure 5.10. It is thus clear that both the polydispersity and the average size of the obtained polymer spheres decreases with the magnetic loading. That can be explained because of the DCB solvent of the iron oxide nanoparticle suspension interacts with the organic phase composed of DCM.

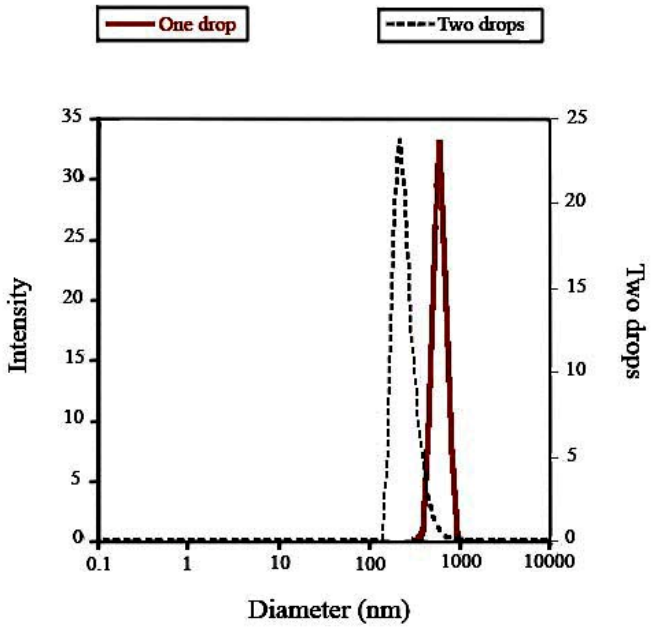

Figure 5.9 DLS of samples loaded with one and two drops of ferrofluid respectively.

In order to study the effect of P4VP concentration in the particle size in the absence of surfactant, four experiments were performed. The experimental data and the mean diameter estimated by DLS are presented in Table 5.2. It can be seen that the diameter increased with the P4VP content.

Table 5.2: DLS values for different concentration

Sample	[P4VP] (mg)	DLS mean size (nm)
C1	25	1200
C2	50	1800
C3	75	2800
C4	100	3000

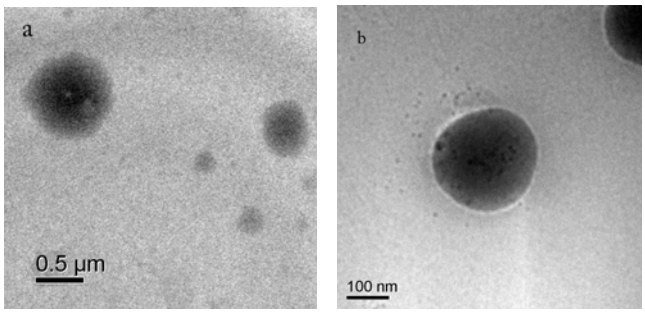

Figure 5.10 a) TEM micrograph of one drop loaded spheres b) TEM micrograph of two drops loaded spheres.

5.3.4.1 Magnetic P4VP-PEG spheres

It is well known that PEG is a biocompatible polymer which is capable of increasing the blood circulation time of nanoparticles in biosystem. Therefore, a P4VP-PEG block-co-polymer was employed instead of P4VP to encapsulate iron oxide nanoparticles using the nanoprecipitation technique. Two different procedures were followed, one of them in the presence of PVA (15 mg) and the other in the absence of any surfactant. DLS measurements indicated that the average diameters were 460 nm for spheres prepared with PVA, whereas that and 575 nm for those prepared in the absence of surfactant. That increment of size in the absence of surfactant was confirmed by TEM measurements, as shown in Figure 5.11, and is coincident with the behaviour of P4VP polymer previously presented.

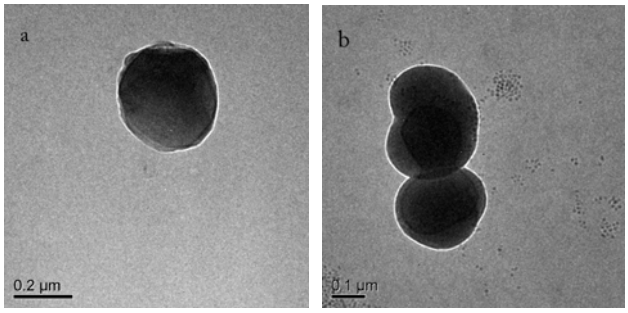

Figure 5.11: a) TEM micrograph of P4VP-PEG spheres with PVA, b) TEM micrograph of P4VP-PEG spheres without PVA.

5.4 Conclusions

Summarizing, we describe a simple synthesis method to obtain a multifunctional and multi-responsive system for a number of biomedical applications. This system renders the core magnetic to enable external controlled actuation under a magnetic field, and the polymeric coating consists on a pH responsive polymer. Furthermore, the system is shown to be ionic strength responsive.

In a first stage we have developed a new and straightforward chemical synthesis to prepare stimuli-responsive non crosslinked P4VP nanospheres. The P4VP polymer was synthesized by atom transfer radical polymerization in order to have a good control of the average molecular weight and the polydispersity. A nanoprecipitation process was used to obtain P4VP nanospheres due to its advantages, as it is simple, rapid and reproducible. The obtained nanoparticle suspensions in water were stable during several months. It is found that the surfactant concentration in the synthesis step plays a very important role in the size control of the nanospheres. In particular, as the concentration increases the volume decreases resulting in mean diameters varying from 200 to 420 nm.

In order to give these systems magnetic heating functionality we encapsulated oleic acid coated iron oxide nanoparticles with defined size and crystallinity. As described in chapter 2, these nanoparticles are superparamagnetic and capable of undergo a magnetically driven heating, and their relative heating performance decreases with the concentration due to interparticle interactions.

We have also described a chemical synthesis procedure to prepare multi-responsive P4VP microspheres loaded with iron oxide nanoparticles, based on the nanoprecipitation method. We achieved a hybrid (organic-inorganic) material by encapsulating oleic acid-coated iron oxide nanoparticles with sizes of the order of 6 nm in a P4VP spheres with sizes between 1 and 3 μm. Subsequently we use P4VP-PEG block-co-polymer to encapsulate the iron oxide nanoparticles in order to provide

the system with a protective biocompatible layer and increase the blood circulation time, with an average size of 460 nm.

It is interesting to combine the possibilities that offer this kind of systems in order to take the maximum advantage of them fusing the therapeutic effect with diagnosis. The system has the potential capacity of deliver a therapeutic agent in a controlled manner. The magnetic nanoparticles can induce remote effects since it is possible to use their properties to absorb energy and convert it into heat, it also can be consider that they can be directed by a magnetic field to a target point and deliver a specific drug. Another interesting possibility is to use their diagnosis properties as a contrast agent in MRI. However, there is still a lot of work to do to develop this system before arriving to clinical practice.

5.5 Bibliography

[1] K. Widder, A. E. Senyei and D. G. Scarpelli. Magnetic microspheres: A model system for site specific drug delivery invivo. *Proccedings of the Society for Experimental Biology and Medicine*, 158:141–146, 1978.

[2] A. Senyei, K. Widder and G. Czerlinski. Magnetic guidance of drug-carrying microspheres. *J. Appl. Phys*., 49:3578–3583, 1978.

[3] J. Kim, J. E. Lee, S. H. Lee, J. H. Yu, J. H. Lee, T. G. Park and T. Hyeon. Designed fabrication of a multifunctional polymer nanomedical platform for simultaneous cancer-targeted imaging and magnetically guided drug delivery. *Advanced Materials,* 20:478–483, 2008.

[4] Y. H. Deng, C. C. Wang, J. H. Hu, W. L. Yang and S. K. Fu. Investigation of formation of silica-coated magnetite nanoparticles via sol-gel approach. *Colloids and Surfaces A*, 262:87–93, 2005.

[5] D. X. Li, Q. He, Y. Yang, H. Mohwald and J. Li. Two-stage pH response of poly(4-vinylpyridine) grafted gold nanoparticles. *Macromolecules,* 41:7254–7256, 2008.

[6] R. I. Mahato. Water insoluble and soluble lipids for gene delivery. *Advanced Drug Delivery Reviews,* 57:699–712, 2005.

[7] A. Millan, A. Urtizberea, N. Silva, F. Palacio, V. Amaral, E. Snoeck and V. Serin. Surface effects in maghemite nanoparticles. *Journal of Magnetism and Magnetic Materials*, 312:5–9, 2007.

[8] A. Millan, F. Palacio, A. Falqui, E. Snoeck, V. Serin, A. Bhattacharjee, V. Ksenofontov, P. Gutlich and I. Gilbert. Maghemite polymer nanocomposites with modulated magnetic properties. *Acta Materialia,* 55:2201–2209, 2007.

[9] A. Millan, A. Urtizberea, N. J. de Oliveira, P. Boesecke, E. Natividad, F. Palacio, E. Snoeck, L. Soriano, A. Gutierrez and C. Quiros. Multiplelength- scale small-angle X-ray scattering analysis on maghemite nanocomposites. *Journal of Applied Crystallography,* 40:696–700, 2007.

[10] Y. Komorida, M. Mito, H. Deguchi, S. Takagi and A. Millan and F. Palacio. Pressure effects on γ-Fe_2O_3 nanoparticles. *Journal of Magnetism and Magnetic Materials*, 310:800–8002, 2007.

[11] D. Dupin, S. Fujii, P. Reeve, S. M. Baxter and S. P. Armes. Eficient synthesis of sterically stabilized pH-responsive microgels of controllable particle diameter by emulsion polymerization. *Langmuir,* 22:3381–3387, 2006.

[12] D. Dupin, S. P. Armes, C. Connan, P. Reeve and S. M. Baxter. How does the nature of the steric stabilizer affect the pickering emulsifier performance of lightly cross-linked, acid-swellable poly(2-vinylpyridine) latexes*? Langmuir*, 23:5903–6910, 2007.

[13] D. Dupin, J. Rosselgong and S. P. Armes. Swelling kinetics for a pH-induced latex-to-microgel transition. *Langmuir*, 23:4035–4041, 2007.

[14] J. Yin, D. Dupin, J. Li, S. P. Armes and S. Liu. pH-induced deswelling kinetics of sterically stabilized poly(2-vinylpyridine) microgels probed by stopped- flow light scattering, *Langmuir,* 24:9334–9340, 2008.

[15] Y. Ren, X. Jiang and J. Yin. Copolymer of poly(4-vinylpyridine)- poly(ethylene oxide) respond sharply to temperature, pH and ionic strength, *European Polymer Journal*, 44:4108–4114, 2008.

[16] Z. Tyeklar, R. R. Jacobson, N. Wei, N. N. Murthy, J. Zubieta and K. D. Karlin. Reversible-reaction of O_2 (and CO) with a copper(I) complex. X-ray structures of relevant mononuclear Cu(I) precursor adducts and the trans- (μ-1,2-peroxo)dicopper(ii) product. *Journal of the American Chemical Society,* 115:2677–2689, 1993.

[17] J. Wang and K. Matyjaszewski. Atom Transfer Radical Polymerization. Chem. Rev., 101:2921–2990, 2001.

[18] J. H. Xia, X. Zhang, K. Matyjaszewski, Atom transfer radical polymerization of 4-vinylpyridine, *Macromolecules,* 32:3531–3533, 1999.

[19] N. V. Tsarevsky, W. A. Braunecker, S. J. Brooks and K. Matyjaszewski. Rational selection of initiating/catalytic systems for the copper-mediated atom transfer radical polymerization of basic monomers in protic media: ATRP of 4-vinylpyridine. *Macromolecules,* 39:6817–6824, 2006.

[20] F. J. Jiang, A. Kaltbeitzel, W. H. Meyer, H. T. Pu and G. Wegnert. Proton-conductin a polymers via atom transfer radical polymerization of diisopropyl-p-vinylbenzyl phosphonate and 4-vinylpyridine. *Macromolecules,* 41:3081–3085, 2008.

[21] T. Hyeon. Chemical synthesis of magnetic nanoparticles. *Chemical Communications*, 8:927–934, 2002.

[22] H. Zhao, J. Gagnon and U. O. Hafeli, Process and formulation variables in the preparation of injectable and biodegradable magnetic microspheres, *Biomagn. Res. Technol.,* 5:2–5, 2007.

[23] B. A. Firestone and R. A. Siegel. Kinetics and mechanisms of water sorption in hydrophobic, ionizable copolymer gels. *Journal of Applied Polymer Science,* 43:901–914, 2003.

[24] T. Tanaka and D. J. Fillmore. Kinetics of swelling of gels. *Journal of Chemical Physics,* 70:1214–1218, 1979.

List of abbreviations

μ-CP	Micro contact printing
2VP	2-Vinylpyridine
4VP	4-Vinylpyridine
acac	Acetylacetonate
AEE	Aminoethoxy ethanol
AFM	Atomic force microscopy
ATRP	Atomic transfer radical polymerization
BSA	Bovine serum albumin
CEA	Carcinoembryonic antigen
Cup	N-nitrosophenylhydroxylamine
CV	Cyclic voltametry
DCB	Dichlorobencene
DCM	Dichloromethane
DDA	Dodecilamine
DEA	2-(Diethylamino) ethyl methacrylate
DLS	Dynamic light scattering
DPA	2-8diisopropylamino) ethyl methacrylate
DTESP	Diethyl [2-(triethoxysilyl) ethyl] phosphonate
ED	Electron diffraction
EDC	1-Ethyl-3-(3-dimethylaminopropyl) carbodiimide
EDIPA	Ethyldiisopropylamine

EELS	Electron energy loss spectroscopy
EIS	Electrochemical impedance spectroscopy
ELISA	Enzyme-Linked immuno sorbent assay
FTIR	Fourier transform infrared spectroscopy
GPC	Gel permeation chromatography
IBEC	Instituto de Bioingeniería de Cataluña
IgG	Immunoglobuline G
IO	Iron oxide
IOMNPs	Iron oxide magnetic nanoparticles
IP	In-phase
IR	Infrared
JCPDS	Joint committee on powder diffraction standards
MCP	methyl 2-chloropropionate
MES	Morpholino ethanesulfonic acid monohydrate
MNPs	Magnetic nanoparticles
MPEGPLA	Methoxy poly(ethylene glycol) polylactide copolymer
MRI	Magnetic resonance imaging
NHS	N-hydroxysuccinimide
NMR	Nuclear magnetic resonance
OA	Oleic acid
OE	Dioctyl ether
OP	Out-of-phase
P4VP	Poly 4-vinyl pyridine

PBS	Phosphate buffer solution
PCL	D, L-caprolactone
PD	Polymerization degree
PdI	Polydispersity index
PEG	Poly(ethylene glycol)
PEI	Poly(ethylene imine)
PEO-PPO-PEO	Poly(ethylene oxide)-poly(propylene oxide)-poly(ethylene oxide) block copolymers
PFP	Pentafluorophenol
PLLA	Poly(D, L-lactide-co-glycolide)
PVA	polyvinyl alcohol
RT	Room temperature
SAED	Selected area electron diffraction
SAR	Specific absorption rate
Sil-PEG	N-(3-triethoxysilylpropyl) O-polyethylene oxide urethane
TEM	Transmission electron microscopy
TEOS	Tetraethyl orthosilicate
TESDI	N-(3-triethoxysilylpropyl)-4, 5-dihydroimidazole
TESPDA	3-(Triethoxysilyl) propylureido dodecanoic acid
TGA	Thermogravimetric analysis
TMB	3, 3′, 5, 5′-Tetramethylbenzidine
ToF-SIMS	Time-of-flight secondary ion mass spectrometry
TOPO	Trioctylphosphine

TPMA	Tris [(2-pyridyl)methyl] amine
XRD	X-ray diffraction

Publications

A. Urtizberea, E. Natividad, A. Arizaga, M. Castro and A. Mediano. Specific absorption rates and magnetic properties of ferrofluids with interaction effects at low concentrations. *J. Phys. Chem*. C 114: 4916–4922, 2010.

A. Arizaga, G. Ibarz and R. Piñol. Stimuli-responsive Poly(4-vinyl pyridine) hydrogel nanoparticles: síntesis by nanoprecipitation and swelling behavior. *Journal of Colloid and Interface Science* 348:668-672, 2010.

A. Urtizberea, A. Arizaga, N. J. O. Silva, A. Millán, F. Palacio and F. Luis. Texture-induced magnetic interactions in ferrofluids. *Journal of Applied Physics* 111:093910-093916, 2012.

A. Arizaga, G. Ibarz, R. Piñol and A. Urtizberea. Encapsulation of magnetic nanoparticles in a pH-sensitive poly(4-vinyl pyridine) polymer: a step forward to a multi-responsive system. *Journal of Experimental Nanoscience* 1-9 iFirst, 2012.

A. Arizaga, A. Millán, U. Schubert and F. Palacio. Synthesis of silica-coated aqueous ferrofluids through ligand exchange with a new organosilica precursor. *Journal of Materials Science* 48:2550-2556, 2013.